ISSN 1068-3755, Surface Engineering and Applied Electrochemistry, 2009, Vol. 45, No. 2, pp. 81–84. © Allerton Press, Inc., 2009.
Original Russian Text © V.D. Shkilev, A.N. Adamchuk, 2009, published in Elektronnaya Obrabotka Materialov, 2009, No. 2, pp. 4–8.

ELECTRICAL DIMENSIONAL MATERIALS PROCESSING

On New Approaches in Data Base Formation of Identification Marks Obtained by the Electrodischarge Method

V. D. Shkilev and A. N. Adamchuk

Ministry of Informational Development of the Moldova Republic, ul. Pushkina 42, Chisinau, MD-2012 Moldova Republic
e-mail: schilov@registru.md

Received December 24, 2008

Abstract—Ways of protection of identification marks obtained by the electrodischarge method on the basis of the Cartesian, spectral, and phase picture approaches have been offered. It has been shown that a sufficiently reliable level of protection can be attained at a mark processing time duration on the order of five seconds.

DOI: 10.3103/S106837550902001X

The interference pictures discovered and described in [1] resulting from electrical discharges hitting a paper target (a future document of special significance) required the development of new approaches to data base formation.

In the creation process of the identification mark, there should have been developed a new technology sooner or later that would enable the protection of a numerical code on a material carrier by means of a practically unique matrix (a picture composed of electrical discharge patches). The stochasticity of a gas discharge [2] provides the possibility to create each time a unique matrix, and it is this property of stochasticity that permits the development of novel ways in the area of material resources identification.

The unity of state documents circulation may be attained with the help of universal principles providing the protection of both a material paper carrier and the electronic form of a document while transferring a similar kind of information and with their being protected by an electronic numerical signature.

A significant moment in the investigations was the fact that the initially described experiment [1] was carried out using a specific high frequency (200–300 Hz) high voltage source with sharp edges. The experiment was performed within the limited range of interelectrode gaps (5–10 mm).

There appeared the necessity to see whether or not the intenferential pictures remain on the target with the use of an ordinary high voltage transformer feeding from an industrial power circuit of 50 Hz in the range of interelectrode gaps of 15–20 mm. The pattern of the experiment, the methodology of the experiment, and the mathematical processing of the results were similar to [1]. There was defined the center of the apertures distribution, the target was divided into a preset number of rings around the determined center, and the apertures' relative areas on a ring of preset radius were calculated.

As the targets, paper carriers were used, and some of the charges rapidly found their individual way in the interelectrode gap (Figs. 1 and 2).

Taking a picture of the process with an exposure of several seconds confirms the uniqueness of the spark discharge path.

The obtained set of electrodischarge patches needs to be fixed and introduce into a data base. This should be done in order to provide for the material resources identification in the future [3]. The identification may be performed in two stages: the first stage includes the retrieval of a definite material resource in the data base by means of a numerical code. This stage may be easily automatized with the help of the stroke code. The second stage, i.e., the identification itself, is a comparison of the irreproducible (individual) matrix of an article with an individual matrix kept in the data base. How is such a data base formed? Firstly, it is necessary to create a center of the individual identification marks, which will provide such marks for all the enterprises

Fig. 1. Discharge photos at an exposure of 5–10 seconds.

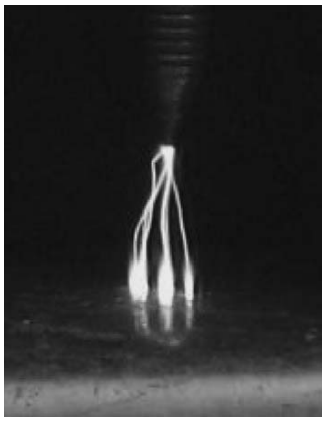

Fig. 2. Discharge photos at an exposure of 5–10 seconds.

marking the objects they produce. Such a center will slightly differ from the certification center of private keys by its methodology, and the very process of the identification is somewhat identical to the checking of the documents authenticity by means of their electronic-numerical signature. The process of identification is considered accomplished at the coincidence of the individual matrix on the article with the one kept in the data base under this number. Later on, after carrying out the system operation analysis on the basis of this principle, the delivery of the identification equipment to each enterprise will be possible. The report of an enterprise to the state will be different from today's not only by marking the article with a numerical code but with the individual matrix to match each numerical code. A system based on the individual matrices only without the numerical codes is inexpedient because of the complexity of the images identification. In the presence of a numerical code on the mark, the search is carried out by the numerical codes. Once it is discovered that, on an article offered for sale, under the numerical code is the wrong individual matrix, the tax inspectorate should raise the alarm. Let us touch upon the creation of such data bases. There are several of them. First, the most simple is the well-known Cartesian approach (Fig. 3), when each of the electrical discharge patches (which vary both in their area and configuration) is reduced to a dot by means of software. It is not much of a difficulty to manage such an approach. However, it is appropriate only for technology based on introduction of a random (individual) set of dots into a material object, and, hence, it may be applied only for hard (electroconductive and dielectric) material resources.

It is of interest that the spectral approach and the method of random electrodischarge patches have common informational roots. However, the depth and degree of generalization of the spectral approach makes it more significant in comparison with the Cartesian one.

It becomes clear that something that was conceived as a dot by us after the Cartesian processing is comprehended as the top of a spectral peak from the viewpoint

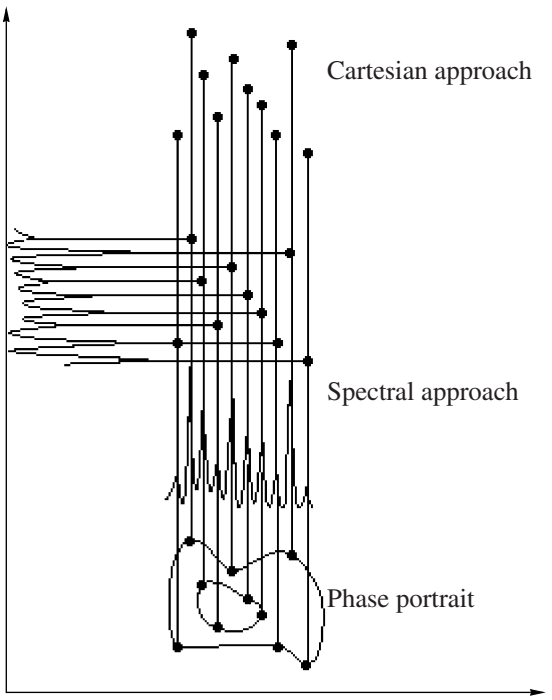

Fig. 3. Cartesian, spectral, and phase approaches in the data-base formation.

of the spectral approach. Such an approach will easily unite the information processing of not only electrodischarge [4] identification but will also allow one to create a common data base using universal principles.

There is one more approach in the data base formation—it is a phase portrait. The term "phase portrait" was introduced by Academicians L.I. Mandelshtam and A.A. Andronov into science in the middle of the past century. It was mainly used in electrodynamics in the study of oscillation and wave processes. However, the efficiency of the "phase approach" application in material resources identification is obvious.

By connecting separate dots on a phase plane, we obtain the phase trajectory. A system of closed phase trajectories forms a phase portrait of a resource. In the informational sense, the spectral and phase approaches are equivalent. The phase approach in a certain way resembles classical dactyloscopy, which is based on the comparison of papillary (phases, as a matter of fact) trajectories. If the Cartesian approach is based on a numerical principle (a set of coordinates of random dots), the spectral and, particularly, the phase ones are based on the image comparison. The Cartesian approach is very easy to automatize, while the spectral and phase approaches rest on the complexity of a mathematical theory of images identification. The theory, as a matter of fact, has been swiftly developing and the hope remains that these approaches will be automatized in the nearest future. Today, the two latter approaches assume only an expert level of identification, which

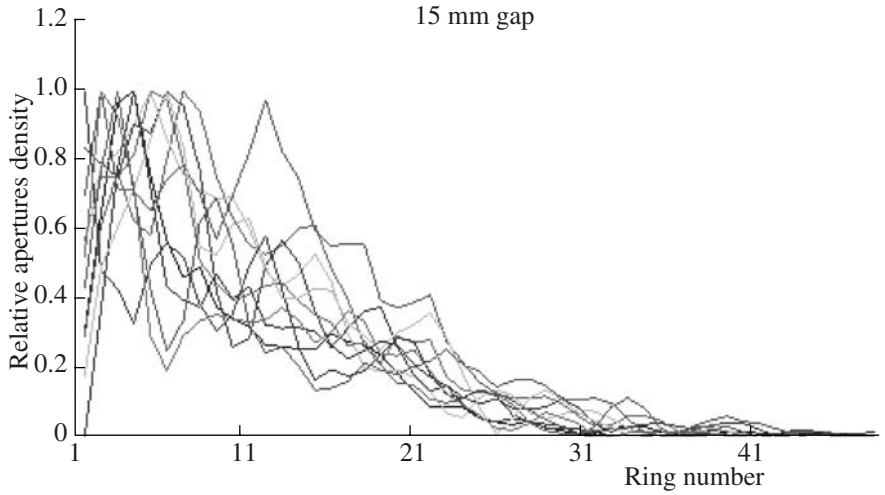

Fig. 4. Interferential pictures at a 15 mm gap.

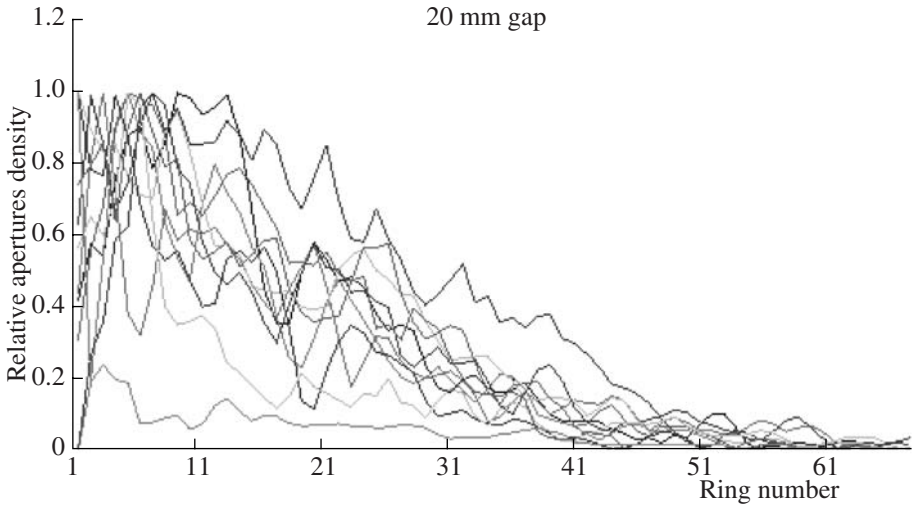

Fig. 5. Interferential pictures at a 20 mm gap.

requires a highly qualified expert to participate in making the decision.

The subject of the elaboration of the data-base formation principle is sufficiently profound and demands writing a series of papers in the course of time.

Let us proceed to a discussion of the recently obtained experimental data with gaps of 15 and 20 mm (Figs. 4 and 5) and a high voltage transformer power source fed by an industrial power circuit.

As was expected, the interference pictures appeared under those conditions as well. The interference waves are formed not by the power source but by a physical phenomenon—the arc discharge (more precisely, by the inseparable unity of a wave streamer and the discharge itself). The interference pictures result from the electric discharge stochasticity effect [4]. Returning to the present experiment, we should note that the explanation of the interference picture by gas discharge stochasticity requires a more profound further examination of the physical process. It is necessary to create new software that reveals all the details of stochasticity manifestation.

The present paper is devoted to the technological aspects and the possibility of the examined technology application for material resources identification and to the principles of the individual matrix data-base creation obtained by the electric discharge process. It will be worthwhile to come back to the physical aspect of the question in the future as new experimental data becomes available.

A factor of no less importance is the target processing durability, on which the economical and technological aspects of the proposed technology depend. The target processing time in all the experimental series [1] was identical and equaled 60 seconds.

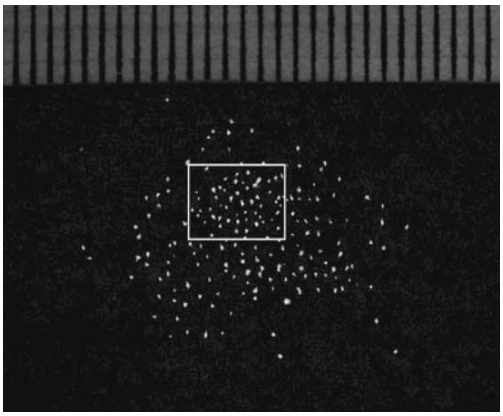

Fig. 6. A typical collection of electrodischarge patches.

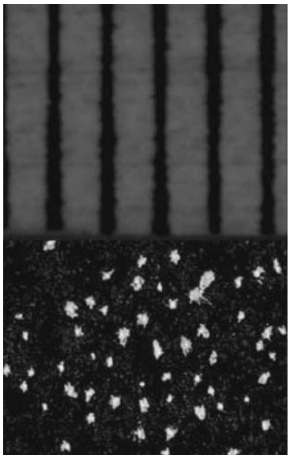

Fig. 7. The patches' identity on a matrix.

In a new series of experiments, the duration of the processing varied from 5 to 6 seconds and up to 2 minutes with a step of 15 seconds.

The comparative analysis confirms that the highest degree of information protection can be attained even for 5–6 seconds. Further processing of the target insignificantly increases the number of patches on the target, which results from the discharge hitting the previously formed patches.

Electrodischarge patches change their exterior outlines and sizes after repeated hitting. No doubt, the individuality (Fig. 6) of each of the obtained electrodischarge patches may considerably enhance the informational uniqueness and reliability of the expert identification.

The singled out light square in Fig. 6 at a large magnification (Fig. 7) displays the individuality of the patches and allows one to distinguish inside each of them a more light site, which is a transparent channel, where the electric discharge gets through. The rest of the patch is formed due to the black dye evaporation.

It is evident that the repetition probability of the individual matrix built on the basis of a set of electrodischarge patches (admitting the similarity of the patch forms and sizes) on the matrix is several orders lower than the one based on the patches individuality registration.

Nevertheless, the probability, even in the first case, is so insignificant that it will produce no effect on the economic relations and, hence, allows for a reduction of each electrodischarge patch to a dot, in accordance with the known programs of figure center detection and the Cartesian approach, thus providing complete automatization of the identification free from experts participation.

A more profound level of identification based on a comparison of the electrodischarge patch forms involves the application of a complex mathematical theory of image distinguishing; therefore, its automatization seems problematic at the first stage.

At present, this identification level is called the expert one, and it is performed by hand, by way of comparison of the electrodischarge patch forms of the identification mark with the identical information in the data base.

REFERENCES

1. Shkilev, V.D., Adamchuk, A.N., and Nedioglo, V., Electrodischarge Technology of Protection the Documents of Special Significance (strict accounting), *Surf. Eng. Appl. Electrochem.*, 2008, no. 2, pp. 4—10.
2. Feynman, *Feynman Lectures on Physics. Electricity in the Atmosphere*, 1964, vol. 5, p. 174.
3. Karanfil, V.G., Fotenko, V.M., and Shkilev, V.D., Republic Moldova Patent 3389, 2007.
4. Podlipchuk, V.Yu., Stochastic Model of Quantum Mechanics, *Teor. Mat. Fiz.,* 1990, vol. 82, no. 2, pp. 208–215.

ISSN 1068-3755, Surface Engineering and Applied Electrochemistry, 2009, Vol. 45, No. 2, pp. 85–92. © Allerton Press, Inc., 2009.
Original Russian Text © S.I. Galanin, A.S. Galanina, I.V. Kalinnikov, 2009, published in Elektronnaya Obrabotka Materialov, 2009, No. 2, pp. 9–18.

ELECTRICAL DIMENSIONAL MATERIALS PROCESSING

Technological Features of Electrochemical Polishing of Gold Alloys by Pulse Currents

S. I. Galanin, A. S. Galanina, and I. V. Kalinnikov

Kostroma State University of Technology, ul. Dzerzhinskogo 17, Kostroma, 156005 Russia
e-mail: ikalinnikov@yandex.ru

Received November 30, 2008

Abstract—The features of the electrochemical polishing of complex shaped jewelry made of different gold alloys by unipolar and bipolar current pulses have been considered. A comparison with the other polishing processes has been carried out.

DOI: 10.3103/S1068375509020021

INTRODUCTION

Under the conditions of much competition, heavy demands are imposed on the quality of jewelry from various gold alloys. The high reflectivity of their surface is one of the performance criteria. The transition to small-batch production and making unique articles with their design becoming more and more complicated is a tendency of modern manufacturing. Fashionable articles are often marked by complex-shaped and textured surfaces, undercutting, fine design, articulated moving elements, and thin projecting details.

The finishing of such complicated "design pretentious novelties" presents some difficulties. The technological finishing processes most extensively employed at present are not possible for such articles (turbotumbling); don't always ensure the required quality of the surface, namely, its luster and a low microroughness over the entire surface (vibrotumbling); or are too costly and demand highly qualified workers (hand polishing). Old technological methods and processes that haven't found wide application for some reasons have become needed. Electrochemical polishing (ECP), which was used for the first time early in the 20th century, is one of them [1].

ECP by direct currents is not widely used in jewelry production for the reason that a high quality of the surface is attained only in expensive and ecologically harmful cyan electrolytes. ECP in noncyan electrolytes is more promising in the context of the more rigid demands for ecological safety. It turns out to be necessary to use both unipolar [2] and bipolar [3] pulse currents instead of a direct current with the aim to improve this process. Industrial application of such a complex technological process inevitably has some peculiarities, which are examined in this very article.

Some Features of the Process of ECP by Pulse Currents

The theory supposes that high quality ECP is attained when the rates of the surface anode dissolution and passivation are commensurable and high enough [4] to provide the quick dissolution of the activated microprojections of the treated surface as compared with the passivated microhollows, resulting in the microrelief smoothing. The investigation shows that the polarization peak magnitudes connected with the anode dissolution are not achieved immediately. The dynamics of their evolution are different in the micro- and millisecond time ranges [5]. Thus, by varying the amplitude and current pulse duration in this time range, it is possible to form an anode potential ensuring a compromise between the rates of dissolution and the passivation processes.

The required state of the anode surface and the "anode–electrolyte" interface is supported by the selection of the duration of the pause between the impulses while taking into account the polarization drop dynamics and the peculiarities of the phenomena at the boundary surface attendant on the drop. For every "anode material–electrolyte of a certain composition" pair, the process development rates are different, the potential optimum magnitudes for ECP differ too, and the pulse current amplitude and time parameters of the current pulses (ATPCP) (the amplitude density, the pulse duration, and the pauses between the pulses) ensuring the highest rate of the surface microrelief smoothing [6] differ respectively.[1]

Two regions (*CD* and *EF*) where there are possible ECP stand out on the generalized anode polarization curve (Fig. 1) characterizing (to a certain extend) the processes occurring at the "anode–electrolyte" interface. They correspond to the surface transition from the

[1] Galanin, S. I., Galanina, A. S., Kalinnikov, I. V., *Elektronnaya Obratotka Materialov*, 2009, no. 2, pp. 9–18.

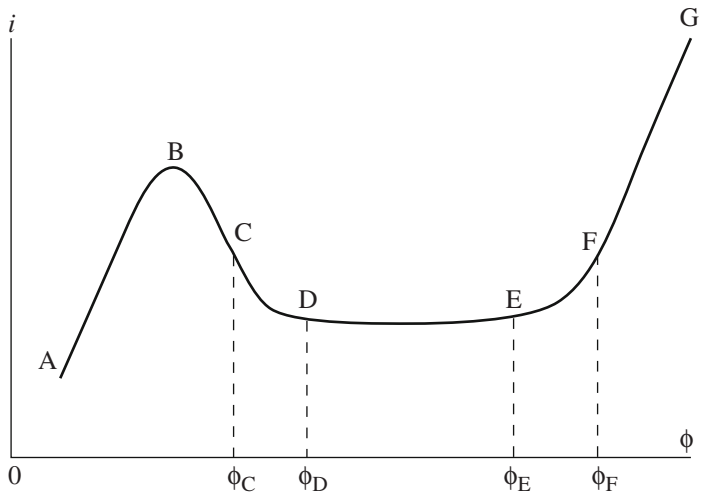

Fig. 1. Generalized anode polarization curve: i is the current density, φ is the anode potential.

active state into the passive one and from the passive state into the transpassive one, respectively. The rates of the surface passivation and dissolution in these portions are much the same. It is possible to maintain the anode potential value in the required region of CD or EF through selection of the electrolyte composition and temperature, the hydrodynamic conditions in the near-electrode area, and the ATPCP. The use of a pulse current as compared with a direct one allows the following:

—to widen the CD and EF regions and ensure more modern technology due to sustaining the surface polishing at broader variation of the process conditions;

—to accomplish polishing in electrolytes with simpler compositions without admixtures, making the process less expensive and more straightforward;

—to carry out ECP with greater efficiency when the rate of smoothing of the microirregularities of the surface under treatment grows substantially; and

—to conduct ECP in relatively cold electrolytes (20–40°C), thus decreasing the ecological burden on the environment and the necessary power expenditures and improving the conditions of the work.

Experimental Procedure

An aqueous solution of thiocarbamide 9% and sulfuric acid 7% was the employed electrolyte. Plates from titanium VT-3 were the cathodes. The treated surface was examined with the help of MII-4 and METAM-32LV microscopes, and the height of its microirregularities R_Z and its reflectivity were measured [6–8]. The specimens were weighed with the help of a chemical balance with an accuracy of ±0.0001 g before and after the treatment. The treatment efficiency λ_{EF} (μm/g) was determined as the dissolved microprojection height to the dissolved metal layer mass Δm ratio:

$$\lambda_{EF} = \frac{R_{ZH} - R_{ZK}}{\Delta m}.$$

The value of λ_{EF} allows to one compare various treatment processes: the quicker the decrease of the surface microirregularity height with the smaller the removal of metal, the more effective the process is. The polishing efficiency was also determined taking into account the change of reflectivity ΔOC:

$$\lambda_{EFOC} = \frac{\Delta R_Z}{\Delta m} \times \Delta OC.$$

The efficiency of the finishing of the ECP process by current unipolar pulses under different conditions of treatment was investigated in the first stage. The current pulse duration was varied in the range of $(0.1–5) \times 10^{-3}$ s at a pulse ratio from 1 to 8. The current density changed from 0.25 to 5 A/cm^2. The specimens were jewelry and molded plates of ZeelEserEm 58.5-8 alloy with sizes of $5 \times 10 \times 0.2$ mm that had undergone machining. The investigation was carried out at room temperature (20°C) and in heated electrolytes (60°C) with agitation and without it.

The ECP efficiency depending on the initial surface roughness was determined in the second stage. Parallelepipeds with flat sides and with three complex shaped casts on one of the sides were the specimens (Fig. 2). The specimen surface was subjected to different preprocess operations:

(1) a through mechanical method with a hand tool; the initial surface microroughness was $R_{Zin} = 0.84 \times 10^{-6}$ m;

(2) a through mechanical method by means of a cohesive abrasive material (emery paper no. 320); $R_{Zin} = 0.59 \times 10^{-6}$ m;

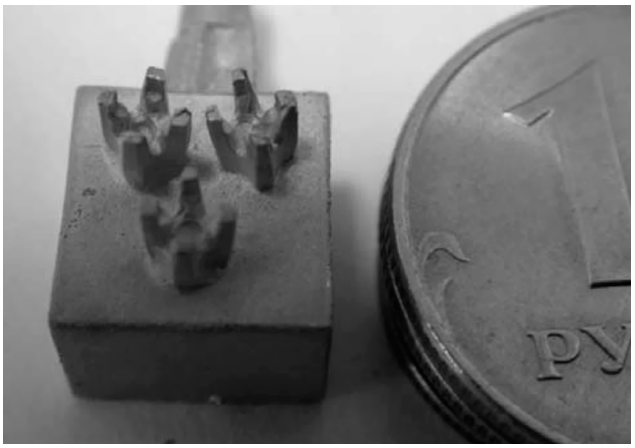

Fig. 2. External view of the specimen at the second experimental stage.

(3) the surface wasn't preprocessed after casting; $R_{Zin} = 0.3 \times 10^{-6}$ m.

The specimen surface was polished using the following ATPCP:

—unipolar ones with duration of 3×10^{-3} s; pulse ratio 1.25; current amplitude density 3–5 A/dm^2;

—bipolar ones with the direct pulse duration of 3×10^{-3} s; pulse ratio 1.25; the back pulse duration 0.5×10^{-3} s; the current amplitude density in the pulses 3–5 A/dm^2.

The ECP was carried out until the termination of the surface microroughness decrease. The surface microroughness and reflectance (luster), as well as the specimen mass, were measured every 20 seconds.

At the third stage, the specimens were manufactured using casting according to the melted patterns and their eye rings were made using stamping (the alloy ZeelEserEm 58.5-8, the noncorrosive master alloy Legor 14K OR129C). The specimen surface shape permitted one to record the differences of the polishing quality of the regions with unequal accessibility for the abrasive material (Fig. 3). The specimen surface was treated according to various operational procedures simulating a production run. The following operations were used as preparatory ones:

—mechanical working with a hand tool (needle files, tidal waves, etc.)—PH;

—mechanical working with a cohesive abradant (polishing paper no. 320—П320 and no. 600—П600);

—the castings being of high quality and not requiring mechanical working—PWT.

There were used the following transitory and terminal operations:

—working on a grinding-and-polishing machine—TGPM;

—tumbling using a spinning disc machine (SDM)—TT;

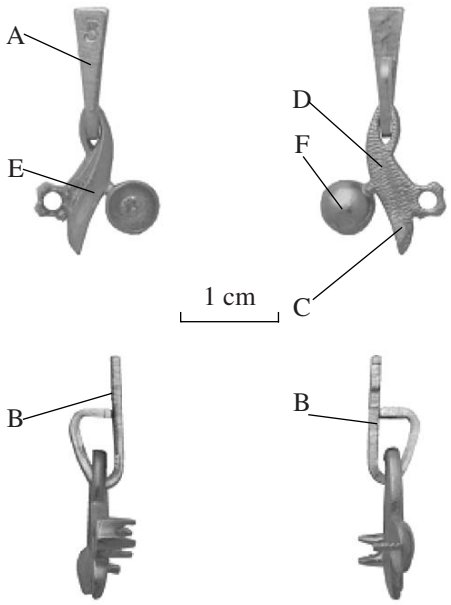

Fig. 3. External view of the specimen at the third experimental stage and the areas of the surface: A—the stamped surface, B—the stamp cut place, C—the flow gate cut-off place, D—the previously textured surface, E—the main easily accessible surface (the leaflet plate surface), and F—the surface of a pearl setting cup.

—ECP employing unipolar pulse currents—TUC;

—ECP employing bipolar pulse currents—TBC.

There were used the following finishing operations:

—working on a grinding-and-polishing machine—FGPM;

—tumbling using a GPM—FT;

—ECT employing unipolar pulse currents—FUC;

—ECT employing bipolar pulse currents—FBC.

Spinning disc finishing machine tools (OTEC) of the CF-18 series were used for tumbling with the following operation sequence:

at TT:

(1) wet tumbling with KX10 and PX10 white plastic chips (of 50% of each) for 6 hours,

(2) dry tumbling with H1/50 nutshell grains for 6 hours,

(3) dry tumbling with H1/500 nutshell grains for 4 hours;

at FT:

(1) dry tumbling with H1/50 nutshell grains for 4 hours,

(2) dry tumbling with H1/500 nutshell grains for 4 hours.

Three specimens were worked in parallel in each case. The average values for the group were determined after every stage of the experiment. Measurements were taken of six areas: on the stamped surface (Fig. 3, A), on the stamp cut place (Fig. 3, B), on the flow gate cut-off

Table 1. Composition of the studied alloys

Alloy trade mark	Alloy color	Alloy composition					
		Au	Ag	Cu	Ni	Zn	In
[ZeelEserEm]585	Red	59.50	5.77	33.80	–	0.93	–
[ZeelEserEm]585	Yellow	58.31	31.14	10.56	–	–	–
[ZeelEserEnTseEm]585	White	60.20	1.16	26.66	5.70	5.81	0.47

place (Fig. 3, C), on the previously textured surface (Fig. 3, D), on the easily accessible surface (the leaflet plate surface) (Fig. 3, E), and on the surface of a pearl setting cup (Fig. 3, F). The luster was visually noted on the inner side of the cast. The same amount of electricity was passed through the anode at the ECP by unipolar and bipolar currents.

At the fourth stage, there was studied the surface electrochemical grindability of the alloys based on golds of various colors—red, white, and European (yellow) ones. The grades of the master alloys and alloy compositions are presented in Table 1. The specimens were made by molding according to melted patterns (Fig. 2). The electrolyte temperature was 20–35°C.

Experimental Results and Their Discussion

The first stage. The decrease of the R_Z value stops after treatment for 40–50 s: it settles at a relatively constant level with the proceeding metal removal (Fig. 4); i.e., there exists an optimum duration of the ECP finishing process. Longer treatment is pointless, as it is necessary to avoid the excessive removal of the precious metal without improvement of the surface quality.

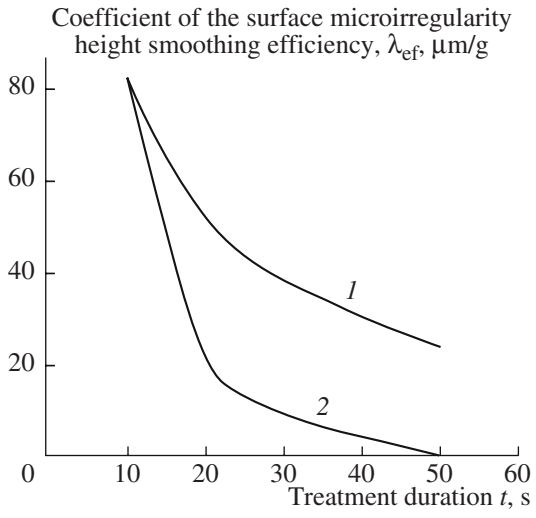

Fig. 4. Relationship between the polished surface microirregularity height smoothing efficiency and the duration of the finishing ECP by unipolar current pulses: *1*—with respect to the initial value, *2*—with respect to the previous value.

The surface of both the specimens and the finished jewelry was effectively polished under the optimum conditions of the treatment and did not affect the quality of the jewellery mountings of phianite and the first group of stones. The setting quality doesn't worsen as the metal removal is negligible during the ECP finishing.

The agitation of the electrolyte doesn't substantially influence the ECP. Yet, with such suspension clips as clamps and hangers being used, thermal damage and erosion pits could occur on the surface of the specimens and articles in the region of their contact with the hanger. In addition, the articles can be expulsed to the electrolyte surface as a result of the active gas release. The contact of the hanger with an article can cause its spoilage, as there is generated a pale film on its surface. Suspension clips in the form of baskets are employed to avoid these undesirable phenomena. Thermal damage is only absent in the case of the baskets' continuous swinging, so the uninterrupted alternating displacement of the hanger during the ECP process is necessary [9,10].

The second stage. The change of the relative smoothing of the surface and its microirregularity height is presented as diagrams in Figs. 5 and 6.

The changes of the surfaces of the casts and the surface of the specimen between them were checked visually. The prong surface smoothed and took on a luster

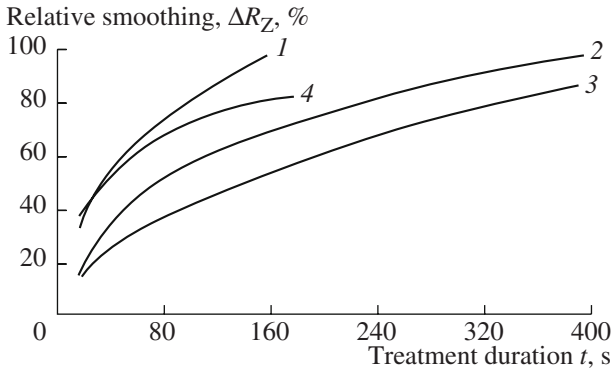

Fig. 5. The variation of the relative smoothing of the specimen surface microirregularities due to ECP with the treatment duration: *1*—ECP by bipolar pulses without the preprocess treatment; *2*—ECP by unipolar pulses without the preprocess treatment; *3*—ECP by unipolar pulses with the preprocess treatment with emery paper; *4*—ECP by unipolar pulses with the preprocess treatment with a needle file.

within only 60 s under the unipolar conditions and within 40 s under the bipolar conditions. The surface between the casts gained the final microroughness ($R_Z = 0.01 \times 10^{-6}$ m) only after 7 min under the unipolar conditions, and, after 3 min under the bipolar conditions, the sharp edges of the specimens and casts rounded up. The rough defects that appeared during the casting (pores, scars, etc) decreased in size but remained. This manifests the smoothing of the microbut not macroirregularities, which is typical of ECP.

Furthermore, there appear microclinks around the pores in the course of ECP under the unipolar conditions, which are gradually polished away and disappear. Their development is evidently caused by the generation of gas bubbles on the pore edges as a result of anode processes. Such microclinks don't form under the bipolar conditions of treatment, which could be explained by the removal of gas bubbles at the back current pulse. Residual surface microclinks represent a negative factor, as larger clinks could appear on this basis in the course of further treatment.

The treatment under a bipolar regime is the most efficient. It is half as long, and the metal removal is substantially smaller. The treatment under the unipolar regime with PH with a needle file is second in efficiency. The height of the microirregularities significantly reduces, though its final value is large $R_Z = 0.14 \times 10^{-6}$ m. Such a surface requires additional smoothing using SDM.

The third stage. The experiment showed that the results of polishing by different ways were commensurable on the areas accessible for the abradant. Basically, another result was obtained on the cast's internal side not accessible for the abrasive material; here, the reduction of roughness is possible only due to ECP.

The comparison of the λ_{EF} values for various treatments shows that the treatment efficiency diminishes in the following order: tumbling—ECP by bipolar currents—ECP by unipolar currents—hand polishing. The result is predictable and related to the fact that, at tumbling, the metal is "smeared" over the surface but not removed from it and λ_{EF} is higher than at other treatments.

The lowest treatment efficiency is observed for the sequences PWT–TT–FBC and PWT–TT–FUC. It is related to the fact that, after tumbling, the surface is smoothed and microirregularities are "smeared" by metal. Sustained ECP (for more than 40–80 s) has a restricted effect in this case, as the height of the microirregularities diminishes relatively rapidly and settles at a high enough level due to the disclosure of the "smeared" microirregularities, and there appears the lemon peel effect with the surface luster significantly growing with its obvious unevenness.

Let's compare the efficiency of the following sequences of treatments: PH–TBC–FT, P600–TBC–FT, and P320–TBC–FT. The use of the first sequence is more efficient, as the initial microroughness is higher after having been worked with a needle file, there are no

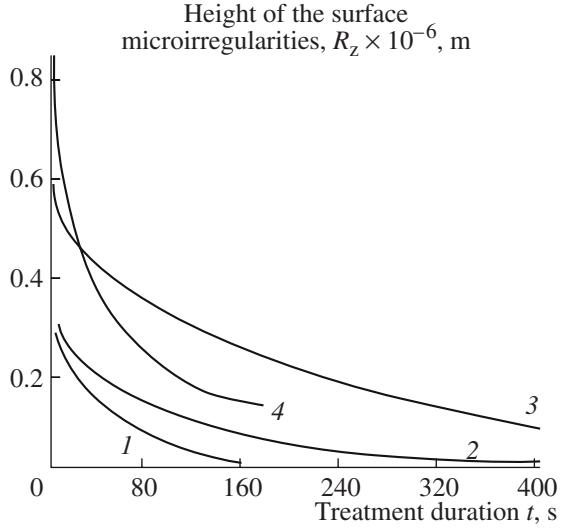

Fig. 6. The variation of the height of the specimen surface microirregularities due to ECP with the treatment duration: *1*—ECP by bipolar pulses without the preprocess treatment; *2*—ECP by unipolar pulses without the preprocess treatment; *3*—ECP by unipolar pulses with the preprocess treatment by emery paper; *4*—ECP by unipolar pulses with the preprocess treatment by a needle file.

smeared metal micropits, and the rate of smoothing of large microprojections at ECP is higher than of small ones. The efficiency of the third sequence is slightly higher than of the second one. This can be explained by the fact that, after working with polishing paper no. 320, the initial surface microroughness height is higher before ECP as compared with working with paper no. 600 and it is smoothed more rapidly.

The sequences PWT–TBC and PWT–TUC are more efficient than the other job sequences, and PWT–TBC is more efficient than PWT–TUC due to the substantially less metal removal with the same final surface microroughness.

The efficiency of the microrelief smoothing is not the same on the specimen surface areas subjected to the different PT. The less the after-casting surface is mechanically worked with a needle file or polishing paper, the more efficient the ECP is. If high-quality casting is used, the preprocess mechanical working should be minimal and ECP and tumbling efficiently smooth the microirregularities. The same is true about the treatment of the not easily accessible areas of the surface, for example, inside the casts. They shouldn't be subjected to mechanical working—only to ECP.

In some cases, the finishing tumbling after ECP reduces the height of the surface microirregularities as at ECP; it is impossible to endlessly decrease the height from a substantial initial value. Within some time, this height becomes steady, and, hereafter, the microroughness remains more or less constant with the metal continuing to be removed or even worsens because of the surface intergranular pickling due to the continuing

Table 2. Efficiency of ECP of the studied alloys

Number of order	Alloy trade-mark	Alloy color	ECP regim	ΔR_Z	λ_{EF}	λ_{EFR}
1	[ZeelEserEm]585	Red	Optimum for the given alloy	0.201	6.484	14.33
2	[ZeelEserEm]585	Yellow		0.201	4.351	9.22
3	[ZeelEserEnTseEm]585	White		0.192	3.582	6.05
4			Optimum for alloys 1 and 2	0.190	3.558	5.76

anode dissolution [6]. To determine the most efficient process duration, the ECP length was specially chosen in the experiment to be more than the optimum one. When the optimum ECP length is exceeded, the surface quality worsens.

It is important to note that, when choosing the job sequence, it is necessary to consider whether the surfaces being worked are figurine-shaped ones. There exist several classes of products whose surfaces can't be subjected to tumbling or such treatment is rather difficult [11], for instance, products with complex casts and undercuts. The visual control of the internal surfaces of casts and the cups for pearl settings after using different job sequences shows that these surfaces take on a luster only at ECP. In addition, the thinning and the change of the protruding details (the cast prongs and the dowel bars used to set a pearl) after ECP are minimum.

The differences in the metal rejects' regeneration at various treatment regimes are also interesting from the point of view of economy. The nonrecoverable metal rejects after working using GPM (using a grinding–polishing machine) may amount up to 40%; after working using SDM, up to 20%; and, after ECP, up to 1.5%. Thus, from this point of view, it is more profitable to carry out the main surface smoothing and metal removal with ECP.

The average reflectance (and luster) of the worked surface reduces in the following order: ECP by bipolar currents (4.88 r.u.) (r.u. = relative units)—ECP by unipolar currents (4.64 r.u.)—Tumbling (4.27 r.u.)—Hand polishing using GPM (4.06 r.u.). By using GPM, it could be quicker to polish those areas that first "catch the eye" at the examination of the article, for example, the main surface (Fig. 3, E) and the surface of the cup for the pearl setting (Fig. 3, F).

The obtained results basically support the proposition that the decrease of the height of the surface microirregularities causes an increase of the reflectance. Yet, the suggested procedure of the reflectance evaluation [7] takes into account the dispersion of microirregularities throughout the height (the more the dispersion, the less the reflectance).

Thus, the reflectance growth dynamics and the specimen surface microroughness decrease, as well as the treatment process efficiency, when various job sequences are used. This allows one to contend that the use of high-quality castings permits dropping the previous jobs of the surface smoothing with abrasive materials, the further surface smoothing by ECP bipolar pulse currents, refinement using SDM, and finishing EHP by bipolar currents. If work stocks are obtained through stamping, ECP is more efficient than hand polishing using GPM and needle files.

The fourth stage. The values of ΔR_Z, λ_{EF}, and λ_{EFR} (the efficiency of the reflectivity) under optimal ECP regimes are presented in Table 2.

The greater the temperature is in the range from 20 to 35°C, the quicker the alloy polishing is, yet the minimum roughness isn't achieved. A temperature from 20–25°C is the optimum one.

The surface reflectance proceeds growing at the second (sometimes at the fifth) minute of treatment, though the surface roughness worsens due to the partial picking. Consequently, the treatment efficiency decreases after three minutes.

White gold is polished slower than red and yellow gold with all the other factors being the same. The minimum roughness forms on it within 4 minutes. For the studied parameter ranges, the grindability drops in the following order: red—yellow—white gold; i.e., there exists a distinctly pronounced relation between the grindability and the alloy composition.

The microstructures of the alloys were analyzed to support this proposition.

Red gold alloy. The alloy structure consists of two phases (Fig. 7, a). The first one represented by light grains is a solid solution of copper and silver in gold. The second phase (the darker one) is most probably a mechanical mixture of a solid solution of copper and silver in gold with an intermetallide. The intermetallide Cu_3Au is the most possible.

Yellow gold alloy. The alloy structure is also two-phase (Fig. 7, b). The first one represented by light grains is (as for the red alloy) a solid solution of copper and silver in gold. The second phase (the darker one) is a mechanical mixture of a solid mixture of copper and silver in gold with the intermetallide CuAu or Cu_3Au. However, the sizes of the second phase are larger than for the red gold—the grains are branched and long.

White gold alloy. The alloy structure is also two-phase (Fig. 7, c), and the first, light phase is a solid solution of copper and silver in gold. The second phase is a mechanical mixture of intermetallides with the solid solution. The formation of the intermetallides Cu_3Au,

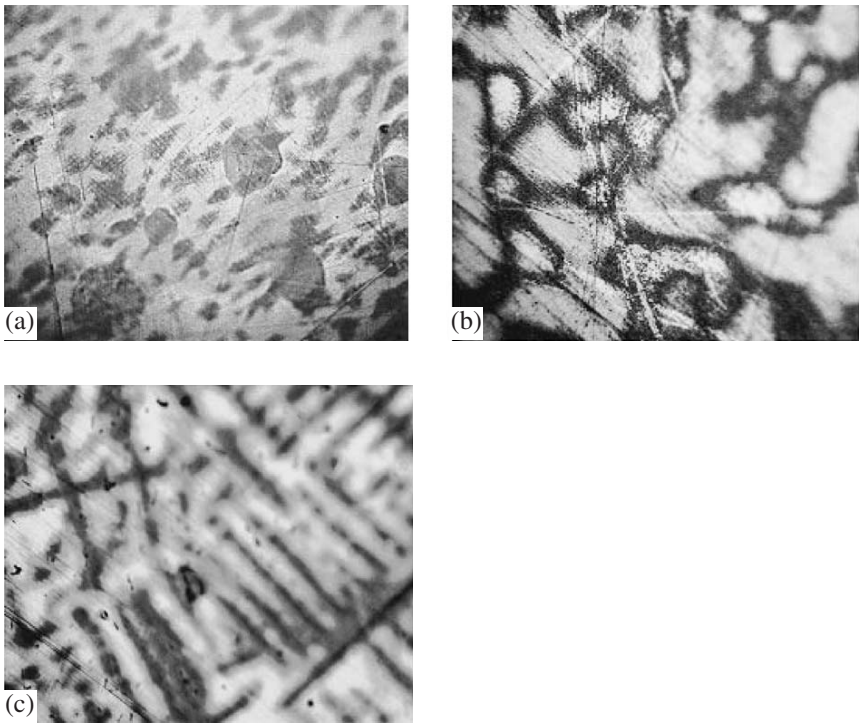

Fig. 7. Microsections of the studied alloys of gold: (a)—ZeelEserEm 585 (red), (b)—ZeelEserEm 585 (yellow), (c)—ZeelEserEm 585 (white).

CuZn, and other representatives of the Cu-Zn family is possible here. The second phase grain shape is more elongated and needlelike and exceeds the grains of the yellow and red alloys by several times.

The examination of the microstructures shows that the grain size influences the grindability. The more developed and long the grains are, the less electrochemically uniform the surface at ECP is and the slower and worse the alloy is polished. During the process of jewelry production, there often arises the necessity of the simultaneous ECP of several gold alloys in the case when the article elements are connected into a single whole. Besides, at small volumes of work stocks from various alloys, it is desirable to conduct their simultaneous ECP. In these cases, it is possible to perform the treatment under the conditions optimum for red and yellow gold. The deviations from the treatment efficiency for white gold are negligible in this case (Fig. 8, Table 2).

CONCLUTIONS

(1) The efficiency of ECP by pulse currents for treatment of figurine-shaped surfaces of jewelry work stocks in both the final and intermediate stages is shown.

(2) There exists an optimum duration of the finishing ECP process by unipolar current pulses. After 40–50 s of treatment, the decrease of the R_Z value stops: it becomes steady at a relatively constant level with the continuing metal removal. Consequently, it is pointless to perform longer treatment in order to avoid the excessive removal of the precious metal without refining the surface quality.

(3) It is impossible to carry out the electrochemical grinding and polishing of the surface at the same time during ECP, i.e., to endlessly reduce its roughness in the treatment process. ECP causes the improvement of the reflectance (luster) of the surface even if it is not

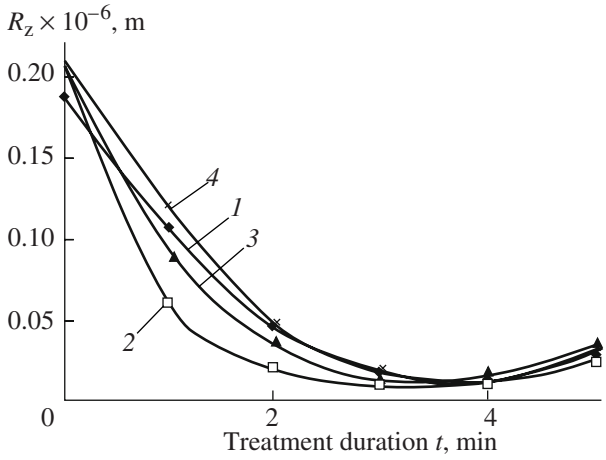

Fig. 8. Variation of the surface roughness of specimens from gold of various colors at treatment under the general regime: white *1*—the regime optimal for treatment of red and yellow gold and not optimal for white gold; yellow, red, white—regimes optimal for the treatment of the corresponding alloys. *1*—white *1*; *2*—yellow; *3*—red; *4*—white.

completely "smoothed"; i.e. microirregularities are removed on the macroirregular surface.

(4) ECP can be used as the finishing treatment under the following conditions:

—After the casting and the previous mechanical working, before ECP, the surface microroughness should exceed the value $R_Z = 0.3 \times 10^{-6}$ m (e.g., after working with emery paper no. 600–1200) to ensure the final microroughness $R_Z = 0.01 \times 10^{-6}$ m after ECP.

—The casting quality should provide the absence of a large number of pores on the surface.

—The finishing ECP duration should not exceed 20–40 s in order not to worsen the surface quality due to the disclosure of the surface regions "smeared" with metal during the earlier jobs.

(5) ECP can be used as an intermediate operation after casting according to melted patterns and stamping (ensuring high quality of the casts and the surface) with the following giving of luster in rotational-disc machines. Thanks to ECP, a sufficient luster is imparted to not easily accessible areas on the product surface.

(6) The ECP bipolar regime is much more efficient than the unipolar one: the smoothing of microirregularities occurs twice quicker, and the relative metal removal is twice less.

(7) The surface reflectance after ECP (under the condition that the height of the microirregularities is $R_Z = 0.01 \times 10^{-6}$ m) is higher than that of the surface polished using mechanical methods thanks to the larger uniformity of the remaining microirregularities with respect to their height.

(8) Alloys based on gold with various master alloys and colors can be efficiently electrochemically polished using bipolar current pulses. The optimum ECP regimes for various alloys based on gold in electrolytes of the same composition were determined experimentally.

REFERENCES

1. Shpital'skii, E.I., Russia Patent 45537, 1911.
2. Galanin, S.I., RF Patent 2184801, 2002.
3. Galanin, S.I., RF Patent 2288978, 2006.
4. Grilikhes, S,Ya., *Electrokhimicheskoe i khimicheskoe polirovanie: teoriya i praktika. Vliyanie na svoistva metallov* (Electrochemical and Chemical Polishing: Theory and Practice. Effect on Metal Properties), Leningrad: Mashinostroenie, 1987.
5. Galanin, S.I. and Kalinnikov, I.V., Polarization of Jewelry Gold Alloys by Bipolar Current Pulses in a Polishing Electrolyte, *Surf. Eng. Appl. Electrochem.*, 2008, vol. 44, no. 5, pp. 359–366.
6. Galanin, S.I., Sorokina, M.V., Tokmakov, A.Yu. and Subbotin, D.N., Efficiency of Various Processes of Gold Alloy 585 Grade Jewelry Surface Polishing, *Metalloobrabotka*, 2006, no. 4, pp. 20–25.
7. Galanin, S.I., Uspenskii, S.V., Sorokina, M.V., Lomagin, V.N. and Subbotin, D.N., Method of Determination of Surface Luster, *Vestn. Kishinev. Gos. Univ.*, 2006, no. 13, pp. 71–74.
8. Galanin, S.I., Uspenskii, S.V., Galanina, A.S. and Agafonov, V.O., Methods of Determination of Metal Surface Optic Characteristics, *Vestn. Kishinev. Gos. Univ.*, 2008, no. 17, pp. 119-123.
9. Galanin, S.I. and Uspenskii, S.V., Electrochemical Polishing of the ZeelEserEm 585-80 Alloy Surface Polishing by Bipolar Current Pulses, *Metalloobrabotka*, 2005, no. 2, pp. 10–13.
10. Galanin, S.I., Sorokina, M.V. and Tokmakov, A.Yu., Electrochemical Polishing of Jewelry Surface Using Pulse Currents, *Materialy 4-go mezhdunarodnogo simposiuma yuvelirov "Traditsii, innovatsii i perspektivy sovremennogo yuvelirnogo proizvodstva"*, (Proc. 4th Int. Symposium of Jewelers "Traditions, Innovations and Prospects of the Modern Jewelry Production"), Saint-Petersburg, 2005, pp. 186–198.
11. Galanin, S.I., Sorokina, M.V. and Tokmakov, A.Yu., Jewelry Design Considering Finishing Technologies, *Yuvelirnoe obozr.*, 2005, no. 4, pp. 28–30.
12. Galanin, S.I., Sorokina, M.V. and Galanina, A.S., Electrochemical Polishing of Jewellery Gold Alloys by Bipolar Current Pulses, *Fiz. Khim. Obrab. Mater.*, 2007, no. 5, pp. 67–71.
13. Galanin, S.I., Sorokina, M.V. and Galanina, A.S., Features of Electrochemical Polishing of Gold Alloys of Various Colors, *Materialy 2-i MNTK "Electrokhimicheskie i electrolitno-plazmennye metody modifikatsii metallicheskikh povernostei"* (Proc. 2nd ISTC "Electrochemical and Electrolyte-Plasma Methods of Metal Surface Modification"), Kostroma–Moscow, 2007, pp. 77–79.

ISSN 1068-3755, Surface Engineering and Applied Electrochemistry, 2009, Vol. 45, No. 2, pp. 93–97. © Allerton Press, Inc., 2009.
Original Russian Text © O.A. Beshentseva, V.D. Kalugin, N.S. Opaleva, 2009, published in Elektronnaya Obrabotka Materialov, 2009, No. 2, pp. 19–24.

ELECTRICAL METHODS OF SURFACE PROCESSING

Effects of the Liquid Medium Composition in the System of Chemical Tin Deposition on the Dielectric According to the Reaction of Disproportion under Convection Diffusion Conditions

O. A. Beshentseva[a], V. D. Kalugin[b], and N. S. Opaleva[b]

[a]*Kharkov National Automobile and Highway University, 25 Petrovskaya str., Kharkov, 61022 Ukraine*
[b]*Institute for Chemistry at Kharkov V.N. Karasin National University, Svobody sq., Kharkov, 61077 Ukraine*
e-mail: kalugin.v.d@mail.ru

Received November 11, 2008

Abstract—For the first time, there were determined the specific effects of the solutions' chemical metallization composition on the rate of chemical tinning, the phase composition, and the electroconductivity of tin deposits based on the NaOH concentration and indifferent electrolytes (NaCl and Na_2SO_4). The optimal values of the concentrations of the tinning solution components ($SnCl_2$, NaOH, and NaCl) and the temperature were defined. It was shown that the reaction of disproportion yields to the main mechanisms of heterogeneous oxidation reduction reactions (the rule of Van't Hoff is complied with). The possibility of the chemical tinning processes' intensification, along with the deposited coating quality improvement, on the basis of the determined new effects has been assumed.

DOI: 10.3103/S1068375509020033

INTRODUCTION

One of the major problems in physical chemistry and physicochemical materials science is the study of the processes of the chemical metallization of the dielectric (D) surfaces of metals (Me). The chemical tinning of dielectrics has been insufficiently studied [1, 2 and 3]; therefore, in the process of the examination of the kinetics of this phenomenon under the conditions of convectional diffusion, new factors are likely to be found that can be used for the metallization process intensification and obtaining of coatings with the required functional properties. The purpose of the present paper is to examine the influence of the solutions composition (the reagent concentration and pH) and the conditions (the temperature and catalysis) of D metallization upon the kinetic peculiarities of D chemical tinning and the phase composition and electrophysical properties of Sn layers formed under conditions of convection diffusion.

The chemical reduction of Sn(II) ions on an activated dielectric according to the reaction of disproportion can be actually performed in the mode of "internal" electrolysis, when the process is realized under a closed (on the catalyst surface) oxidation-reduction reaction, which determines the electrochemical nature of the process on the whole.

METHODS OF INVESTIGATION

The study of tin chemical deposition was carried out in constant volumes of the solution ($v = 150$ ml) on glass specimen tubes with $l = 0.08$ m and $d = 0.01$ m. The surface of the D specimens was degreased and activated according to the standard techniques [4]. Prior to and after the experiment, the rate of the chemical tinning was estimated by means of the specimens' weighing. The time of the chemical deposition τ in all the experiments was 50 minutes. The electrical resistance of the Me deposits was measured by the double-contact method with the help of an R-5010 alternating current bridge. Roentgen diffractograms of the Sn coatings were taken using a DRON-1.5 diffractometer with CuK_α radiation (with an Ni filter) [5]. At the preset parameters, the tests were performed no less than 5 times with the V_{Sn} values' convergence being satisfactory (with a relative error of up to 0.5%). The solutions were prepared from reagents of "pure for analysis" or "chemically pure" quality using twice-distilled water.

RESULTS AND DISCUSSION

According to our notion of the catalytically active centers (CAC) of the palladium atoms (under the condition of the absence of a more strong reducing agent), in the solution there occurs Sn(II) particles distributed along E_α activation energy levels onto groups with more pronounced oxidation and reduction properties. Therefore, the interaction between the particles with

Ionic composition of the chemical tinning solution

Sn^{2+}	OH^-	Cl^-	Chemical formula of a particle	log*K*	Concentration of particles, mol/l
1	1	0	$Sn(OH)^+$	9.95	5.2×10^{-17}
1	2	0	$Sn(OH)_2$	20.03	2.4×10^{-6}
1	3	0	$Sn(OH)_3^-$	24.68	4×10^{-1}
2	2	0	$Sn_2(OH)_2^{2+}$	22.62	1.9×10^{-22}
4	3	0	$Sn_4(OH)_3^{5+}$	47.75	1.9×10^{-22}
4	4	0	$Sn_4(OH)_4^{4+}$	28.22	1.9×10^{-22}
1	0	1	$SnCl^+$	1.17	1.9×10^{-22}
1	0	2	$SnCl_2$	1.72	1.9×10^{-22}
1	0	3	$SnCl_3^-$	1.7	1.9×10^{-22}
1	0	4	$Sn_2Cl_4^{2-}$	2.3	1.9×10^{-22}
0	1	0	H^+	–14	3.8×10^{-14}
1	0	0	Sn^{2+}	–	1.9×10^{-22}

different E_α levels on CAC entails the acts of oxidation and reduction of Sn(II) particles up to the metal (according to the pattern of a disproportion reaction).

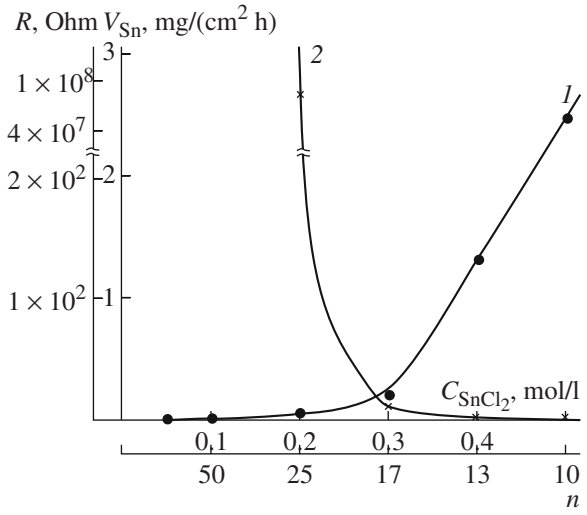

Fig. 1. The influence of $SnCl_2$ on the chemical tinning rate (V_{Sn}) and the specific electroresistance of the tin layers (R). The solution composition (mol/l): $SnCl_2 \cdot 2H_2O$–(0.0–0.5), NaOH–5.0. The conditions: T(K) = 333–358; τ(s) = 3000. Designations: *1*—V_{Sn}, *2*—R.

Since the process of the catalytic tin deposition according to the reaction

$$2Na_2[Sn(OH)_4] = Sn + Na_2[Sn(OH)_6] + 2NaOH \quad (1)$$

is rather complicated and depends on the composition of the solution and the conditions of the process realization, there was examined the influence of the concentrations of $C_{(SnCl_2)}$ and $C_{(NaOH)}$, where $C_{(SnCl_2)}$ and $C_{(NaOH)}$ are the concentrations of tin chloride and NaOH, correspondingly. Also, the influence of the temperature under conditions of convectional diffusion upon the rate of the chemical reduction of tin (V_{Sn}), the phase composition, and the electrical resistance (R) of the deposited Sn layers was examined.

The influence of complex-formation processes of Sn(II)-containing particles in alkaline solutions on V_{Sn} was studied at $C_{(SnCl_2)}$ = 0–0.5 mol/l against the background of constant $C_{(NaOH)}$ = 5 mol/l. The rate of the chemical reaction of tin reduction at T = const is directly proportional to the concentration of Sn(II)- and OH^- particles and depends on the potential of $[Sn(OH)_x]^{2-x}$ complexes reduction. The higher the concentrations of OH^- ions in the solution, the stronger the Sn(II) complex and the higher the discharge polarization of $[Sn(OH))_x]^{2-x}$ but the lower the chemical deposition rate [6].

In order to determine the nature of the complex particles in the preset composition solution in the solution–CAC interphase layer, there was performed a computation (using the CLINP program) of the ionic composition of the chemical tinning solution, the results of which are presented in the table. One may see from the table that the tin in the chemical tinning solution is in the form of a complex $Sn(OH)_3^-$ ion. Therefore, the offered reaction of disproportion 2Sn(II) = Sn(0) + Sn(IV) may occur according to the equation

$$2Na[Sn(OH)_3] = Sn + Na[Sn(OH)_5] + NaOH. \quad (2)$$

It was found that the complex formation in these solutions is characterized by the correlation $n = C_{(NaOH)}/C_{(SnCl_2)}$. Hence, a double-level abscissa is depicted for the dependencies V_{Sn}–$C_{(SnCl_2)}$ and V_{Sn}–$C_{(NaOH)}$ (Fig. 1): along the first level is $C(SnCl_2)$, and along the second is n. It was determined that the process of chemical reduction is efficiently realized within the interval of n = 11–14, with the formation of compact Sn deposits having good adhesion suitable for technological use. The coatings' quality rating and their adhesion with the basis show that the optimum interval for $C_{(SnCl_2)}$ is 0.36–0.4 mol/l.

Since, within the limits of $C_{(SnCl_2)} \geq 0.5$ mol/l, there was observed a chemical decomposition of the metal lay-

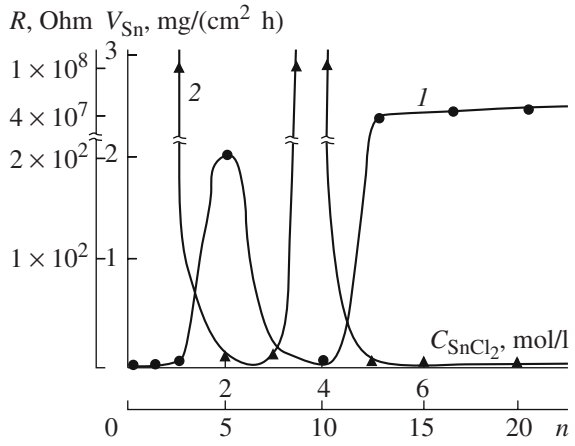

Fig. 2. The influence of the NaOH concentration on the chemical tinning rate (V_{Sn}) and the specific electroresistance of the tin layers (R). The solution composition (mol/l): $SnCl_2 \cdot 2H_2O$–0.4, NaOH–(0–8). The conditions: T(K) = 333–358; τ(s) = 3000; ω(rot./min.) = 0. Designations: *1*—V_{Sn}, *2*—R.

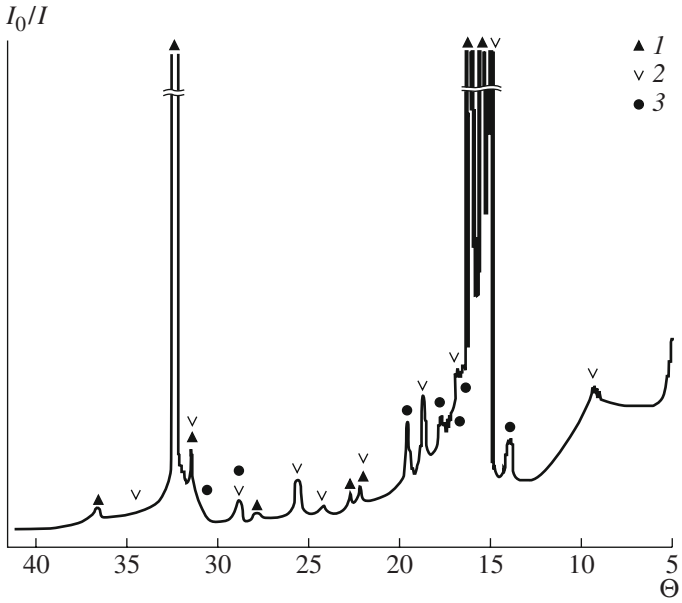

Fig. 3. Roentgen diffractogram of chemically deposited tin on a dielectric (glass). The solution composition (mol/l): $SnCl_2 \cdot 2H_2O$–0.4, NaOH–2.0. Designations: ▲—β-Sn; v—SnO; ●—impurity phase.

ers due to which a considerable V_{Sn} decrease was registered, this phenomenon was examined by studying the dependency V_{Sn}–$C_{(NaOH)}$ at $C_{(SnCl_2)}$ = 0.4 mol/l (Fig. 2). As becomes clear from Fig. 2, the dependencies V_{Sn}–$C_{(NaOH)}$ and R–$C_{(NaOH)}$ have an opposite character and become stable (coincide satisfactorily with the table data) at $C_{(NaOH)}$ > 5 mol/l. The observed complicated character of the V_{Sn}–$C_{(NaOH)}$ dependency is probably connected with reduction difficulties associated with Sn(II) complexes containing a small quantity of OH^- particles and a great number of Cl^- ions.

For deeper insight into the causes of such a peculiar trend of the V_{Sn}–$C_{(NaOH)}$ curve, one may obtain some information from the sediment analysis. With this aim, there was carried out a roentgen phase analysis of the chemically deposited layers from the solutions with alkaline concentration of 2 and 5 mol/l.

We failed to make a roentgenograph of the deposits obtained at $C_{(NaOH)}$ = 3.75 mol/l because of their very small amount.

The analysis of the diffractograms showed that the sediment obtained at $C_{(NaOH)}$ = 2 mol/l, besides the main β-Sn phase, comprised the SnO phase and an impurity phase of unknown composition (Fig. 3). The sediment obtained at $C_{(NaOH)}$ = 5 mol/l only contains the β-Sn phase (Fig. 4).

The impurity phase nature is very hard to identify. Perhaps, they are hydroxochloride compounds of tin. The electroconductivity of such a coating is lower than that of a pure Sn layer deposited from the solution with $C_{(NaOH)}$ = 5 mol/l and over. For practical purposes, it is worthwhile to use the solutions with $C_{(NaOH)}$ = 5–6.25 mol/l, since, at $C_{(NaOH)}$ > 6.25 mol/l, there occurs intense chemical dilution of the Sn sediment.

With regard to the X-Ray diffractometry data on the tin sediment composition (Fig. 3 and 4) and the results of the calculations of the ionic composition of the initial solution (see the table), one may reveal the nature of the Sn(II) particles that are reduced on CAC within the region of $C_{(NaOH)}$ = 2.0–3.5 mol/l (Fig. 2) prior to the heavily complexed Sn(II) particles formation. There-

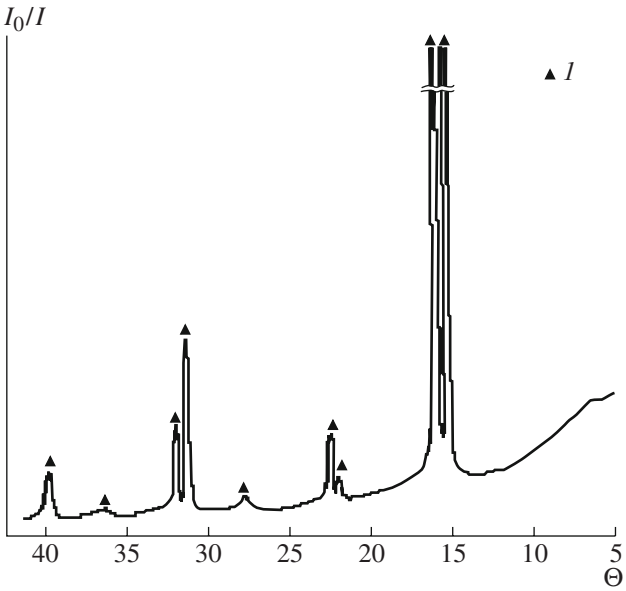

Fig. 4. Roentgen diffractogram of chemically deposited tin on a dielectric (glass). The solution composition (mol/l): $SnCl_2 \cdot 2H_2O$-0.4; NaOH-5.0. Designations: ▲—β-Sn.

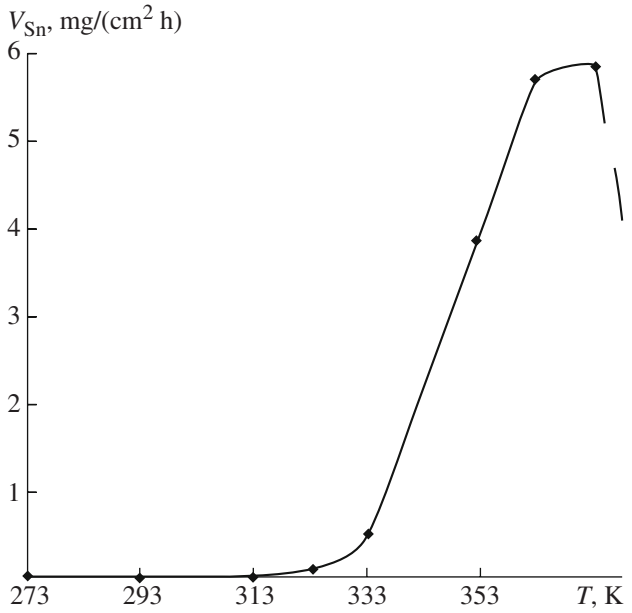

Fig. 5. The temperature influence on the rate (V_{Sn}) of the chemical reduction of tin. The solution composition (mol/l): $SnCl_2 \cdot 2H_2O$–0.4; NaOH–5.0. Conditions: T(K) = 333–358; τ(s) = 3000.

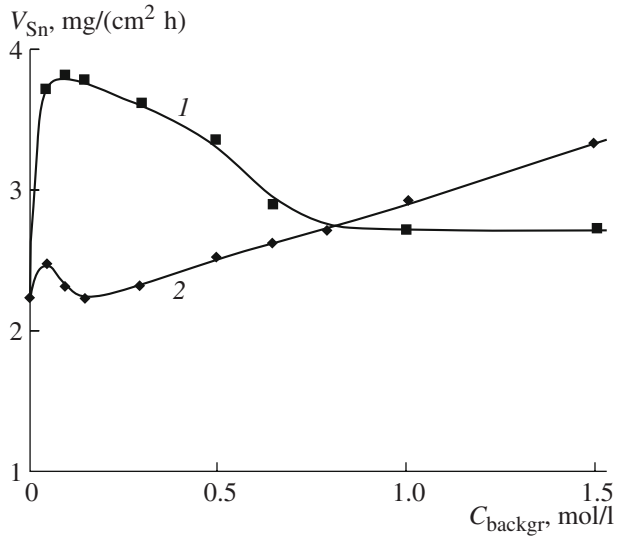

Fig. 6. The influence of the concentrations of the background electrolytes on the chemical deposition of tin. The solution composition (mol/l): $SnCl_2 \cdot 2H_2O$–0.4; NaOH–5.0. Conditions: T(K) = 333–358; τ(s) = 3000. Anions: *1*—Cl^-; *2*—SO_4^{2-}.

fore, in this region of alkaline concentrations, only colloidal $Sn(OH)_2$ particles may appear, which are reduced and form a sediment of grey-steely color. It may happen that the sediment also comprises $Sn(OH)_2$ particles in the process of formation.

Taking into account that the chemical tinning process in the $SnCl_2$–NaOH–H_2O system can be realized only at high temperatures, there was examined the dependency of V_{Sn}–T (Fig. 5). As a result of the investigations, a linear dependency of V_{Sn}–T was determined. It should be noted that, in the temperature range of 60–85°C, the formation of fine-crystal compact deposits is observed. At 85–90°C, the deposits are crumbly, porous, dissolve in alkali in 23–30 min., and slip down the glass substrate. According to our estimates, the V_{Sn}–T dependency obeys the Van't Hoff law (the temperature coefficient of the rate is γ = 2). The temperature range of 70–80°C can be considered optimal for the process, when the phenomena that deteriorate the sediment properties develop insignificantly.

As a result of the investigations, the following composition for the chemical tinning solution of D (mol/l) is offered: $SnCl_2 \cdot 2H_2O$–0.4; NaOH–5.0. The temperature range of the solution is 343–358 K, and the deposition time is 3000 s. The coating thickness on D under such conditions may amount to 3.5–4.0 mkm.

In order to accelerate the delivery of reactionally active particles of metal to the CAC, various methods can be used: in the regime of the diffusion rate increase, by means of forced hydrodynamic transport of ions to the active surface of the D and due to the physical adsorption effects application. The latter case of accelerated delivery of electrochemically active particles is examined in solutions for chemical reduction with additives of various inorganic anions (at the level of background concentrations) that have opposite possibilities of adsorption on CAC. Therefore, for the investigations, there were chosen Cl^- and SO_4^{2-} anions in the concentrations intervals from zero to values close to those of saturated solutions (Fig. 6).

The maximum permissible concentrations of Na_2SO_4 and NaCl exceeded the concentration of the Sn salt by 1.25–2.0 times, respectively. As one can see from Fig. 6, in the case of introduction of small NaCl quantities (curve *1*), the rate of the chemical reduction increases approximately by 1.75 times. With a further increase of Cl^- ions, the process rate monotonically decreases, and, in the region of $C_{backgr.}$ = 0.75–1.5 mol/l, it does not change its character. In the case of SO_4^{2-} ions (curve *2*) at small concentrations, there is observed an insignificant increase of V_{Sn} (by 1.03 times) followed by some decrease and then a further monotone increase of the V_{Sn} chemical deposition (almost up to $C(Na_2SO_4)$ = 1 mol/l).

In our opinion, the explanation for the V–$C_{backgr.}$ dependency variations in the chemical tinning solutions containing Cl^- or SO_4^{2-} anions is connected with the peculiarity of Sn(II)-containing particles to form ($SnCl_2(OH)_2^{2-}$, $SnSO_4(OH)_2^{2-}$) complexes. These complexes considerably differ in their ability to be adsorbed on CAC due to the electrostatic interaction of the active

anionic constituent of the complex (Cl^- or SO_4^{2-}) with CAC (thus accelerating the delivery of particles to the activated surface), which leads to the increase of the metal chemical reduction rate. Since SO_4^{2-} anions are a constituent of a complex anion and exhibit no specific adsorption on CAC, the effect of the V_{Sn} increase in the presence of SO_4^{2-} ions in the solution is insignificant (as compared to the case of Cl^- ions). At the concentrations of the background salts of 0.6–0.7 mol/l, the V_{Sn} values for Cl^- and SO_4^{2-} anions are identical. This may suggest that, when the chemical reduction reaction is running in the regime of autocatalytic deposition on a newly formed surface of Sn, the surface effects of the concentration influence of the various anions' natures become leveled.

The previous investigations showed that the effects of V_{Sn} that increase with surface active substances (SAS) (Cl^-) introduction also considerably influence the properties of Me deposits. The latter have a light grey hue, a fine-crystalline structure, and good adhesion with D substrates. The coatings obtained from the solutions with SO_4^{2-} ions are dark grey and are of a more crumbly macrocrystalline structure, perhaps due to the inclusion of the solution components into the sediment structure.

CONCLUSION

There were determined the specific effects of the composition of chemical metallization solutions on the rate of chemical tinning, the phase composition, and the electroconductivity of tin deposits from the NaOH concentration and indifferent electrolytes (NaCl and Na_2SO_4). The optimal values of the concentrations of the tinning solution components ($SnCl_2$, NaOH, and NaCl) and the temperature were defined. It was shown that the reaction of disproportion yields to the main mechanisms of development of heterogeneous oxidation reduction reactions. The possibility of the chemical tinning processes intensification along with the deposited coating quality improvement on the basis of the determined effects is assumed.

REFERENCES

1. Kalugin, V.D., and Beshentseva, O.A., Process Regularities in Chemical Tinning of Dielectrics According the Reaction of Disproportion, Mezhdunarodnaya nauchnaya konferentsiya "Electrochemiya, galvanotekhnika i obrabotka poverkhnosti" (Proc.Int.Conf. "Electrochemistry, Electroplating and Surface Processing"), Moscow: Izd-vo MGU, 2001, p. 54.
2. Beshentseva, O.A., Kalugin, V.D., Kinetic Regularities of Chemical Tin Reduction Process on Dielectrics according to the Reaction of Disproportion, *Vestnik L'vovskogo Universiteta. Ser. Khimicheskaya*, 2002, issue 42, part 2, pp. 233—236.
3. Beshentseva, O.A., Kalugin, V.D., Influence of Solution Composition and Temperature on the Rate of Corrosive Attack of Chemically Deposited Tin Layers on Dielectrics and Physico-Mechanical Characteristic of Coatings, XII Vserossiiskoe soveshchanie "Sovershenstvovanie tekhnologii gal'vanicheskikh pokrytii" (Proc. XII Rus.Conf." Techology Impovement of Electroplated Coatings"), Kirov, 2003, pp. 17–18.
4. Shalkauskas, M. and Vashkyalis, A., *Chimicheskaya metallizatsiya plastmass* (Chemical Metallization of Plastic), Leningrad: Khimiya, 1985.
5. Gorelik, S.S., Rastorguev, L.N., and Skakov, Yu.A., *Rentgenograficheskii i elektronno-opticheskii analiz* (Roentgenographical and Electron-Optical Analysis), Moscow: Metallurgiya, 1970.
6. Akhmetov, N.S., *Obshchaya i neorganicheskaya khimiya* (General and Inorganic Chemistry), Moscow: Vysshaya shkola, 1980.

ISSN 1068-3755, Surface Engineering and Applied Electrochemistry, 2009, Vol. 45, No. 2, pp. 98–101. © Allerton Press, Inc., 2009.
Original Russian Text © E.K. Sevidova, V.N. Tsyuryupa, 2009, published in Elektronnaya Obrabotka Materialov, 2009, No. 2, pp. 25–28.

ELECTRICAL METHODS OF SURFACE PROCESSING

Study of the Corrosion-Protection Effect of Electrodeposited Coatings on Objects of Rapid Prototyping Technologies

E. K. Sevidova[a] and V. N. Tsyuryupa[b]

[a]*National Technical Institute Kharkov Polytechnical Institute, ul. Frunze 21, Kharkov, 61002 Ukraine*
e-mail: grinko@kpi.kharkov.ua
[b]*SE Malyshev Factory, ul. Plekhanovskaya 126, Khrakov, 61001 Ukraine*

Received December 3, 2008

Abstract—It is shown that metal composite materials based on stainless steel and bronze, which are used for the layer-by-layer synthesis of products by the method of selective laser sintering (SLS), can be reliably protected from corrosion by electrodeposited coatings. It is established that, at equal thickness of the coatings (~20 μm), the best characteristics in a 3% solution of NaCl are found for layers of chemically precipitated nickel, electrodeposited milky chromium, and a three-layer coating of Cu–Ni–Cr. The correlation between the corrosion and electrochemical activity of the coating materials and the value of the wetting angle for their surface and polar fluid is obtained.

DOI: 10.3103/S1068375509020045

INTRODUCTION

When products formed by one of the methods of rapid prototyping (RP) are used as functional models, special requirements are imposed on their surface, being determined by the application purpose.

In particular, at present, applying the method of selective laser sintering (SLS), forms and tool equipment for the cast molding of polymers are made of metal powders [1]. Their working face must correspond to exclusive standards on wear resistance, hardness, antifriction properties, and corrosion stability.

The current limitations in selection of construction materials in RP technologies and their structural features (resulting from one or another method of layer-by-layer synthesis) do not always ensure obtaining of optimum function–operation properties of the end product.

In view of the above, it appears necessary to carry out measures focused on improvement of the properties of the functional layer, including the use of coatings. Promising for use in RP objects are considered, first of all, chemical and electrodeposited coatings characterized by a wide range of mechanical and physicochemical properties and by relatively simple deposition techniques. The latter circumstance is of particular concern for products of RP technologies, for which the applicability of other techniques of coating deposition is often limited either by the temperature factor or by the complexity of the geometrical form of the product itself.

The aim of the present paper was to study the corrosion-protection effect of electrodeposited and chemical coatings as applied to metal products formed by one of the methods of RP technologies, in particular, SLS.

EXPERIMENTAL

The material of the SLS samples was a composite of stainless steel particles (85.3% Fe, 14.3% Cr, 0.3% Mn, and 0.1% Ni) and tin bronze (86.6 Cu, 10.7 Sn, 0.6 Pb, and 0.5 Zn), which is used for impregnation (infiltration) of a presintered sample at the second stage of preparation.

Before the deposition of the coatings, the sample surface was polished with an R800 abrasive cloth (~12 μm). We studied the coatings of chemical nickel (from acid electrolyte) in the initial and heat-treated states and of electrodeposited chromium deposited in the mode of milky and hard deposits. The coating thickness was ~20 μm.

The corrosion-protection effect of the coatings was estimated by the electrochemical method and according to the results of corrosion tests.

The electrochemical studies were carried out by means of a PI–50–1.1 pulse potentiostat. The protective power of the coatings was estimated by the values of the stationary corrosion potentials E_{corr} and by the characteristics of the polarization dependences j–E measured by a three-electrode circuit.

As a corrosion environment, we selected a 3% solution of NaCl, being one of the most aggressive and often applied in similar research of steel based samples.

The corrosion tests took into account the temperature factor: with the use of RP products as equipment for casting and press molding of polymer materials, the temperature of the latter may be within 100–150°C. Therefore, after a drop (V = 100 μl) of the 3% solution of NaCl was applied on the surface of the samples, they were placed into an exsiccator (a salt solution was pored on its bottom) and kept in a dry-air sterilizer at a temperature of

Values of the corrosion potentials E_{corr} of samples with coatings

Sample / potential	Initial, without coating	With coating				
		Ni_{chem}	$Ni_{chem, h/t}$	Cr_{hard}	Cr_{milk}	Cu + Ni + Cr_{br}
E_{corr} B	–0.37	–0.11	–0.19	–0.27	–0.16	–0.14

100°C for 20 h. After the tests, the corrosion damage of the surface was estimated by visual inspection with subsequent photographic recording and comparison of the corrosion damage areas.

In addition to the generally accepted criteria of the corrosion stability, in the present work, for the coating estimation, we used one more parameter—the surface wetting angle Q. According to [2], there is a correlation between the wetting angle and the energy characteristics of the surface σ. In turn, it is the surface energy determined by the number of noncompensated bonds of surface atoms that is responsible for the complex of properties (adsorption, adhesion, catalytic, tribological, etc.) influencing the physicochemical activity, including the corrosion one.

The wetting angles were measured by an earlier developed technique [3]. The wetting solution was distilled water.

RESULTS AND DISCUSSION

As could be expected, the most negative value of the corrosion potential E_{corr} was found for the initial sample (see the table), which affords grounds for a preliminary conclusion regarding its minimal corrosion stability in a 3% solution of NaCl.

All the studied coatings exhibit a protective effect shifting E_{corr} into the range of positive values. By comparing their values, it is possible to suppose that the best protective properties are found in the coatings of the initial (without heat treatment) chemical nickel and of the three-layer electrodeposited coating with a total thickness of ~20 μm.

The behavior of the anode polarization dependences (see Fig. 1) almost completely confirms the stated conclusion. In particular, it is obvious that, in conditions of accelerated electrochemical studies, the corrosion-electrochemical activity of the coatings increases in the series

$$Ni_{chem} \le Cu + Ni + Cr_{br} < Ni_{[chem, h/t]} < Cr_{milk} < Cr_{hard}.$$

The polarizability of the anode processes on the samples with coatings differs from the analogous parameter of the initial material—the SLS composite (curve *1*, Fig. 1). This testifies to the different electrochemical reactions taking place on the surface. Most probably, in terms of the potentials under consideration, they are attributed to active dissolving of metals of the substrate (curve *1*) or coatings, respectively, in the active or active–passive state.

Both metals constituting the base of the coatings under study tend to passivation, which depends on the structure, roughness, stress, and other characteristics of the electrodeposits [4]. In particular, it follows from our studies that, despite the more negative values of the corrosion potentials, the electrodeposited chromium coatings are easily passivated in sodium chloride brine. This tendency is expressed by the milky chromium (curve *6*) most of all; in hard chromium (curve *2*), it is expressed least of all. A region of passivity was not observed in the nickel deposits, including the initial and heat-treated ones.

The results of the corrosion tests (Fig. 2) allow more complete estimation of the protective properties of the coatings caused by their porosity or the presence of defects. In particular, we can mention that the initial composite SLS material intensively corrodes with the formation of rust characteristic of iron. The maximum damage is observed under drops of the corrosive solution; their perimeters are of irregular shape, reflecting the chemical inhomogeneity of the surface. The damage on the other areas is of local character.

After primary inspection, individual marks of corrosion were also found on three coatings—the heat-treated chemical nickel, the milky chromium, and the

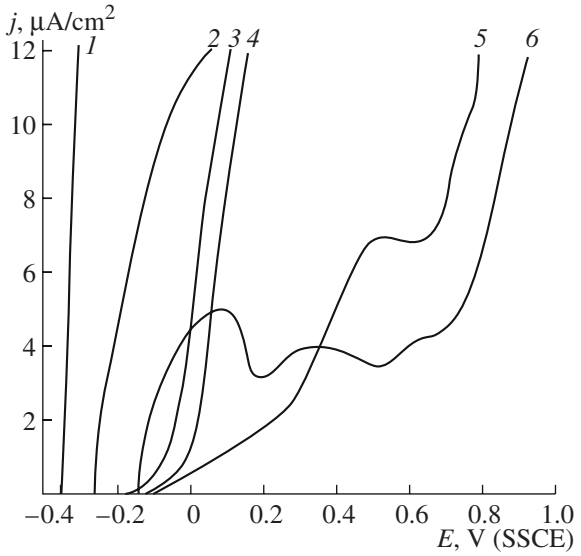

Fig. 1. Anode polarization curves of the metal SLS composite with different coatings in a 3% solution of NaCl: (*1*) without coating; (*2*) Cr_{hard}; (*3*) $Ni_{[chem, h/t]}$; (*4*) Ni_{chem}; (*5*) Cu+Ni+Cr_{br}; (*6*) Cr_{milk}.

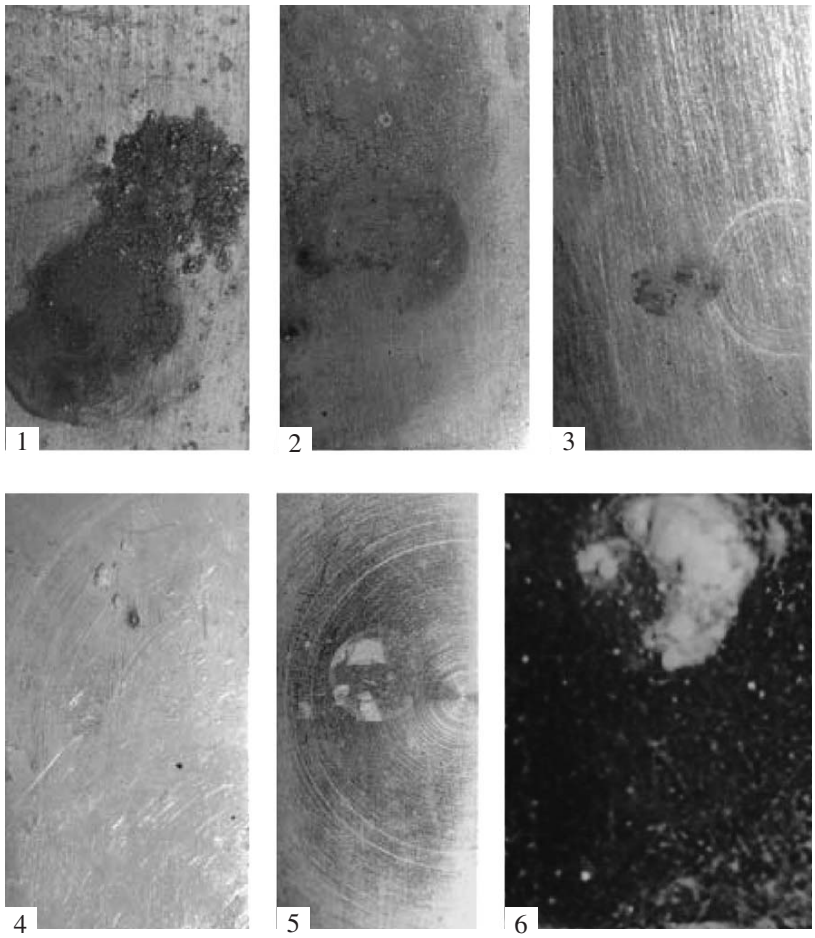

Fig. 2. Surface of SLS samples with coatings after corrosion tests in a 3% solution of NaCl: (1) initial composite; (2) $Ni_{[chem, h/t]}$; (3) Cr_{hard}; (4) Cr_{milk}; (5) Ni_{chem}; (6) Cu + Ni + Cr_{br}.

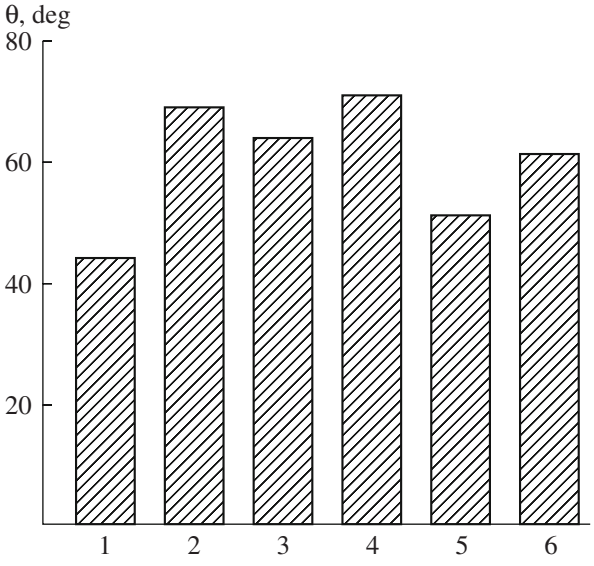

Fig. 3. Coating wettability with distilled water: (1) initial composite without coating; (2) Ni_{chem}; (3) $Ni_{[chem, h/t]}$; (4) Cr_{milk}; (5) Cr_{hard}; (6) Cu + Ni + Cr_{br}.

hard one (2, 3, 4). The products of iron corrosion on the chromium coatings were easily removed by rubbing.

"Absolute" protection in the test conditions was exhibited by the three-layer electrodeposited and initial coatings of chemical nickel. Neither marks of corrosion of the base nor products of oxidation of the coating materials were observed on them.

The results of the measurement of the wetting angles in distilled water (Fig. 3) correlate, first of all, with the corrosion-electrochemical behavior of the materials under study. Thus, the initial SLS composite characterized by the highest activity corresponds to the minimum value of θ and, accordingly, the maximum surface energy. For the coatings of chemical nickel and milky chromium, which were relatively "safe" in terms of corrosion, the maximum wetting angles were found; for hard chromium, the minimal wetting angles were found. The observed correlation allows using the value of θ as an additional criterion for the comparative evaluation of the corrosion activity of several materials.

CONCLUSIONS

The corrosion stability of metal composite products formed by SLS methods may be efficiently increased by means of electrodeposited or chemical coatings. At equal thickness (~20 μm), the best corrosion-protective properties are found in the coatings of chemical Ni, three-layer Cu–Ni–Cr_{br}, and milky Cr. The correlation established between the corrosion-electrochemical activity of the coating materials in a 3% solution of NaCl and the value of the wetting angle for surface and polar liquids allows applying it as an additional criterion for prediction of the severity of the corrosion of the materials under study.

REFERENCES

1. Mueller, T., Der Weg zum funktionstuchtigen Prototyp, *Kunststoffe*, 2005, no. 11, pp. 130–131.
2. Perevertailo, V.M., Shmekra, S.V., and Ostrovskaya, L.Yu., Estimation of the Surface Energy of Carbonaceous Materials on the Basis of Measurement of Wetting Angles, *Sverkhtverd. Mater.*, 2005, no. 3, pp. 19–30.
3. Sevidova, E.K. and Kononenko, V.I., Estimation of Ceramic Coatings of Bioengineering Application by the Wetting Method, *Sverkhtverd. Mater.*, 2007, no. 2, pp. 26–30.
4. Zhuk, N.P., *Kurs teorii korrozii i zashchity metallov* (Course of Theory of Corrosion and Protection of Metals), Moscow: Metallurgiya, 1976.

ISSN 1068-3755, Surface Engineering and Applied Electrochemistry, 2009, Vol. 45, No. 2, pp. 102–115. © Allerton Press, Inc., 2009.
Original Russian Text © M.S. Apfel'baum, 2009, published in Elektronnaya Obrabotka Materialov, 2009, No. 2, pp. 29–46.

ELECTRICAL PROCESSES IN ENGINEERING AND CHEMISTRY

On the Electric Field Distribution in Plane and Axisymmetrical Partially Charged Stationary Jets

M. S. Apfel'baum

Institute of Thermal Physics of Extreme States, Joint Institute for High Temperatures, Russian Academy of Sciences, ul. Izhorskaya 13, stroenie 2, Moscow, 125412 Russia

e-mail: msa@ihed.ras.ru

Received October 31, 2008

Abstract—This work is divided into two parts: a theoretical one including a literature review and a comparison of the calculations with experiments, whose installation diagrams are given. The methods of graphical and comparative analysis are applied for treatment of the data. A theoretical model of the charge formation in thin prebreakdown and plasma jets is described. A system of macroscopic equations of the thermal electrohydrodynamics of the phenomena under study is written. The calculations and their comparison with the experiments are carried out according to the obtained solutions of these equations.

DOI: 10.3103/S1068375509020057

The described theoretical modes and calculations of the spatial distributions of the electric field potentials measured in jets of partially charged fluids at both room and plasma temperatures are an enhancement of the models and calculations of papers [1, 2]. In this work, in contrast to [1], we discuss not only axisymmetrical but also plane laminar and turbulent jets, including the ones resulting from a prebreakdown applied electric field (see Fig. 1). We still consider that the thermal ionization (thermal dissociation) of the fluids under study occurs by the laws of the classical statistics and kinetics of Arrhenius–Boltzmann–Gibbs and that the rate of this ionization (dissociation) in unit time in the unit volume $W_{D,\,I}$ satisfies the known equation of statistical physics (mechanics)

$$\frac{\partial W_d}{W_d \partial T} = \frac{u_a}{k_B T^2}, \quad \frac{\partial W_{Ii}}{W_I \partial T} = \frac{u_i^A - u_e^B}{k_B T^2}. \qquad (1)$$

In (1), k_B is the Boltzmann constant, T is the absolute temperature, u_i^A is the potential of ionization of the atom A in a molecule of a fluid with covalent chemical bonds, and u_a is the activation energy for molecules of fluids with ionic bonds. In the case of dissociation, an analog to equation (1) is written in [3] (heptane is considered there as an example of a cleared fluid). In the presence of impurities, which, as a rule, increase the natural conductivity of a cleared fluid σ_0, for the calculation of $u_{a,\,i}$, it is necessary to take into account their characteristics influencing thermal ionization (thermal dissociation).[1] For application of this statistical kinetics with the covalent atom B affinity to the electron u_e, along with the use of a formulae close to equations (1), which is widely applied in statistical physics (mechanics), a sufficiently known hypothesis for linear dependence of the volume rate of ion formation $W_{D,\,I} = W_{D,\,I}(n_a, n_p)$ on the neutral molecule concentration n_a is postulated. In addition, its monotonously increasing dependence on module E (which is restricted by the breakdown voltage module being sufficiently high for the fluids under study), as well as on the relatively low volume concentration of the possibly available impurities n_p, is taken into account. By analogy with [3], let us introduce the proportionality coefficient K:

$$W_{D,I}\left(n_a, n_p, T, \left|\vec{E}\right|\right) = K_{D,I}\left(n_p, T, \left|\vec{E}\right|\right) n_a,$$

$$K_{D,I}\left(n_p, T, \left|\vec{E}\right|\right) = K_{D,I}(n_p, T, 0)\psi\left(\left|\vec{E}\right|, T\right)/\psi(0, T), \qquad (2)$$

$$\psi\left(\left|\vec{E}\right|, T\right) > 1, \quad T > T_0.$$

[1] In particular, according to the data of [4], the value of the low-voltage conductivity of cleared transformer oil, being determined by the empiric current–voltage characteristics, is lower by an order than the conductivity of the same untreated oil. For its enhancement, easily ionized additives (impurities) are often introduced into a fluid [5]. In the present work, we consider ionization of the molecules AB with covalent bonds of type $2AB \longrightarrow A^+B + AB^-$ and dissociation of molecules with ionic bonds of the type $AB \longrightarrow A^+ + B^-$. In the case of ionization, we consider fluids with molecules consisting of atoms A (of the air nitrogen type) with a considerably low ionization potential and of atoms B (of the air oxygen type) with sufficiently high electron affinity energy.

Herein, we consider that, for the fluids under study, along with the fulfillment of the inequality

$$n_{\pm} \ll n_a, \tag{3}$$

which mathematically closes the differential equations of the theoretical models of previous works (for example, [2]), the analogous algebraic inequality is also correct:

$$n_p \ll n_a. \tag{4}$$

Thereupon, $n_a = \dfrac{\rho_a}{m_a} \approx \dfrac{\rho}{m_a}$; that is, the density ρ of the mixture of charges and neutrals, including impurities, may be approximately considered to be equal to the density of the neutral component of the molecular carrier fluid ρ_a. Here, m_a is the mass of a neutral particle. It follows from integration (1) over T that

$$\begin{cases} W_d = C_d \exp\left(-\dfrac{u_a}{k_b T}\right); & \text{(5A)} \\ W_I = C_I \exp\left(\dfrac{u_e^B - u_i^A}{k_b T}\right). & \text{(5B)} \end{cases}$$

Equations (5) are known as Arrhenius-type equations. For the first time, kinetic equations of this type were obtained by Arrhenius empirically for the dependences of the constants of ionization (dissociation) on T (in the literature, the proportionality coefficients written in linear dependence (2) are called such). In works, dependences (2) are used for the theoretical simulation of the formation of a volume charge and the fields of this charge in the fluids under study in the cases of weak and strong electric fields applied near their boundaries. Herein, both heating up to plasma temperatures and partial combustion of resting and moving fluids are possible. In addition, in prebreakdown modes, we use these equations for calculation of their flow velocities caused by self-consistent electric fields. With the view to increase the module of the velocities of prebreakdown flows of weakly conducting liquid fluids (of transformer oil type) (Fig.1), impurities with a composition differing from those mentioned in [5] are often introduced. These impurities enhance the electrophysical or electrochemical ionization effects in electrodes, for example, in [6] (in both homogeneous and inhomogeneous strong applied electric fields); thereby, the flows of the fluids under discussion in these fields become more intense. In this work, we do not consider fluids with purposely introduced impurities. Instead, along with cleared fluids, the ones with a priori available impurities are studied. In the general (not necessarily Arrhenius) case, for the liquids and dense gases under investigation, the constant of ionization (dissociation) is considered to increase with the growth in temperature and the module of the intensity of the macroscopic electric field $\vec{E}$, which is taken into account in the mathematical formulation of equation (2). Strictly speaking, this field should be considered electromagnetic; yet, as has been shown, for example, in [7], in the weakly conducting (weakly ionized) fluids under study, the influence of the induced magnetic fields on the electrohydrodynamic phenomena is small, and applied magnetic fields from an external source are not discussed in this work. Herein, for the theoretical simulation and calculations of the macroscopic characteristics in the jets under consideration, it is sufficient to use electrohydrodynamics approximation [8], in which a system of Maxwell equations for a macroscopic magnetic field splits off from the principal system of equations, and it is possible not to consider it at all. The same is true of the equation for a change in the impurity concentration being low in comparison with the carrier fluid molecule concentration. In contrast to the magnetic field weakly influencing

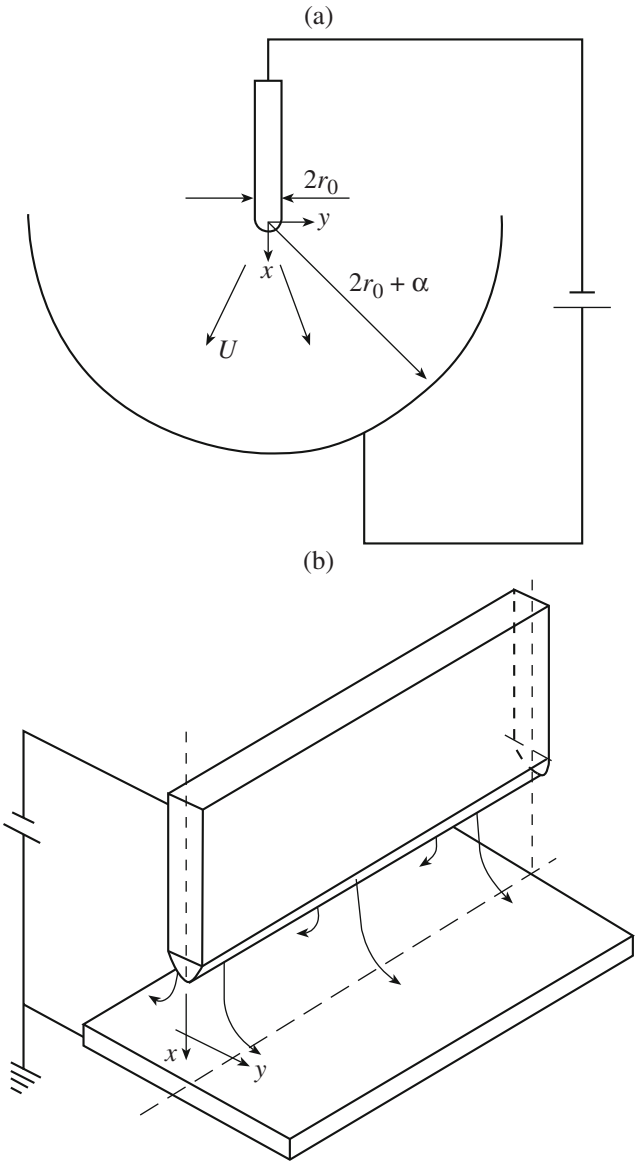

Fig. 1. Diagrams of the axisymmetrical (a) and plane (b) prebreakdown thin jets from high-voltage pin and bladelike electrodes.

the processes under study in polarizable nonmagnetizable fluids, impurities have an effect on the desired electrohydrodynamic characteristics. Hence, let us note that the possible types of equations for their volume concentration are close to the here-written equations for the same concentrations of charged components (the difference consists only with regard to charged components of the terms describing their drift in an electric field). The latter equations will be given below, as well as the possible types of equations for impurities. For the intensity of the desired electric field, the macroscopic Maxwell equations at constant relative dielectric permeability of the fluids under study ε_r are written in the standard form:

$$\begin{cases} \mathrm{div}(\vec{E}) = \dfrac{q}{\varepsilon_r \varepsilon_0}; \\ \vec{E} = -\nabla\varphi. \end{cases} \tag{6}$$

System of equations (6) is easily reduced to one Poisson's second-order scalar equation for the macroscopic electric field potential φ. The methods for the solution of boundary-value problems for such an equation with the right-hand side being implicitly dependent on the space coordinates are amply described in the literature. However, in the case of prebreakdown processes, the right-hand side of this equation depends on the electric field distribution; hence, along with the Poisson equation, the other equations written below must be solved as well. In equations (6), $q = (n_+ - n_-)Ze_0$ is the volume charge density, and ε_0 is the dielectric permeability of a vacuum in the SI system. In the absence of a strong applied electric field or before heating, the fluids under study (beyond the range of the diffusion layers near their boundaries) are electrically neutral. Their low-voltage conductivity σ_0 at the constant temperature T_0 is due to the availability in the fluid volume of the concentrations $n_{0+} = n_{0-} = n_0$ of charges of different signs being equal in value. A quasi-neutral background of positively and negatively charged particles may be formed in a fluid that mostly does not change its composition, according to (1), due to the volume thermal ionization (thermal dissociation) effects increasing in prebreakdown electric fields, as well as at heating or partial combustion of the fluids under discussion. According to, for example, [2, 7], this leads to the formation of a volume charge at an inhomogeneous distribution of the electric fields and temperatures in viscous, heat-conducting, and sufficiently dense fluids, in which the mobilities hardly depend on the electric field intensity module, in contrast to the case of low-density gases. In addition, according to, for example, [6], such a charge may also be formed near boundaries of fluids with high-voltage electrodes. The formation of this charge is also probable on other boundaries with solid, liquid, or gaseous media. In the case of the moving (including in a strong electric field) fluids under consideration, the hydrodynamic (gas-dynamic) transfer of the formed volume charge influences its spatial distribution. This influence in the volume of a moving fluid was studied earlier, for example, in [2], and it will be described below in this paper. The gas-dynamic transfer of this charge near the boundaries of the fluids under study in conditions of their possible electric breakdowns was described, for example, in [5]. The value of σ_0 is determined theoretically from the conditions of the ionization (dissociation) equilibrium due to ionization (dissociation) of molecules of a liquid (gas) with close-in-value recombination of charged particles. The rate of the volume ionization (dissociation) in this case is determined by (2); the recombination rate may be considered proportional to the ion concentrations $n_\pm$ with the proportionality coefficient K_r. This conductivity may be determined experimentally by the linear part of the current–voltage characteristics being observed for the fluids under discussion in weak fields only. It may also be found according to reference literature or calculated (in some cases) by methods of statistical physics and physical kinetics according to the charge composition of the fluid molecules.

The dependence of the coefficient or constant of recombination K_r on the ion mobilities $b_\pm$ of the charges may be determined by the simple Langevin–Onsager relation [9]:

$$K_r = \frac{(b_+ + b_-)Ze_0}{\varepsilon\varepsilon_0}. \tag{7A}$$

For the sake of simplicity, positive and negative free (in the case of dissociation according to Bjerrum [9]) ions are assumed to be charges of equal value or equal multiplicity (valence) Z. Therefore, hereinafter, e_0 is equal in value to the charge of a proton. As the multiplicity (valence) of the ion charge increases, for its calculation, e_0 must be multiplied by a respective value. In addition, formula (7A) is obtained under the condition of the proportionality of the rate of motion of the charges due to the electric field $\vec{v}_{\pm\vec{E}}$ and its intensity (macroscopic) $\vec{E}$ at which the ion mobility is the coefficient of this proportionality. In addition to these rates of charges, we must take into account their rate due to the molecular-ionic diffusion, which, according to Fick's law [9], is equal to $\vec{v}_{\pm\vec{E}} = \dfrac{D_\pm \nabla n_\pm}{n_\pm}$, and the rate of the hydrodynamic transfer $\vec{u}$. Under conditions (3) and (4), this rate may be considered close to the rate of the fluid. At plasma ideality, the coefficients of the ionic diffusion $D_\pm$ are related with their mobilities $b_\pm$ by the well-known Nernst–Townsend–Einstein correlation:

$$D_\pm = \frac{k_B T}{Ze_0} b_\pm. \tag{7B}$$

Thereupon, the rates of motion of the volume elements of the charged components are as follows:

$$\vec{u}_{\pm} = \vec{u} \pm b_{\pm}\vec{E} - \frac{k_B T b_{\pm}}{Ze_0}\frac{\nabla n_{\pm}}{n_{\pm}}. \quad (8)$$

Alongside with Fick approximation (8), other models may be used for determination of the macroscopic rates of the fluid components. Thus, for determination of $\vec{u}$ (the neutral component rate), with regard for the viscosity, under conditions (3) and (4), the Navier–Stokes equations are most often applied [10]:

$$\begin{cases} \rho\left(\dfrac{\partial \vec{u}}{\partial t} + \vec{u}\nabla\vec{u}\right) \\ = -\nabla p + \rho\nu\Delta\vec{u} + \rho\vec{g} + q\vec{E} + \dfrac{(\varepsilon_r - 1)\varepsilon_0\nabla(\vec{E}^2)}{2}; \\ \dfrac{\partial \rho}{\partial t} + \mathrm{div}(\rho\vec{u}) = 0. \end{cases} \quad (9)$$

Here, p and ν are the pressure and the kinematic viscosity of the neutral component of the fluid, respectively, being close to the corresponding characteristics of the fluid itself under conditions (3) and (4); t is the time; and $\vec{g}$ is the free-fall acceleration.

The expression for the volume density of the electric field forces in (9) in the case of constant ε_r is written according to [11]. For incompressible fluids, the second equation in (9) resulting from the mass conservation law is simplified, because, for these fluids, the constant density condition $\rho = \rho_0$ is fulfilled in the case of isothermal modes. In addition, due to the low (in terms of [4]) concentration of the possibly available untreated impurities n_p, the known diffusion equations applied, for example, in [12], for determination of the time–space distributions are not studied in this work. These differential equations with their respective initial and boundary conditions may be qualitatively studied or numerically solved after solution of the split-off-them electrohydrodynamic equations for the density, rate, pressure, and temperature of the carrier fluid; the charged component concentrations; and the electric field potential. It should be noted that, for a wide class of dispersion fluids, the distribution of the impurity concentration satisfies the well-known equation of convective diffusion. In some works, for example, in [12], for the determination of n_p, the equation of this diffusion is written in the Fick approximation. Since the particular solution of this equation is constant in the absence of a strong applied electric field or heating, here we will use this solution. Its physical sense is the alignment influencing the conductivity of impurities by diffusion. Herein, in the case of dissociation, there can be fluids with dissociation of both fluid molecules [3] and impurities (of the weak electrolyte type) [9]. The isothermal processes at room temperatures (at which in the fluids under study only impurity molecule dissociation occurs), being enhanced by the prebreakdown field, are theoretically described in the same manner as the dissociation of neutral molecules of cleared fluids. That is, in postulated dependences (2), the arguments of the volume concentrations of the fluid neutrals—the carrier and impurities—change places as in the formulae written below. The nonisothermal case of ion formation with T increasing from room to partially ionized plasma temperature is considered in this work only at the linear dependence of the rate of ionization (dissociation) of the neutral molecules of the carrier fluid on their concentration.

The continuity equations for the charged components with regard for (8) and Fick's diffusion law are written as follows [13]:

$$\frac{\partial n_{\pm}}{\partial t} + \mathrm{div}\left[n_{\pm}(\vec{u} \pm b_{\pm}\vec{E}) - \frac{k_B T b_{\pm}}{Ze_0}\nabla n_{\pm}\right] = K_{D,I}\left(n_p, T, \left|\vec{E}\right|\right)n_a - K_r n_+ n_-. \quad (10)$$

For the derivation of these equations, for example, in [13], the differentiation rules for the field of a vector being time-variant in the moving volume of a continuum are used (the substantiation for the correct application of the approximation of a continuum with a not very weak degree of ionization (dissociation) for its charged components is described, for example, in [8]). In isothermal conditions, as well as under the condition of a low impurity concentration (4) and constant density $\rho = \rho_0$, system of equations (10), together with equations (6) and (9), becomes mathematically closed. At the conditions $\vec{E} = 0$ and $T = T_0$, the value of $K_{D,I}$ may be determined by σ_0, where σ_0 is the conductivity at these conditions. That is, from the equation $W_{D,I} = W_r$ in the absence of heating and a strong applied electric field (beyond the range of the boundary layers near the frontier of the area under study, where diffusion may be significant), we get

$$C_I = \frac{\sigma_0^2 \exp\left[\dfrac{u_e - u_i(0)}{k_B T_0}\right]}{Z\varepsilon_r\varepsilon_0 e_0(b_+ + b_-)\rho_0},$$

$$C_D = \frac{\sigma_0^2 \exp\left[\dfrac{u_i(0)}{k_B T_0}\right]}{Z\varepsilon_r\varepsilon_0 e_0(b_+ + b_-)\rho_0}, \quad u_{a,i} = u_{a,i}\left(\left|\vec{E}\right|\right); \quad (11)$$

$$K_{D,I}(n_p, T_0, 0) = \frac{\sigma_0^2 n_a}{Z\varepsilon_r\varepsilon_0 e_0(b_+ + b_-)\rho_0}.$$

For obtaining of (11), Arrhenius equations (5) and Langevin–Onsager relation (7A) are used. In addition, in [9], Onsager substantiated the effect of a strong electric field's influence on the dissociation constant K_D for "loose" ion pairs and showed that this field does not

influence the coefficient of their recombination. The electric field's influence on the value of K_D may be written under the condition of the influence of $\vec{E}$ on u_i only (the Frenkel'–Plumley model [3, 14] for the case of ionic conductivity).[2] Herein, both in Onsager's model [9] and in the here-used model of Frenkel' for ionization [14] or of Plumley for dissociation [3], the classical statistics and kinetics of Arrhenius–Boltzmann–Gibbs are applied [15]. In the Onsager theory [9], the transition to macroscopic magnitudes is implemented after obtaining of a solution of a Boltzmann-type equation [8, 15] for the function of the distribution of an assembly of free charges formed under dissociation in the applied electric field rather than after the solution of relatively simple equation (1). For obtaining of a solution of differential equation (1), the electric field influence on the integration constant C is considered (as well as in [3, 4]) insignificant. Only its above-described influence on the ionization potential (activation energy) is taken into account. Then, the below-used exponential influence close to the Onsager one [9] is obtained in prebreakdown fields.

For closing of differential equations (9)–(11) in the case of the heating or partial combustion of the fluids under discussion, we should write the differential equation of heat penetration and the algebraic constitutive equation

$$\rho = \rho(p,T). \tag{12}$$

For an ideal and perfect gas, function (12) is written in the form [13]

$$p = \rho k_B T/m_a, \tag{13A}$$

and, for a liquid being incompressible in isothermal conditions (for example, transformer oil), in the form [12]

$$\rho = \rho_0[1 - \gamma(T - T_0)]. \tag{13B}$$

The heat penetration equation with regard for the Joule heating for the temperature T is written while ignoring the energy contribution due to the polarization, viscosity, and chemical reactions as follows:

$$\rho c_v\left(\frac{\partial T}{\partial t} + \vec{u}\nabla T\right) = \mathrm{div}(\lambda(T)\nabla T) + \sigma\vec{E}^2. \tag{14}$$

In equation (13B), the constant specific heat-expansion coefficient is considered to be sufficiently low (at prebreakdown electric fields, this equation may be used, for example, for the theoretical simulation of cooling of transformers, in the windings of which the temperature of the heat-transfer oil may achieve 373 K). The heat conductivity, for example, in the case of an ideal gas with constitutive equation (13A), linearly depends on the temperature in (14). In incompressible liquids and dense gases, for which it is appropriate to use constitutive equation (13B), the heat conductivity may be regarded as constant. There can also be fluids for which the heat conductivity dependence on the temperature is simulated by a nonlinear monomial and fluids for which this dependence is decreasing in a certain range of increasing T. The equations of thermogasdynamics, without regard for the thermal ionization (thermal dissociation) of the fluids under study and the volume charge formation, are usually written traditionally by all the authors, as well as the Maxwell equations for the macroscopic electric field. The equations of thermoelectrodynamics of type (10) are written differently in educational–scientific literature. Thus, instead of the equations with diffusion (10), for ion concentrations n, it is possible to write momentum conservation equations of type (9) in the form of Newton's law

$$\rho_\pm\vec{a}_\pm = -\nabla p_\pm + \vec{f}_\pm. \tag{15}$$

Here, $\rho_\pm$ is the densities, $\vec{a}_\pm$ is the kinematic accelerations of the physically infinitely small volumes of charged components of the mixture, and p and $\vec{f}_\pm$ are the pressures and the volume densities of the external forces influencing these volumes. Herein, in the analysis of the mathematical relations of the densities of the resultant external forces, according to the properties of the ions, the forces due to their viscosity may be regarded or disregarded. In Fick's approximation [15–18], the viscosity for the charged components, in contrast to the neutral components, at condition (3) is not regarded; however, their formation, for example, according to [2, 19], should be taken into account. Written macroscopic equations (15) may be obtained not only by the continuum mechanics methods described, for example, in [10, 13], but also by microscopic methods in determination of the respective moments from the Boltzmann kinetic equation for the microparticle distribution functions [8, 15]. In the derivation of the expressions for the force densities $\vec{f}_\pm$, it is possible to take into account the influence on these forces exerted by collisions between charged and neutral components, which is often used in the physics of nonideal partially ionized plasma [20]. Thus, in [21], the

[2] The decrease in the ionization potential ΔU_i by the electric field, according to [14], is determined by the simple formula $\Delta U_i = \int_{r_M}^{\infty} \frac{e_0^2 dr}{4\pi\varepsilon\varepsilon_0 r^2}$. Here, r_M is the potential barrier maximum at the Coulomb attraction of the nuclei and electrons in the field. Herein, $\frac{e_0^2}{4\pi\varepsilon\varepsilon_0 r_M^2} = e_0|\vec{E}|$ (analogously, the work function according to [18] and the energy of breaking of the ionic bond of a molecule u_a with the particle charge $|e| = Ze_0$ decrease according to [3]). In addition, according to [3, 14, 18], these decreases double due to the electric field work. It is additionally assumed that a strong electric field does not influence the electron affinity of the molecule and, according to [9], the recombination coefficient.

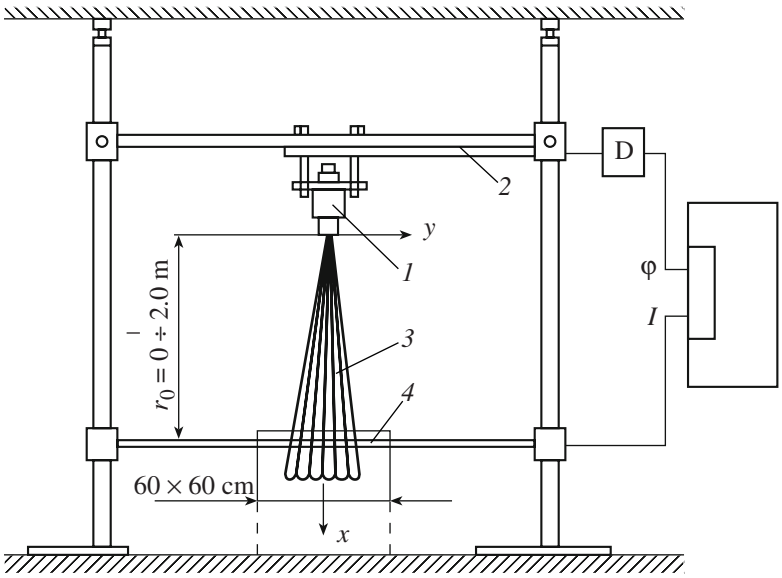

Fig. 2. Diagram of the experiments of [21] on determination of the spatial distribution of the electric potential along the plasma axisymmetrical thin jet: *1* is the thermal diffuser, *2* is the fixing arm, *3* is the jet, and *4* is the plane collector electrode.

macroscopic momentum equations for the charged components are written as equations of the type

$$\begin{cases} \rho_{\pm}\vec{a}_{\pm} = -\nabla p_{\pm} + n_{\pm}Ze_0\vec{E} + \alpha_{\pm}n_{\pm}(\vec{u} - \vec{u}_{\pm}); \\ p_{\pm} = n_{\pm}k_B T. \end{cases} \quad (16)$$

Here, $\alpha_{\pm}$ are the constants obtained by the characteristics of the collisions of the charged ions with the neutral molecules. In addition, the constitutive equations for the ion components in (16) are written in approximation (13A) of an ideal ion gas. In the transition to a nonideal ion–ion gas (one of the types of nonideal plasma), these equations with regard for collisions of charged particles not only with neutrals but also with each other may become, according to, for example, [20], more complex. More often, instead of (16), the equations for the momenta or their fluxes are used either in Fick's approximation or by Euler (ignoring the viscosity) together with the respective mass continuity equations described above. Equations (16) for the ion components are partially close to both models. Thus, (16) contains all the terms that are in the momentum equation with external forces (except for the viscous friction forces). Exactly this approximation is referred to as the Euler equations for a nonviscous gas. In contrast to the equations of Euler or (with regard for viscosity) Navier–Stokes, equations (16) contain a term in which the collisions of neutral and charged components are taken into account with a quantitative effect proportional to the relative rates. For the solution of the problems of the characteristics of gas-dynamic jets heated to plasma temperature, in [21], the authors assume local thermodynamic equilibrium in them, at which the temperatures of all the mixture components may be considered equal. The same is true of the temperature of a mixture of neutral and charged components with partial dissociation of the molecules or their partial ionization with subsequent adhesion to other molecules of free electrons.

At local thermodynamic equilibrium of the acceleration $\vec{a}_{\pm} = 0$ and from (16), Fick's diffusion equations are obtained (8). In [21], these equations, being mathematically closed in the general case, were solved without regard for diffusion and in the case

$$|\vec{u}_{\pm}| \ll |\vec{u}|. \quad (17)$$

In problems of the distribution of the potential of the electric field formed in heated strong laminar and turbulent gas–dynamic jets (Fig. 2), condition (17) is justified. Herein, the closures of equations (16) are Maxwell equations (5) only. On the assumption of quasi-neutrality, being more characteristic of plasma fluids with $T > 1000$ K [20, 21], equations (16) may probably be solved without application of Maxwell equations (5). This method was used for the solution of these equations in [21]. In the general case, equations (5) and (16) are insufficient for obtaining mathematically closed equations of thermal ionization (thermal dissociation) even at known distributions of u and T; therefore, they should be added to equations of the type of continuity equations (10).

In obtaining of solutions in [21], the contribution of charge drift in the electric field was taken into account. In [22], only the contribution due to the hydrodynamic transfer of the formed volume charge in a heated (thin, of the type of [10, 12, 23]) jet was taken into account, yet with no condition of plasma quasi-neutrality. The generalization and specification of the results of report [22] concerning only the generation of the electric field

distribution in plasma jets will be described below. The theoretical model of [21] can hardly be applied for the calculation of the characteristics of rates of thermal ionization (thermal dissociation) and conductivity in strong electric fields. At the same time, the theoretical model described here can be applied for calculation of these electrokinetic and electrodynamic characteristics. For this purpose, as in previous works, we will use an abridged (simplified) system of equations (5)–(10) without regard for diffusion and hydrodynamic charge transfer. The self-consistent potential φ is determined by both the applied and uncompensated charges in the volume. With regard for the difference in the electric mobilities $b_{\pm}$, the applied system differs from the analogous one written, for example, in [16], by an additional summand[3]

$$\begin{cases} q = -\varepsilon_r\varepsilon_0\vec{E}\nabla\sigma/\sigma \quad (-\vec{E}\nabla\sigma/\sigma = \operatorname{div}(\vec{E})); \\ \varepsilon_r\varepsilon b_+ b_-\vec{E}\nabla q = \sigma_0^2\dfrac{\Psi(|\vec{E}|,T)}{\Psi(0,T_0)} - \sigma^2 + (b_+ - b_-)q\sigma; \\ \vec{E} = -\nabla\varphi. \end{cases} \tag{18}$$

For obtaining of (18), in addition to Langevin correlation (7A), equation (11) was used. For the generalization of the electrodynamic system of equations (18) in the case of nonisothermal heating, it is sufficient to use, along with (7A), two more Langevin relations [18] independent of the temperature of the products of the neutral fluid density according to the mobility of both the positive and negative ions. Without regard for the collisional ionization by free electrons in a strong electric field, which is more typical of low-density gases, an explicit form of the function of additional ionization (dissociation) $\Psi(|\vec{E}|, T)$ may be written by Frenkel' [14] or, analogously, only in the case of dissociation by [3], as well as by Onsager [9].

The conditions of the neglect of the diffusion and convective components of the current densities are derived in [2]; they are a part of the conditions of the closeness of the rates of the ionization (dissociation) and recombination. Herein, system of electrodynamic macroscopic equations (18), together with Maxwell equations (5), splits off from the Navier–Stokes hydrodynamic equations [10, 13] and may be solved independently. With the view to obtain the condition of chemical or ionization (dissociation) equilibrium (out of the borders of the diffusion boundary layer and in the hydrostatic approximation), we transit to the dimensionless components in (18):

$$E_* = U/L, \quad \sigma_* = \sigma_0, \quad b_* = (b_+ + b_-)/2,$$
$$n_* = \sigma_*/(2b_*Ze_0);$$

$$\tilde{\varphi} = \varphi/L, \quad \tilde{T} = T/T_*, \quad \tilde{\sigma} = \sigma/\sigma_*,$$
$$\tilde{b}_{\pm} = b_{\pm}/b_*, \quad \tilde{q} = q/(n_*Ze_0).$$

At this nondimensionalization, L is the characteristic dimension of the change in variables, U is the applied electric voltage, σ_* is the self-neutralizing background conductivity of the type of conductivity of quasi-neutral plasma [20] or an electrolyte [17] due to the dissociation (ionization) of the liquid (dense gas), and T_* is the representative temperature. Then, system of equations (5) and (18) has the following form:

$$\begin{cases} \tilde{q} = -\delta\tilde{\vec{E}}\tilde{\nabla}\tilde{\sigma}/\tilde{\sigma}, \quad \delta = \dfrac{2\varepsilon_r\varepsilon_0 b_* E_*}{\sigma_* L} \\ \dfrac{\delta^2}{4}\tilde{b}_+\tilde{b}_-\tilde{\vec{E}}\tilde{\nabla}\tilde{q} = \dfrac{\tilde{\Psi}\left(|\tilde{\vec{E}}|,\tilde{T}\right)}{\Psi(0,T_0)} - \tilde{\sigma}^2 + (\tilde{b}_+ - \tilde{b}_-)\tilde{q}\tilde{\sigma}; \\ \tilde{\vec{E}} = -\tilde{\nabla}\tilde{\varphi}. \end{cases} \tag{19}$$

In (19), differentiation with respect to the dimensionless coordinate takes place (with the characteristic size L), $\tilde{\Psi}\left(|\tilde{\vec{E}}|,\tilde{T}\right) = \Psi(E_*, |\tilde{\vec{E}}|, T_*, \tilde{T})$.

In the zero-order approximation over $\delta(\delta \ll 1)$, the conductivity is a known function of the electric field intensity, which is not Laplacian in this approximation. The volume charge being formed in the first approximation over δ influences the cumulative value $\vec{E}$. Its density q in this approximation is determined from equations obtained from (19). In dimensional variables,

$$\begin{cases} q = -\varepsilon_r\varepsilon_0\vec{E}\nabla\sigma/\sigma; \\ \sigma = \sigma_0\dfrac{\Psi^{1/2}(|\vec{E}|,T)}{\Psi^{1/2}(0,T_0)}; \\ \vec{E} = -\nabla\varphi. \end{cases} \tag{20}$$

Similar to as in [16], it is possible to obtain additional conditions of dissociation (ionization) equilibrium in the case of moving fluids. For a pin high-voltage electrode, as an analog of the dot one, due to its small dimensions, it is sufficient to search for a solution of (20) depending on one space coordinate r only while ignoring the changes in latitude and longitude. The difference of the $b_{\pm}$ values in this problem (in contrast to the problems of [21]) contributes to the terms of the

[3] In the statement of problems [22] of the potential of jets heated to plasma T, the mobilities may be unequal. We will show below that their difference does not influence the values of the desired characteristics in conditions of quasi-neutrality. In the case of electron–ion plasma [20], this difference is responsible for the electron character of its conductivity.

quadratic order of infinitesimals with respect to the small parameter δ. In cases when T = const and the conductivity in weak fields σ_0 is due to impurities only, the nondimensional similarity criterion for the phenomena under study δ increases with increasing E_* value; in strong fields it becomes sufficiently great. At the condition $\delta \gg 1$, when the volume charge formation beyond the range of the boundary layers is due to both $\nabla\sigma$ and the cathode emission (injection), solutions of (19) may be found in the form

$$\sigma = -b_- q. \tag{21}$$

The inequality $\delta \gg 1$ can be fulfilled at an increase in the fluid mobility. In particular, the mobility increases at the phase transition from a liquid to a low-density gas, at which both the general model (regard for electron formation becomes appropriate here) and the form of Ψ become more complicated due to, for example, the appearing collisional ionization of molecules by the free electrons accelerated by strong electric fields. This is also true in the absence of an increase in σ with an increasing field intensity module. The solutions of type (21) may be applied for reasons of the neglect of diffusion only beyond the range of the neighborhood of the high-voltage electrode of the boundary layer type. In the theory of corona discharge of low-density gases, this unipolar charged zone is referred to as the external zone of discharge [7]. At positively charged electrodes (being optically corona sometimes), the class of solutions should be used for this zone instead of (21):

$$\sigma = b_+ q. \tag{22}$$

For this class, the inequality $\delta \gg 1$ is also fulfilled; herein, the deviations from the equilibrium ionization (dissociation) are great. Then, the current on the boundary in the case of both (21) and (22) is due to carriers of one sign only.

In the case of empiric boundary conditions, the solutions of a system of unipolar one-dimensional equations for E are written, for example, in [24]. For the thermionic boundary conditions with respect to the current density

$$j_- = j(r_0') = b_- qE \tag{23}$$

on the pin high-voltage electrode and $j_+ = j(d) = 0$ on the anode, the one-dimensional solution of such a system with regard for the respective solution [24] has the following form:

$$E^2(r) = \frac{C}{r^4} + \frac{I}{6\pi\varepsilon_r\varepsilon_0 b_- r}. \tag{24}$$

Here, I is the intensity of the current flowing through the "electrodes–weakly conducting fluid" system, which, in this work, as well as the high voltage applied to the electrodes, is considered only as time constants (flows caused by the electric field from an alternating-voltage supply are described, for example, in [6]). The integration constant C for equations of the unipolar conductivity in (24) is determined by the work function $e_0\chi$ in the case of a heated cathode and electron affinity with regard for the electric field influence on this work function [18]:

$$I = 4\pi r^2 j, \quad \tilde{I} = \frac{I}{4\pi r_0'^2 A_T T_w^2}, \quad \chi = \frac{e_0}{8\pi\varepsilon_r\varepsilon_0 r_a};$$

$$C = r_0'^4 \left\{ \frac{16(k_B T)^4 (\pi\varepsilon_r\varepsilon_0)^2}{e_0^6} \right. \tag{25}$$

$$\left. - \left(\frac{e_0\chi}{k_B T} - \frac{u_e}{k_B T_W} + \ln\tilde{I} \right) \frac{\tilde{I}}{6\pi\varepsilon_r\varepsilon_0 b_-} \right\}.$$

For the determination of C, it is appropriate to use this boundary condition of the thermionic emission domination (with respect to other ionization or injection surface processes) with subsequent electron attachment to molecules for the cathode being heated at least to plasma temperatures. The jets described in [18] are also observed from such a pin cathode close to the dot one (Fig. 1a). Herein, the solutions of (24)–(25) may be applied for studying the processes in the neighborhood of a flame placed into a strong electric field [18], yet with preservation of the fluid composition in this neighborhood (only for the partial combustion of the fluids under discussion caused by this flame). The solution of (24) with the integration constant C, which was determined from the empiric boundary conditions at room temperatures, was written, along with [24], in a great number of publications where only fluids with unipolar conductivity were considered as well as electrodynamic problems without the prebreakdown hydrodynamics of neutrals.

In the instant case of C determination by (25), A_T is the Richardson constant of the thermionic emission obtained by Dashman by quantum-mechanical methods, T_W is the cathode temperature before the field application, and r is the characteristic radius of the electrode with a near-electrode diffusion boundary layer. In this work, we assume that the electric current flowing through the circuits whose arrangements are shown in Fig. 1 weakly changes the temperature of the heated high-voltage cathode or anode. If the interelectrode distance is great, we can obtain an expression for the applied voltage according to (24):

$$U \approx \sqrt{\frac{2Id}{3\pi\varepsilon_r\varepsilon_0 b_-}}. \tag{26}$$

The argumentation in favor of the appropriateness of the application of this formula for a cold cathode is described in some previous works and in the literature on corona discharge of low-density gases. In the case of the cathode heated to plasma temperatures, the sufficient condition for the use of formula (26) is deduced in

[1] in the form of the simple inequality $C/r_0^3 \ll 1$, where C is determined by (25). This inequality is obtained from (24), (25), and the second mean value theorem for a certain Riemann integral. The quadratic dependence of the current on the voltage according to (26) is numerically confirmed by the results of many experiments where a corona was observed near the high-voltage apex, which not always occurs in the liquids and dense gases under consideration. The quadratic current–voltage characteristic is also obtained under the treatment of prebreakdown experiments with weakly conducting dielectric liquids [6]. It may be confirmed theoretically in conditions of equilibrium volume isothermal dissociation (ionization) in the case $\Psi(|\vec{E}|, T_0)/\Psi(0, T_0) = \Psi_0(|\vec{E}|)$ determined by Frenkel' [14] or by [3] with the multiple (Z) elementary charge

$$\beta(T) = \frac{(Ze_0)^{3/2}}{(\pi\varepsilon_r\varepsilon_0)^{1/2}k_BT};$$
$$\beta(T_0) = \beta_0; \quad (27)$$
$$\Psi_0(|\vec{E}|) = \exp\left(\beta_0|\vec{E}|^{\frac{1}{2}}\right).$$

In this case, for the field near a high-voltage spherical or semispherical electrode of small (in comparison with the interelectrode distance) radius (Fig. 1), in previous works, for example, in [16], the analytical solution of equations (20) was obtained:

$$E_0 = |\vec{E}(r_0)|;$$
$$|\vec{E}|\exp\left(\beta_0|\vec{E}|^{\frac{1}{2}}\right) = \frac{I}{4\pi\sigma_0 r^2};$$
$$\varphi_w = \varphi(r_0'); \quad (28)$$
$$|\varphi_w| = U = \left|\int_{r_0}^{\infty} E dr\right| = \frac{1}{2}\left(\frac{I}{\pi\sigma_0}\right)^{1/2}$$
$$\times\left(\frac{8}{\beta_0}\left[1 - \exp\left(-\frac{\beta_0E_0^{1/2}}{4}\right)\right] - E_0^{\frac{1}{2}}\exp\left(-\frac{\beta_0E_0^{1/2}}{4}\right)\right).$$

One can see from (28) that the difference of the self-consistent electric field intensity module from the applied field value is small only under the condition

$$\beta_0E_0^{1/2} \ll 1, \quad (29)$$

that is, for undeveloped-by-[6] flows from high-voltage electrodes. As I or U increases, the current–voltage characteristic (28) becomes nonlinear. At the value

$$\beta_0E_0^{1/2} \gg 1 \quad (30)$$

from (28), by respective passage to the limit, we obtain

$$U = \frac{4}{\beta_0}\left(\frac{I}{\pi\sigma_0}\right)^{1/2}. \quad (31)$$

Herein, the influence of r_0 on the current–voltage characteristics is small, as well as in the modes of unipolar strongly nonequilibrium ionization (dissociation), for which this follows from (28).

The preservation of the quadratic current–voltage characteristic in conditions of the influence of the hydrodynamic charge transfer at the electric wind of weakly conducting liquid fluids on its spatial distribution is experimentally shown in [6] not only for unipolar-charged liquids. According to [6], the same empiric dependence on U is more typical of velocities of developed flows. For undeveloped flows, according to [6], the empiric exponent in dependences of the axial jet velocity (Fig. 1a) on the voltage is higher. Below, this will be shown theoretically.

For such flows $u(x, 0) \sim u^n$, $n = 3$ according to [6]. Theoretically, a decrease in this exponent at an increase in U and at transition from undeveloped flows of electric wind to developed ones may be obtained in conditions of equilibrium ionization (dissociation), for which the current voltage characteristic is determined by formulae of types (28) and (31). In [16] and in other previous papers, in these conditions, there was used the analogy of an electric wind and a hydrodynamic immersed jet, that is, a jet outflowing from a nozzle into a space filled with the same fluid that does not flow around walls or other solid bodies, such as cylinders, ellipsoids, and cones, after outflowing. The use of this analogy was proposed for the first time by Ostroumov [7]; however, in the cases when the jet is an additional source of mass, the analogy with [6] is invalid. It may be applied for the flow structure (e.g., for Landau thin jets [10]) with the weak influence of the additional mass introduced by the jet being small in comparison with the fluid mass; however, on the other hand, an electric wind jet that is not a mass source may be compared to thin jets caused by a point momentum source [10] only when the Coulomb force density sharply decreases with the distance from the active high-voltage electrode being close to the dot one. Thereupon, the calculation of the vector constant of the jet momentum P according to [10], in the calculation of whose velocities the mass source characteristics are assumed to be close to zero, is reduced to calculation of the integral

$$P = \int_V q\vec{E}dV = \vec{F}_e, \quad (32A)$$

where V is the half-space volume in the direction from a pin or semispherical high-voltage electrode (Fig. 1a). The mathematical proof of equation (32A) for a class of generalized functions was given in previous works of the author of this paper, although the statement itself was expressed in publications of other authors as well,

for example, in [12]. In the spherical coordinates $dV = r^2\sin(\theta)drd\theta d\zeta$, this integral converges in the case when

$$\left|q\vec{E}\right| < \frac{F}{r^{3+n}}, \tag{32B}$$

where $n > 0$; F is the constant majorant; and r is the distance to the center of the active electrode, which, due to its small dimensions, is close in topology to the point (spherical, small in size) or radial coordinate. Equilibrium solutions of (28) satisfy condition (32), and strongly nonequilibrium solutions of (23) do not. Therefore, in [25], where unipolar-charged jets in a strong inhomogeneous electric field were considered (Fig. 1), the structure of the obtained axisymmetric solutions appeared to be more complex than in [1, 2], where the Landau–Schlichting solutions were applied [11, 12] and the momentum P was calculated according to solutions of (28) with the use of (5).

Let us note that one can set problems of the microlevel calculation of the charge formation kinetics, being more rigorous than the Arrhenius one, with subsequent application of the results in electrohydrodynamics. At the same time, many works are concerned with the argumentation of Arrhenius equations (5) (see, e.g., [26]). Hence, formulae for the velocities of plane jets, such as those presented in Fig. 1b, were also deduced in this work with the use of (5). They will be given in the final part of our paper. Concerning the analogy with hydrodynamic jets, we should note that it is widely used in magnetic hydrodynamics, for example, in [12]; however, a (32)-type criterion of the pointness of the Ampere force causing magnetohydrodynamic jets has not been obtained. In the limiting case (32A) for velocities of undeveloped jets, according to [2], we find $u \sim U^{5/2}$, which is in agreement with the results of Gibbins' experiments [19]. In the other limiting case (32B) and $d \gg r = \sqrt{x^2 + y^2} \gg r_0$ for prebreakdown flows of viscous liquids for a Schlichting jet (Fig. 1a), [12] the following formulae are obtained:

$$P = 2\pi\rho_0\int_0^\infty u_x^2 y dy = \frac{\varepsilon_r\varepsilon_0 U^2}{8}; \tag{33A}$$

$$u_x = \frac{3P}{8\pi\rho_0 x(1+\xi^2/4)^2},\quad u_y = \frac{\sqrt{3P}(\xi - \xi^3/4)}{2\sqrt{\pi\nu\rho_0}x(1+\xi^2/4)^2},$$
$$\xi = \frac{\sqrt{3P}}{2\sqrt{2\pi\rho_0\nu x}}. \tag{33B}$$

Herein, the frequently observed [4, 6] quadratic dependence on U or the linear one on I theoretically results from (32A) for the axial velocity of developed jets. In addition, formulae (33A) confirm the observed-in-[6] weak influence of the value of the radius of the curvature of a thin high-voltage electrode (Fig. 1a) on the velocities of the prebreakdown flows of the fluids under study from this electrode. The observed insignificant influence of Z on the value of these velocities, confirmed by formulae (33), counts in favor of the possibility to apply these formulae for calculation of velocities without additional determination of this initial constant by a computational or experimental method according to the composition of the molecules of the fluid (its dielectric permeability is assumed to be an initial reference constant, as well as the mobility and low-voltage conductivity). The molecular (atomic) composition of the fluid is not taken into account in writing of macroscopic equations for the calculation of the electrodynamic characteristics in external zones of unipolar and bipolar corona either [24, 27]. However, ignoring this composition, one can set only empiric boundary conditions in corona electrodes.

Lets us note that, for Schlichting jets, structure (33B) survives for the turbulent conditions too with the kinematic viscosity being replaced with the apparent turbulent viscosity. Then, the determined-by-(33A) momentum P of the gas-dynamic (plasma) jets, such as the jets of reaction–propulsion units (Fig. 2), according to (32A), is equal to their propulsion, which is easily confirmed by the below-given experimental data of [21] near the nozzle slot. Herein, for heated fluids, constitutive equations (13B) may often be used, in particular, for the case of infinitely thin (weakly spraying) jets of these fluids (in this case, the specific coefficient of the volume expansion of the jet itself may be assumed to be small). The estimates made by means of solutions of (33) for these jets in the experiment conditions of [21] show that, in momentum equation (9), the gravitational force density is negligible in comparison with the inertial term in this equation. For these estimates, we took the reference value of the heated air viscosity (0.015 St) applied in the experiments of [21] and contained only in the calculation formulae below for the distribution of the desired potential along plane jets. The formulae for the determination of the steady-state distribution of the absolute temperature T at constant heat conductivity in these jets with regard for (33B) are obtained from (14) in [23]. For the axial distribution of the electric potential from (6) with the conditions along the axis of these jets being close to [17] and under fulfillment of the relations

$$\left|\sigma\vec{E}\right| \ll \left|q\vec{u}\right|,\quad q = q(x),\quad \vec{j} = q\vec{u},$$
$$I = \int_S q\vec{u}d\vec{S} = 2\pi q\int_0^\infty u_x y dy \tag{33C}$$

we obtain the Poisson one-dimensional equation, having applied the charge conservation law in the integral form

$$\int_S \vec{u} d\vec{S} = J = 0.404\sqrt{\frac{P}{\rho_0}}x;$$

$$qJ = I = S_c A_T \exp\left(\frac{U_e - e_0\chi}{k_B T_c}\right); \quad (34)$$

$$S_c = \pi(R_c + r_c)l_c, \quad \Delta\varphi = -\frac{I}{0.404\varepsilon_r\varepsilon_0\sqrt{\frac{P}{\rho_0}}x}.$$

For this equation, the boundary conditions may be written in the standard form

$$\varphi(S_c) = \varphi(0) = 0, \quad \varphi(d_m) = \varphi_0;$$
$$-h_c \le x \le d_m, \quad h_c = \sqrt{l_c^2 - (R_c - r_c)^2}. \quad (35)$$

In (35), the range of the definition of the axial coordinate is given (here r, R, l, and h are the radii, generatrix, and height of the nozzle's truncated cone). The circle radius of the nozzle slot (critical section) for thin jets is considered small as compared to the dimensions of the fluid into which this jet outflows. In addition, in (35), d is the maximum empiric distance between the nozzle diffuser and the net-shaped collector electrode (Fig. 2) in the experiments of [21]. The problem of replacement of the empiric boundary condition at the distance d from the nozzle with a more rigorous one (from theoretical considerations) has not been solved yet. At the same time, in this work, in contrast to some previous publications, the total electric current was determined not empirically but according to modification (34) of the known Richardson–Dashman formula for the density of the emission current from a metal nozzle. In addition, in this theoretical simulation, it follows from the condition of the adhesion of the viscous fluids under study to the lateral nozzle surface that the thermionic current near this metal surface is equal to the convective electric current in the main part of the jet. Herein, as against formula (25), the influence of the electric field near nozzles of plasma jets on the electronic work function of their surfaces can be neglected due to the formation of low fields in the experiments of [21]. The applied modification of the Richardson–Dashman thermionic formula allows obtaining overall formulae for calculations of the spatial distribution of the desired potential taking into account that it is affected by the electron affinity energy of the molecules of a moving heated fluid. At I nonaltering by the charge conservation law defined by (33), the solution of (34) with boundary conditions (35) in the one-dimensional approximation is as follows:

$$\varphi(x) = \frac{\varphi_0 x}{d_m} - \frac{Ix\ln(x/d_m)}{0.404\sqrt{\frac{P}{\rho_0}}\varepsilon_r\varepsilon_0}, \quad (36)$$

herein, the consumption J in (34) is written according to the Schlichting formula in the case of a high-pressure (turbulent) jet; its derivation is presented, for example, in [28].

Contrary to the earlier solutions of macroscopic equations (16) obtained in [21], distribution (36) allows calculating the maximum in the spatial potential distribution, which was observed in the experiments of [21]. Herein, according to (36), the extreme value is obtained with the distance from the source being approximately the same as in the experiments of [21]:

$$\frac{d_m}{\exp\left(1 - \frac{1}{\tilde{I}}\right)}, \text{ where } \tilde{I} = \frac{Id_m}{0.404\varphi_0\varepsilon_r\varepsilon_0\sqrt{\frac{P}{\rho_0}}}. \quad (37)$$

Let us note that, in the experiments of [21], the mass introduced by the jet weakly influenced the mass of the jet involved in motion by it due to the small nozzle volume in comparison with the volume of the fluid under discussion (Fig. 2). Therefore, the theoretical solutions of the equations of viscous fluid motion [10, 12] obtained analytically as is shown, for example, in [28], in the thin jet approximation are applied in this work for description of electric convective jets both at room temperatures and heated to plasma temperatures. The diagram of spatial distribution (36) is shown in Fig. 3 in the form of theoretical curve *1* calculated for the experiment conditions of [21] with a net-shaped electrode. The temperature of the jet of partial combustion products near the nozzle was 2370 K and the velocity of its outflowing was 1380 m/s, which testifies to the justification of the use of the formulae for a turbulent jet in calculations of the desired potential. The critical radius of the nozzle's truncated cone was 2.2 mm, the generatrix of this cone was 75 mm, and the nozzle height was 50 mm. The jet propulsion was 230 N. The potential distribution over the jet axis was determined from the critical section of the nozzle to a distance of 2 m from it. Since the dielectric permeability of air at room temperature is 1.1, that is, close to 1, it was assumed to be such in the heated air jet as well. The density of the partially combusted air was assumed to be 1.3 in the SI system. The electronic work function of the metal nozzle's surface according to reference literature was selected to be 4.36 eV; the electron affinity of air oxygen was 1.8 eV. Let us note that a simple comparative analysis of the values of the work functions, ionization potentials, and electron affinity energies is described, in particular, in [20] (In the case of dissociation, analogs of the thermal emission current and the work function of the electrode surface are, for example, given in [17] for the exchange current and the electrochemical potential near the electrode surface.). However, for fluids weakly dissociating at room temperatures, the analysis of the exchange currents and electrochemical potentials was performed more completely than in [17] and other monographs on electrochemistry for the case of strong electrolytes. For jets at plasma T, in this work, as well

as in previous publications, only experiments with grids were theoretically analyzed (Figs. 2, 3). The application of the described theoretical results is quite practicable in both installations used in industry, such as electric filters or electric dehydrators of oil, and in aircraft engineering (reaction–propulsion units) and in the design engineering of new electrohydrodynamic devices, such as electrohydrodynamic pumps [29] and generators [30]. In devices applied in industry, the calculations of the volume charges, electric fields, and current–voltage characteristics by the techniques proposed here (such as the synthesis of techniques [31] and [24]) can lead to the refinement of the values of the consumed electric power and energy and to their application for the diagnostics of electric breakdown avoidance. One of the examples of such diagnostics by means of solution of gas-dynamic explosion problems [33] will be described below. Herein, the data for the initial values (for example, of the mobility and the dielectric permeability) may be adapted from [32].

In the design engineering of electrohydrodynamic pumps and generators introduced in industry, one can calculate the discharge heads, discharge rates, and powers generated by them with the use of the here-proposed analytical formulae for the determination of the electric fields, pressures, and flow velocities due to fields of thin high-voltage electrodes. A description of one of the constructions of an electrohydrodynamic pump with such an application and technique for calculation of its discharge head and discharge rate is given, for example, in work [29], where it is shown that it is efficient to apply high-voltage bladelike electrodes instead of pin ones, as in [30]. Analogously, the practicability of the use of plane plasma jets as electrohydrodynamic generators for comparison of the maxima of the calculated potentials in such and similar axisymmetrical jets was announced in [1, 22]. In the present work, we will show this using the example of a planar nozzle and conditions of experiments that may be carried out with a plane jet by analogy with those carried out for an axisymmetrical nozzle and described in [21].

In the case of a plane jet, we will consider a net-shaped collector electrode only. On it, the boundary condition is set the same as in the axisymmetrical case, at a distance of 2 m from the nozzle. The jet velocity near the nozzle is also assumed to be 1380 m/s. The jet propulsion is set the same. The dimensions of the planar nozzle are as follows: the area of each square plate is taken to be 100 cm^2, and the distance between them is 2.2 mm, as the small radius of the conical nozzle (truncated cone) in the experiments of [21]. The planar nozzle length is selected to be 0.1 m, which is much greater than the distance between the plates. The other initial data for the calculations by the below formulae in the plane case are taken to be the same as in the above described axisymmetrical case. In addition to these data, according to [28, 34], in the plane case, it is necessary to specify the momentum and current per unit length of the narrow nozzle slot (P/L and I/L). Formulae

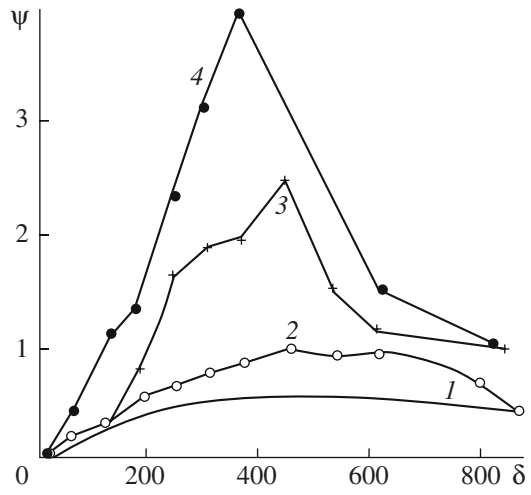

Fig. 3. Distribution of the electric field potential in the jet along the axis ($\Psi = \varphi/\varphi_{max}$, $\delta = x/r_e$): *1* is the theoretical solution; *2* is the experiment with a net-shaped electrode; *3* is the experiment with a metal electrode; *4* is the experiment with a liquid electrode (water).

for the velocities of such a plane laminar jet obtained by Schlichting [28, 34], analogous to (33), look as follows (at their application, the planar nozzle length L must significantly exceed the slot width):

$$u_x = 0.454\left(\frac{P}{\rho_0 L}\right)^{2/3}(\nu x)^{-1/3}(1-\tanh^2\xi);$$

$$u_y = 0.5503\left(\frac{P\nu}{x^2 L}\right)^{1/3}[2\xi(1-\tanh^2\xi)-\tanh\xi];$$

$$\xi = 0.2572\left(\frac{P}{\rho_0\nu^2 L}\right)^{1/3}\frac{y}{x^{2/3}}; \qquad (37A)$$

$$\frac{J}{\rho_0 L} = \int_{-\infty}^{\infty} u_x^2 dy = 0.3019\sqrt[3]{\frac{P\nu x}{(\rho_0 L)^4}}.$$

Herein, in contrast to the axisymmetrical jet (Fig. 2) in (37), x and y are Cartesian coordinates instead of cylindrical ones. The procedure of obtaining a plane-jet solution of the Poisson one-dimensional equation for the electric potential along the jet axis, analogous to (34) with boundary conditions of type (35), also consists in its double integration. The solution in the dimensionless form, analogous to (36), looks as follows:

$$\bar{\varphi}(\bar{x}) = \bar{x}[0.9\bar{I}(1-\bar{x}^{2/3})+1];$$

$$\bar{\varphi} = \varphi/\varphi_0; \qquad (38)$$

$$\bar{I} = \frac{Id^{5/3}}{\varepsilon_r\varepsilon_0\varphi_0 L^{2/3}}\left(\frac{\rho_0}{\nu P}\right)^{1/3}.$$

This is also a nonmonotonic function with one extremum. The distance at which the maximal with-respect-to-the-nozzle value of φ is achieved is the same as in the

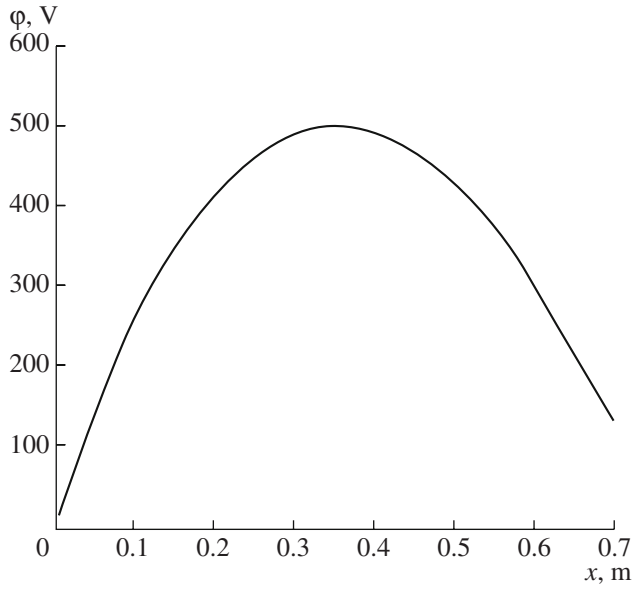

Fig. 4. Diagram of the theoretical solution (38) for the stationary distribution of the electric field potential along the plane plasma jet.

case of the axisymmetrical jet. If, for the empiric boundary (by [21]) condition, we assume $\varphi_0 = 50$ V at a distance of 2 m from the nozzle, then, for the maximum potential, we have $\varphi_m = 500$ V, which is much higher than in the axisymmetrical case with the same boundary condition. The diagram of the size distribution of φ determined by (38) is shown in Fig. 4. The diagram is plotted using reference and experimental (from [21]) initial data. The constancy of the kinematic viscosity of a fluid, postulated in calculations in the temperature range from room to plasma ones, follows from the Walden relations [32] of the constancy of the products of the respective dynamic viscosity and charge mobilities and from similar relations of Langevin [18] for the fluid density and mobilities mentioned above.

Contrary to plane plasma jets, for prebreakdown jets from a thin bladelike electrode (Fig. 1b), formulae (37) can be applied only in the case of small deviations from the quasi-neutrality of the fluid. Let us show this analogously to the above described axisymmetrical case. The plane jet momentum is

$$P/L = \int_S f_q ds, \tag{39}$$

where S (Fig. 1b) is the sectional plane normal to the jet. In the case of plane prebreakdown jets, improper integral (39) converges on the assumption

$$\begin{gathered} \left|q\vec{E}\right| < \frac{F}{Lr^{2+\chi}}; \\ r = \sqrt{x^2 + y^2}; \\ \chi > 0. \end{gathered} \tag{40}$$

As well as in the axisymmetrical case, condition (40) is satisfied by a quasi-neutral solution for q. Thereupon, for E in the one-dimensional approximation, we have

$$E\exp(\beta_0 E^{1/2}) = \frac{I}{2\pi\sigma_0 rL} \tag{41}$$

at the positive sign of the thin high-voltage electrode (Fig. 1b). In the case of (41), from (30) and (38) for the prebreakdown plane jet momentum, we obtain

$$P = \frac{2\varepsilon_r\varepsilon_0 I}{\pi\sigma_0\beta_0^2}. \tag{42}$$

Substitution of (42) into (37) leads, as well as in the axisymmetrical case, to the increasing dependences of the components of the velocities of the jets from thin high-voltage electrodes on the measured current. Herein, an additional limitation of the proposed theory of prebreakdown jets, for example, in the axisymmetrical case, is the smallness of the maximal radius ($d \gg r_{\max}$) of the zone of microbreakdowns observed in neighborhoods of thin high-voltage electrodes in comparison with the interelectrode distance (Fig. 1a). Thereupon, the estimate for U is obtained:

$$U \ll \frac{d}{Ze}\sqrt[3]{\frac{100\pi k_B^2 p_0 T_0^2}{21}}. \tag{43}$$

In formula (43), p_0 is the pressure of the fluid under study at room temperatures. It is this pressure that is contained in the more general formula of Sedov [33] resulting in condition (43). This formula is obtained in [33] from the solution of the problem of point explosion for fluids with constitutive equation (13B). For the application of these solutions for the viscous and heat-conducting fluids under discussion, one more condition must be satisfied:

$$\varepsilon_r\varepsilon_0/\sigma_0 \ll \max(d^2/\nu, d^2/a). \tag{44}$$

In (44), the thermal diffusivity

$$a = \lambda_0/c_V\rho_0.$$

Herein, the heat conductivity is assumed to be independent of T. Let us note that, in [35], the electric breakdown energy is taken equal to QU, where

$$Q = \int_V q dV. \tag{45}$$

In (45), V is the space volume. In the present paper, this energy is calculated as an integral of the volume density of the electrostatic energy, which leads to the correction factor in (43).

ACKNOWLEDGMENTS

The author thanks the participants in the Electrohydrodynamic [16] and 26th Magnetohydrodynamic [22] conferences for useful discussion of the results.

REFERENCES

1. Apfel'baum, M.S., Distribution of Electric Fields in Certain Types of Stationary Weakly Ionizing Jets, *Elektron. Obrab. Mater.*, 2007, no. 1, pp. 31–46 [*Surf. Eng. Appl. Electrochem.* (Engl. Transl.), vol. 43 no. 1, p. 24].
2. Yantovskii, E.I. and Apfel'baum, M.S., On Pumping Action of a Thin High-Voltage Electrode in Weakly Conducting Dielectric Liquid, *Zh. Tekh. Fiz.*, 1980, vol. 50, issue 7, pp. 1511–1520.
3. Plumley, H.J., Conduction of Electricity by Dielectric Liquids at High Field Strength, *Phys. Rev.*, 1941, vol. 50, no. 2, pp. 200–207.
4. Petrichenko, N.A., Thermal Phenomena Accompanying Electric Wind in Liquids, *Elektron. Obrab. Mater.*, 1973, no. 6, pp. 44–45.
5. Lyubimov, G.A., On Condition of the Breakdown of a Near-Electrode Layer in a Flow of Ionized Gas, *Zh. Prikl. Mat. Tekh. Fiz.*, 1973, no. 3 pp. 16–23.
6. Stishkov, Yu.K. and Ostapenko, A.A., *Elektrogidrodinamicheskie techeniya v zhidkikh dielektrikakh* (Electrohydrodynamic Flows in Liquid Dielectrics), Leningrad: LGU, 1989.
7. Bologa, M.K., Grosu, F.P., and Kozhuhar', I.A., *Elektrokonvektsiya i teploobmen* (Electroconvection and Heat Exchange), Kishinev: Shtiintsa, 1977.
8. Gogosov, V.V., Polyanskii, V.A., Semenova, I.P., and Yakubenko, A.A., Equations of Electrohydrodynamics and Transfer Coefficients in a Strong Electric Field, *Izv. Akad. Nauk SSSR, Ser.: Mekh. Zhidkosti i Gaza*, 1969, no. 2, pp. 31–45.
9. Onsager, L., Deviation from Ohm's Law in Weak Electrolytes, *J. Chem. Phys.*, 1934, vol. 2, no. 9, pp. 599–615.
10. Landau, L.D. and Lifshits, E.M., *Mekanika sploshnykh sred* (Mechanics of Continua) Moscow: GITTL, 1954.
11. Landau, L.D. and Lifshits, E.M., *Elektrodinamika sploshnykh sred* (Electrodynamics of Continua), Moscow: GITTL, 1957.
12. Boyarevich, V.V., Freiberg, Ya.Zh., Shilova, E.I., and Shcherbinin, E.E., *Elektrovikhrevye techeniya* (Electric Vortex Flows), Riga: Zinatne, 1985.
13. Sedov, L.I., *Mekhanika sploshnoi sredy* (Mechanics of Continuum), Moscow: Nauka, 1994, vol. 1.
14. Frenkel', Ya.I., To the Theory of Electric Breakdown in Dielectrics and Electronic Semiconductors, *Zh. Eksp. Teor. Fiz.*, 1938, issue 12, pp. 1293–1301.
15. Levich, V.G., Vdovin, Yu.A., and Myamlin, V.A., *Kurs teoreticheskoi fiziki* (Course of Theoretical Physics), Moscow: Nauka, 1971, vol. 2.
16. Apfelbaum, M.S., The Prebreakdown Electrohydrodynamic Equations for Liquid Insulators, *Proc. 7th Int. Conf. on Modern Problems of Electrophysics and Electrohydrodynamics of Liquids*, St. Petersburg, 2003, pp. 9–13.
17. Damaskin, B.B., and Petrii, O.A., *Vvedenie v elektrokhimicheskuyu kinetiku* (Introduction into Electrochemical Kinetics), Moscow: Vysshaya Shkola, 1975.
18. Lawton, J. and Weinberg, F., *Electrical Aspects of Combustion*, Oxford: Clarendon Press, 1969; Moscow: Energiya, 1976.
19. Gibbings, J.C. and Mackey, A.M., Charge Convection in Electrically Stressed Low-Conductivity Liquids, Part 3: Sharp Electrodes, *J. Electrostatics*, 1981, vol. 11, pp. 119–134.
20. Khrapak, A.G., Fortov, V.E., and Yakubov, I.T., *Fizika neideal'noi plazmy* (Physics of Nonideal Plasma), Moscow: Fizmatlit, 2004.
21. Usachev, V.K., Stavrov, Yu.P., and Tambovtsev, V.I., Electrokinetic Phenomenon in a Jet of Ionized Combustion Products, *Tezisy dokladov nauchno–prakticheskogo seminara po elektrofizike goreniya* (Proc. Sci. Workshop on Electrophysics of Combustion), Karaganda, 1985, pp. 66–67.
22. Apfelbaum, M.S., The Space Electric Field Distribution in Thermoionization Strong Jets, *Proc. 15th Int. Conf. on MHD Energy Conversion and 6th Workshop on Magneto-Plasma Aerodynamics*, Moscow, 2005, vol. 1, pp. 196–197.
23. Loistyanskii, L.G., *Laminarnyi pogranichnyi sloi* (Laminar Boundary Layer), Moscow: Gos. Izd. Fiz.–Mat. Lit., 1962.
24. Tikhodeev, N.N., Differential Equation of Unipolar Corona and Its Integration in Simplest Cases, *Zh. Tekh. Fiz.*, 1955, vol. XXV, issue 8, pp. 1449–1457.
25. Zhakin, A.I., On Electroconvective Jets in Liquid Dielectrics, *Izv. Akad. Nauk SSSR, Ser.: Mekh. Zhidkosti i Gaza*, 1984, no. 6, pp. 13–19.
26. W. Stiller, *Arrhenius Equation and Nonequilibrium Kinetics*,, Leipzig: Teubner–Verlag, 1989; Moscow: Mir, 2000.
27. Tikhodeev, N.N., Interrelation of Current–Voltage Characteristics of Corona Discharge at Constant Voltage for Various Systems with Wires, *Izv. Ross. Akad. Nauk, Ser.: Energetika*, 2002, no. 2, pp. 85–95.
28. Loistyanskii, L.G., *Mekhanika zhidosti i gaza* (Mechanics of Liquid and Gas), Moscow: Nauka, 1978.
29. Apfel'baum, M.S., On One Technique of Calculation of the Characteristics of Electrohydrodynamic Flows and Pumps, *Elektron. Obrab. Mater.*, 1990, no. 6, pp. 39–42.
30. Bortnikov, Yu.S. and Rubashov, I.B., Electric Gas–Dynamic Effects and Their Application, *Magn. Gidrodinamika*, 1975, no. 1, pp. 23–34.
31. Ostroumov, G.A., *Vzaimodeistvie elektricheskikh i gidrodinamicheskikh polei* (Interaction of Electric and Hydrodynamic Fields), Moscow: Nauka, 1979.
32. Adamchevskii, I., *Elektricheskaya provodimost' zhidkikh dielektrikov* (Electric Conductivity of Liquid Dielectrics), Leningrad: Energiya, 1972.
33. Sedov, L.I., *Metody podobiya i razmernosti v mekhanike* (Methods of Similarity and Dimensionality in Mechanics), Moscow: Nauka, 1977.
34. Schlichting, H., *Boundary Layer Theory*, New York: McGraw–Hill, 1964; Moscow: Nauka, 1974.
35. Apfel'baum, M.S., The Problem of Point Electric Explosion of Weakly Conducting Fluids, *Elektron. Obrab. Mater.*, 2000, no. 6, pp. 31–42.

ISSN 1068-3755, Surface Engineering and Applied Electrochemistry, 2009, Vol. 45, No. 2, pp. 116–124. © Allerton Press, Inc., 2009.
Original Russian Text © A.G. Anisovich, I.N. Rumyantseva, V.F. Bevza, E.I. Marukovich, V.V. Azharonok, S.V. Goncharik, 2009, published in Elektronnaya Obrabotka Materialov, 2009, No. 2, pp. 47–56.

ELECTRICAL PROCESSES IN ENGINEERING AND CHEMISTRY

Structural Changes in СЧ-25 Cast Iron in an Amplitude-Modulated High-Frequency Electromagnetic Field

A. G. Anisovich[a], I. N. Rumyantseva[a], V. F. Bevza[b], E. I. Marukovich[b], V. V. Azharonok[c], and S. V. Goncharik[c]

[a]*State Scientific Institution, Physical–Technical Institute, National Academy of Sciences of Belarus, ul. Kuprevicha 10, Minsk, 220141 Republic of Belarus*

e-mail: anna-anisovich@yandex.ru

[b]*State Scientific Institution, Institute of Metal Technology, National Academy of Sciences of Belarus, ul. Byalynitskogo–Biruli 11, Mogilev, 212030 Republic of Belarus*

[c]*State Scientific Institution, Stepanov Institute of Physics, National Academy of Sciences of Belarus, pr. Nezavisimosti 68, Minsk, 220072 Republic of Belarus*

Received November 6, 2008

Abstract—The high-frequency magnetic field influence on changes in the structure and properties of СЧ-25 cast iron obtained by the method of continuous-cycle freeze casting has been studied. It has been found that the structure effects of high-frequency magnetic-pulse action on cast iron are the "healing" of surface defects, perlite dispersion, a decrease in the ferrite content in the structure due to the ferrite–graphite complex transformation into perlite, coarsening and modification of the internal structure of graphite inclusions, and a change in the cementite morphology. The observed structural changes determine the decrease in hardness of automobile parts of the cylinder–piston block.

DOI: 10.3103/S1068375509020069

INTRODUCTION

One of the methods for obtaining cast iron castings is continuous-cycle freeze casting (CCFC) [1]. It is based on the principle of directional crystallization of cast iron, wherein the external surface of a casting is formed by the working cavity of a crystallizer and the inner surface is obtained directly from the melt and is determined by the crystallization front only. By virtue of this method, it is possible to form gray iron castings for fabrication of parts of cylinder–piston blocks of internal-combustion engines, compressors, and hydromechanical transmission boxes of car-and-tractor units. The high performance reliability and service life of the given units and machines are due to the considerably steep requirements concerning the structure and properties of the formed castings: a perlite matrix (ferrite content less than 5%), fine flake graphite (25–95 μm), hardness of ~100 HRB, tensile strength ≥25 kg/mm^2, and high wear resistance. The CCFC method allows high physicomechanical and operation properties of the castings; high efficiency, economic feasibility, and environmental safety of the process; relatively simple and rapid transfer from one standard size of castings to another; and the possibility to control the mode of their secondary cooling. However, this method is characterized by some disadvantages such as the availability of the chilling effect on the external surface and of the inverse chill in the near-surface layer inside the casting, the availability of a high content of ferrite and spotted interdendritic graphite (graphite of supercooling), and nonuniformity in the distribution of the dispersion of the phase components and the metal matrix over the cross section of a casting. The application of traditional methods of thermal aftertreatment of castings for elimination of these disadvantages requires additional energy consumption leading to rise in the production cost. In addition, the problem of obtaining a uniform structure by the heat treatment methods is, as a rule, inadequately solved [2].

Promising methods for changing in structure and properties of metals and alloys are involve exposure to pulse nonthermal energies [3]; among them, a special position is held by magnetic-pulse treatment (MPT) [4–5]. Magnetic fields are widely used for modification of structure and properties of various materials such as water–electrolyte solutions [6], crystallized melts, biological objects [7–8], polymer materials, and fibers [9–11]. The simple technology and high efficiency of the applied devices and installations allows recommending this method of treatment for various domains of economic activity, yet the most significant results were obtained in the mechanical engineering industry. In particular, the use of MPT made it possible to improve the characteristics of iron–carbon alloys [12] and nonferrous metal alloys [13], to decrease the residual and fatigue stresses in pieces and constructions, and

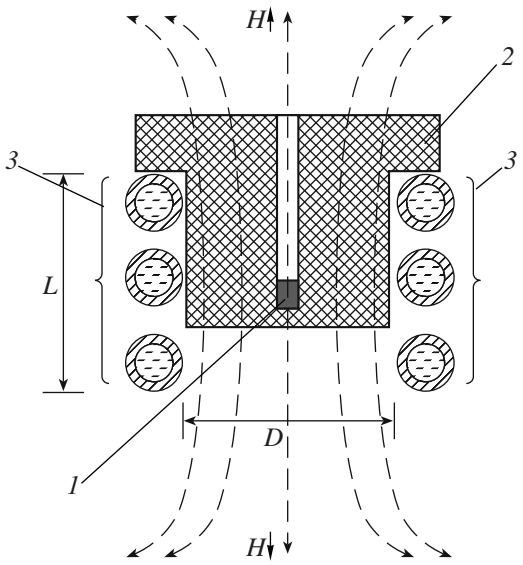

Fig. 1. Circuit diagram of the treatment of cast iron samples in a high-frequency magnetic field: *1* is the sample, *2* is the dielectric matrix for the sample position fixation, and *3* is the water-cooled inductor.

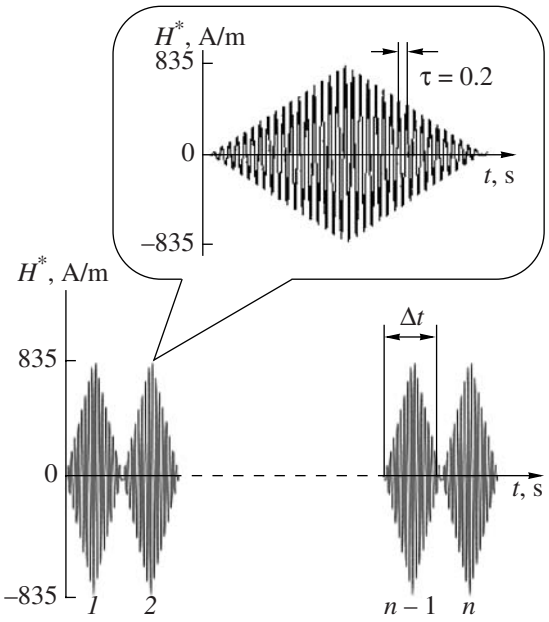

Fig. 2. Time cyclogram of a metal sample treatment by the magnetic component of a high-frequency electromagnetic field.

to improve cutting tool life [14]. It should be noted that, despite the considerably wide practical introduction of MPT, it is still of keep interest to researchers and representatives of industry. The study of the influence of magnetic fields on metals and alloys is in progress and it is considered to be one of the promising directions in general metallurgy and solid state physics. However, almost in all the works, strong (with an intensity of $H \sim$ kA/m) [15] and superstrong ($H \sim$ MA/m) [16] magnetic fields are applied; it is not a simple engineering problem to obtain them [17]. The effect on metals and alloys exerted by easily established weak magnetic fields with an intensity H of the order of several hundreds of A/m is poorly known, although the results obtained by some authors show that this treatment is promising. Thus, for example, in work [18], the influence of treatment in a magnetic field of low intensity on the properties of steel 4Х5МФК is studied. Changes in the structure and properties of beryllium bronze Cu-2%Be under the action of a magnetic field with an intensity of $H \sim$ 900 A/m are investigated in [19]. Specific features of the influence of a low-intensity magnetic field on the structure of condensed media are considered by the author of [20].

The obtained results allow us to suppose that low-intensity MPT can be efficient for structural rearrangement in gray cast iron.

In this work, we study the possibilities to change the structure of СЧ-25 cast iron by the action of an amplitude-modulated high-frequency magnetic field of low intensity on samples formed by CCFC.

EXPERIMENTAL

Low-intensity high-frequency magnetic-pulse treatment (WFMPT) of cast iron was carried out by means of an experimental installation constructed on the basis of a ВЧИ-62-5-ИГ-101 alternating current generator. The installation allowed establishing an electromagnetic field with the power-line frequency $f = 5.28$ MHz localized in a water-cooled three-turn inductor with length $L = 90$ mm and the inner diameter $D = 80$ mm, which is connected, as an inductance load, to the output of the ВЧИ-62-5-ИГ-101 generator (Fig. 1). Samples *1* were placed into dielectric matrix *2* and were introduced into the axial zone of inductor *3* at a distance of 40 mm from its upper face.

The root-mean-square values of the intensities of the magnetic H and electric E components of the electromagnetic field on the inductor axis were determined by a П3-15 high-frequency field-intensity meter with a Я6П-110 indicator; they amounted to 590 A/m ($V \approx 1$ mT, to a precision of ~6%) and 12700 V/m (to a precision of ~4%), respectively. The amplitude values $H^* = \sqrt{2}H$ and $E^* = \sqrt{2}E$ were 835 A/m ($V \approx 1.5$ mT) and 17960 V/m. The error of the generator operation mode reproduction did not exceed 0.5%; therefore, the overall error of determination of the intensities of the electromagnetic field influencing the sample was 10% at most. The treatment was exercised in the air at atmospheric pressure according to the cyclogram depicted in Fig. 2. Each sample was subjected to the action of a high-frequency sinusoidal magnetic field modulated in amplitude within the range from 0 to 835 A/m. The modulation period was $\Delta t \sim 3$ s; it formed an ordinary cycle of the

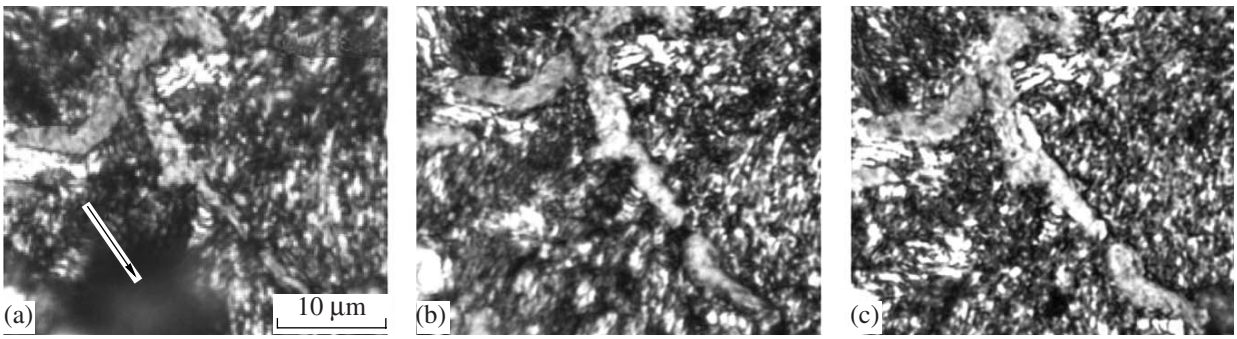

Fig. 3. Change in the structure of cast iron at WFMPT: initial state (a); after two (b) and four (c) cycles of treatment.

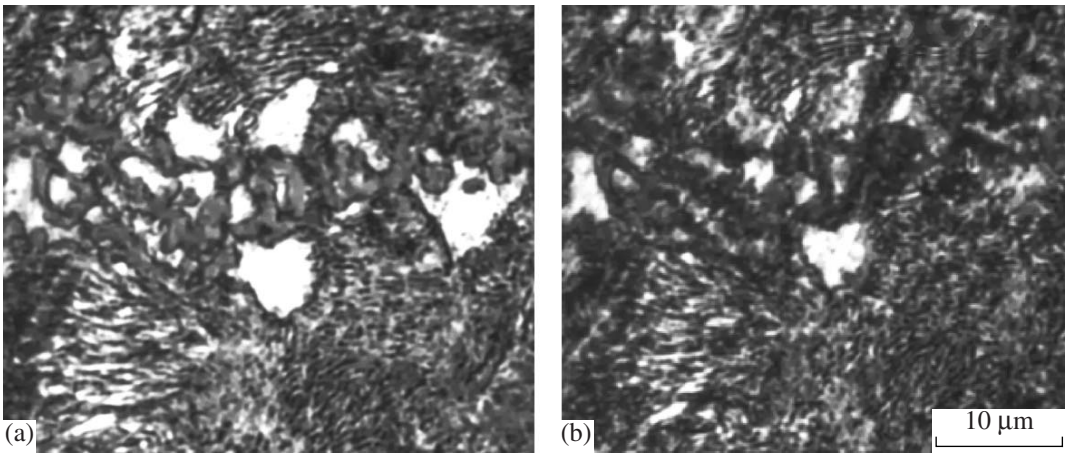

Fig. 4. Change in the ferrite component at WFMPT after two (a) and four (b) cycles of treatment.

treatment. The number of ordinary cycles n varied from 1 to 8. Herein, the heating of the sample did not exceed 40–60°C; thereby, the possibility of a thermal change in its structure was eliminated.

The structural changes in the cast iron after WFMPT were studied by the method of sighting metallography with the use of an МИКРО-200 metallographic complex. The controlled part of the metallographic section was marked with a scratch on its surface. The chemical etching of the surface for the examination of its microstructure was executed by means of a 3% solution of nitric acid in ethyl alcohol. The X-ray structural analysis of the samples under study was performed by virtue of a DRON-3M diffractometer in CuK_α radiation.

RESULTS AND DISCUSSION

In the initial state, the cast iron structure is characterized by perlite eutectics and graphite (Fig. 3a). In some parts of the metallographic section, separate inclusions of free ferrite and cementite are found (Figs. 4, 5), as well as spotted graphite. The WFMPT of cast iron leads to a change in the morphology of the graphite inclusions (for the most part, to an increase in their thickness). The perlite component also undergoes changes shown in the dispersion of the perlite and improvement of its homogeneity at an increase in the number of treatment cycles. One of the specific features of WFMPT is the possibility to eliminate mechanical damage of the surface (Fig. 3). The part of the metallographic section containing a mark (scratch) is marked with an arrow in Fig. 3a (the initial state). Figures 3b and 3c present the mark images, from which we can observe gradual transformation of the cast iron structure in the damaged area depending on the number of cycles of WFMPT. One can see that, after two treatment cycles (Fig. 3b), the image definition of the mark still differs from that of the neighboring parts of the metallographic section; however, after four cycles, all the parts of the metallographic section are in one plane and their image definition is nearly the same; that is, healing of the mechanical defect of the surface has accured.

The applied treatment contributes to a decrease in the ferrite content in the structure of the cast iron (Fig. 4). As the number of treatment cycles increases, the ferrite–graphite complex (Fig. 4a) transforms into perlite (Fig. 4b); therein, the dispersion of the perlite matrix increases. The changes in the eutectics are seen in more detail in Figs. 6 and 7, which present the structural changes in a large fragment of an eutectoid and eutectic grain. As a result of the WFMPT, thinning of the plates

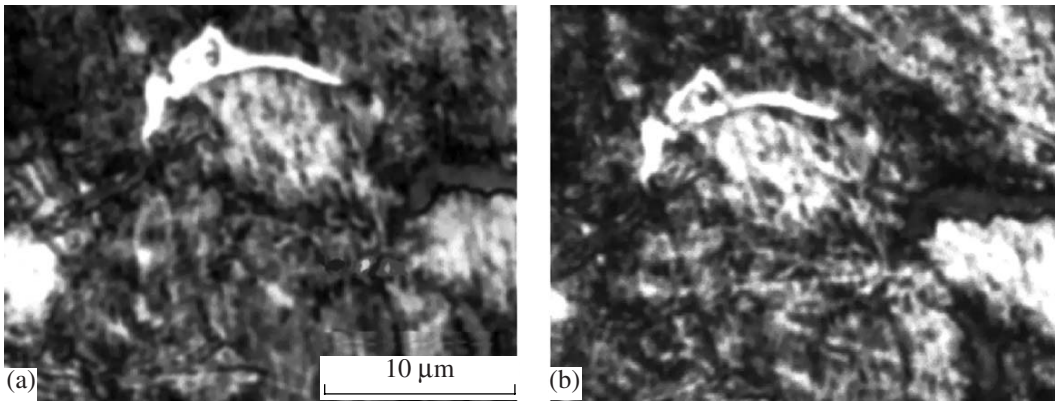

Fig. 5. Change in the cementite inclusion morphology at WFMPT after two (a) and four (b) cycles of treatment.

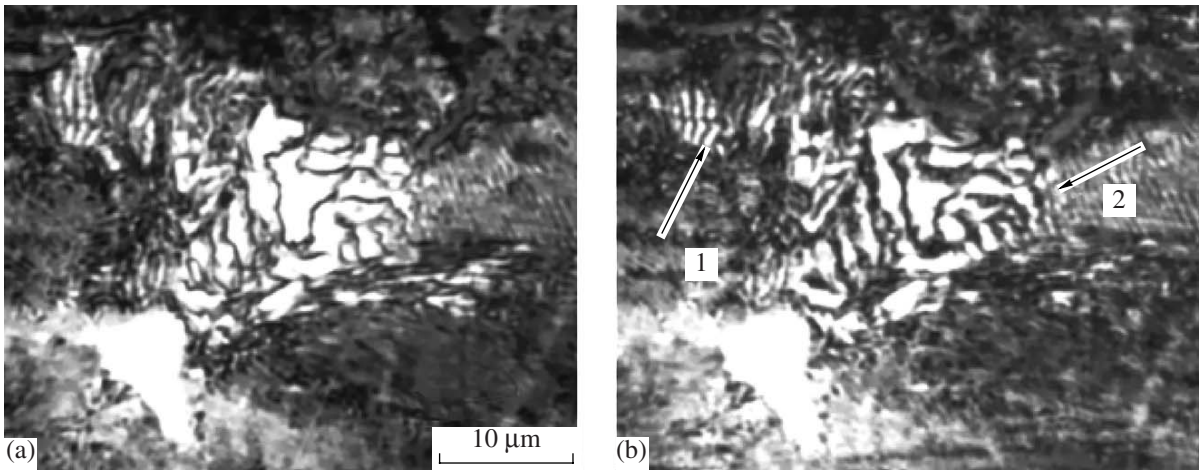

Fig. 6. Change in the large fragment of eutectics after WFMPT: (a) initial state; (b) after four cycles of treatment.

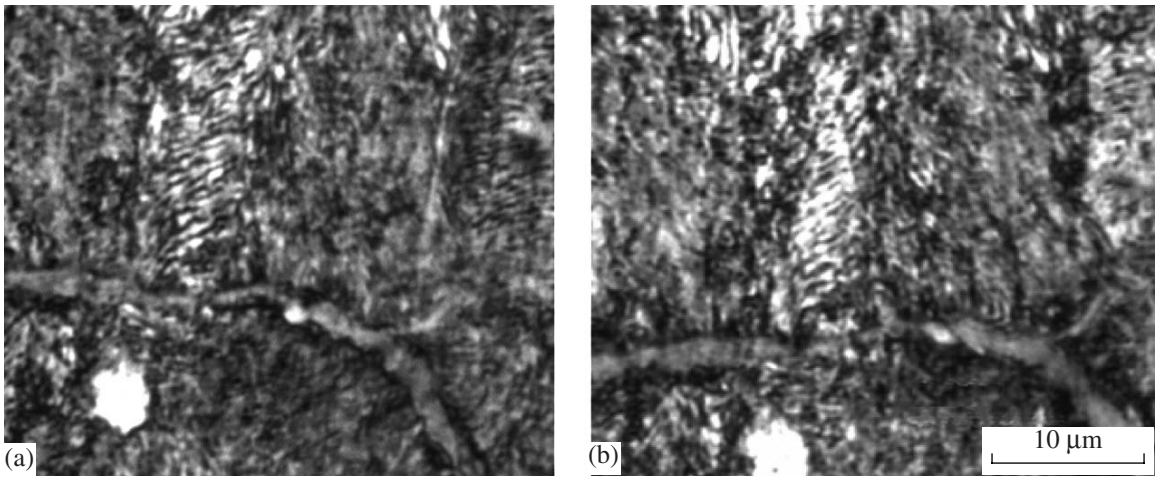

Fig. 7. Change in the eutectic grain morphology after WFMPT: (a) initial state; (b) after two cycles of treatment.

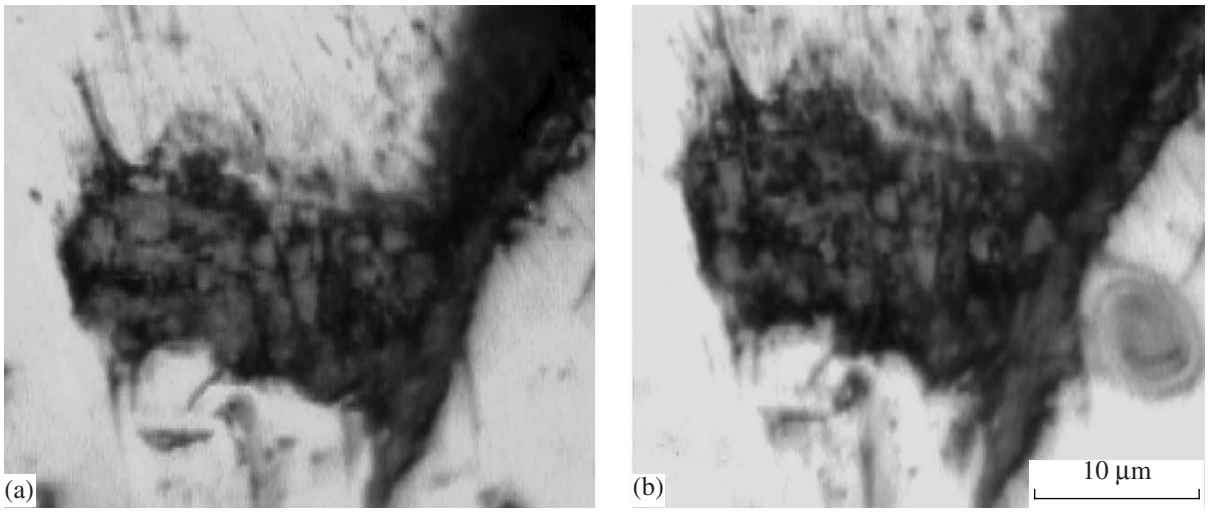

Fig. 8. Change in the graphite structure at WFMPT after six (a) and eight (b) cycles of treatment.

of ferrite and cementite, their cleavage (Fig. 6, arrow *1*), and a change in length (Fig. 6, arrow *2*) are observed. Figure 7 presents the transformation of eutectic grains.

A characteristic feature of the WFMPT process is a change in the nonferromagnetic phases of the cast iron. The free-cementite inclusions change their form; a decrease in their thickness and fragmentation of the inclusions are observed (see Fig. 5).

The graphite inclusions coarsen with simultaneous transformation of their internal structure (Fig. 8).

The X-ray pattern analysis has shown that the WFMPT, with no change in the phase composition of the cast iron, leads to a change in the ratio between the intensities of the interference lines of the phases: ferrite, graphite, and cementite. As one can see from Table 1, the ratio of the interference line intensities in the initial cast state is inconsistent with the table data of [21], whereas, after the MPT, the ratio of the intensities almost coincides with the calculated values of [21]. The effect appears to be due to stabilization of the ferrite phase and to a decrease in the internal stress level. The decrease in the absolute intensity of the ferrite line taking place therein may be explained by the decrease in the free-ferrite content in the cast iron structure. The change in the relative intensities of the ferrite lines can be attributed to the availability of a texture. Usually, in the process of casting, a ⟨100⟩ texture develops in iron and its alloys [22]. At the same time, it is known that, in the course of continuous and piped casting, the second type of oriented crystals of casting can appear. This may explain the development of a ⟨110⟩ texture of the initial state in the course of continuous casting. The change in the ratio of the interference line intensities may also be attributed to the elimination of the casting texture at WFMPT.

As regards carbon and cementite, one can observe (Table 2) an increase in the intensities of their interference lines with a small sum of squared indexes with respect to the ferrite interference line (110) and a decrease in the intensities or disappearance of lines with a large sum of squared indexes. It is possible that this is attributed to an increase in the microstress level in the given phases due to the change in their morphology and structure at WFMPT (Fig. 6).

The found structural changes in the cast iron can cause a change in its strength. With the view to reveal such a possibility, the following automobile parts of СЧ-25 cast iron were subjected to WFMPT: transmis-

Table 1. Change in the intensities of the ferrite interference lines for the initial cast iron sample and after its exposure to WFMPT

HKL	2θ, deg	*d*, Å	Intensity		
			For the initial sample, mm (%)	For the same sample after WFMPT, mm (%)	Calculated values, %
(110)	44.833	2.024	1480 (100)	593 (100)	100
(200)	65.083	1.434	103 (7)	90 (17)	19
(211)	82.500	1.170	204 (14)	171 (33)	30
(220)	99.083	1.014	45 (3)	40 (7)	9
(310)	116.500	0.907	39 (2.5)	58 (12)	12

Table 2. Change in the intensities of the lines of carbon and cementite after WFMPT

Intensity, %					
Carbon			Cementite		
HKL	For the initial sample	For the same sample after WFMPT	HKL	For the initial sample	For the same sample after WFMPT
002	0.7	6.8	112	0.4	1.91
100	0.6	2.5	121	0.6	–
004	–	1.09	210	0.9	4.6
112	0.36	–	113	0.14	–
			122	0.4	1.6
			025	0.7	–
			136	1.07	–

sion gasket rings *1* and *3* and pneumatic-compressor piston ring *2* (Fig. 9). The rings were treated according to a time cyclogram (see Fig. 2). The number of ordinary cycles n for different specimens of each sample was 2, 4, and 8. The change in the strength of the parts resulting from WFMPT was estimated by measurement of their hardness by means of a hardness meter by the Super-Rockwell method with subsequent conversion of the obtained HRA values into Brinell hardness numbers (HB). The measurement results are given in Table 3, from which one can see that WFMPT improves the hardness of cast iron. In particular, after WFMPT, the hardness of the pneumatic-compressor piston ring increased from 177 to 208 HB.

It should be noted that, at present, most of the works are concerned with the study of the magnetic field influence on structural changes in metals and alloys simultaneously with their heat treatment [15–16, 23–25]. It has been found quite reliably that the MPT of metals and alloys leads to a change in the density of the dislocations and dispersion of structure, to intensification of the diffusion processes, increase in the point defect concentration, and change in the structure and physicomechanical characteristics depending on the number of treatment cycles, as well as to the formation of inhomogeneous states of stress. However, there is no clear-cut and consistent idea of how the magnetic field interacts with metals and alloys. This is due to both the synergetics of the field-induced physicochemical processes in the sample under treatment and the difficulties in its diagnostics and the interpretation of the obtained results.

At the same time, the found specific features of MPT, as well as the given-in-[3] results of the analysis of different methods of high-energy treatment of materials, allow us to assume the similarity of the structural effects caused by magnetic-pulse and other types of short-term exposure.

On this basis, we can consider that the formation of the structure of metals and alloys at MPT is determined by processes similar, in the structural effect, to deformation or heating. On the one hand, coarsening of graphite inclusions is a characteristic feature of exposure to heat. The change in the ratio of the line intensities in the X-ray pattern of an alloy is a relaxation process, resulting in the formation of an equilibrium structure. On the other hand, the phenomenon of eutectics dispersion during MPT is not determined by processes similar to annealing (that is, leading to structure coarsening). Under conditions during MPT, when direct heating and plastic deformation are absent, a change in the eutectic component may take place due to complete transformation of the eutectic grain, including its reorientation and formation of large-angle boundaries.

It is known that the MPT method is based on local absorption of energy W_0 of the magnetic field by structure inhomogeneities of the material and on its transition from one nonequilibrium state to another characterized by higher stability. Herein, two basic channels of dissipation of W_0 are recognized: magnetization of the material and local heat losses of W_0 due to the appearance of eddy microcurrents in its body. In the

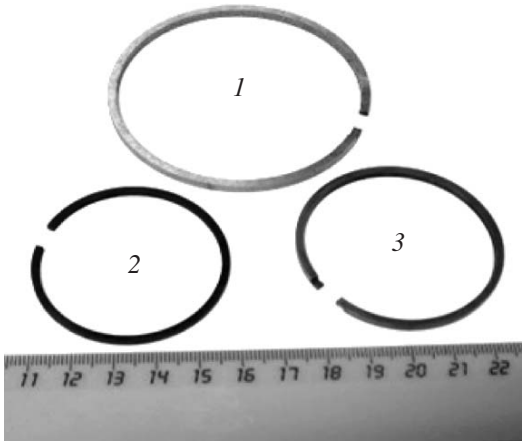

Fig. 9. Automobile parts of cast iron.

Table 3. Change in the hardness of cast iron parts after WFMPT

Sample no.	Designation	Cycle number, n	HRA	HB
1	Transmission gasket ring (D = 70 mm)	0	58	197
		2	58	197
		4	58.3	201.6
		8	58	197
2	Pneumatic-compressor piston ring (D = 47 mm)	0	55.6	177.6
		2	59.7	208
		4	57.3	190.6
		8	58.3	201.6
3	Transmission gasket ring (D = 50 mm)	0	55	170
		2	55.7	175.6
		4	53	171.3
		8	56	179

process of magnetization, under the action of the magnetic force moment $K = \mu H$, in the material structure, a displacement of domain boundaries occurs, in which the magnetization μ is oriented close to the field direction H, leading to an increase in their volumes due to a change in the volume of neighboring domains, as well as a change in the direction of spontaneous magnetization of separate domains and crystallites by rotation of the magnetization vector μ [14]. In a pulse-periodic magnetic field, as the value of its intensity H increases, the magnetization of the structure elements in the material under treatment continues up to the saturation induction. After that, as the values of H decrease, it falls to the residual induction. As a result, due to the difference in the values of the saturation induction and residual induction, the magnetostriction effect takes place.

In cast iron, due to the difference in the magnetic properties of the ferrite [26], cementite [27], and graphite [28] available in it, the magnetostriction value of the different phases is appreciably different; therefore, in the process of WFMPT, an inhomogeneous stress state can be formed in cast iron. Therein, the value of the microdeformation in the maximum can be from a few to tens MPa [3]. The magnetostriction deformation may play the role of a deformation factor, similar to thermal deformations in the course of thermal cycling [3], under the influence of which defects of the crystal structure accumulate. The conditions of plastic deformation during pulse treatments of materials considerably differ from the conditions of static deformation due to the short duration and periodicity of the force impact and to the difference of the internal-stress relaxation procedures. Relaxation processes, in their turn, exert a significant influence on the atom mobility and mass transfer in the material.

Pulse actions (thermal, magnetic, ultrasonic, and laser) of respective power initiate an anomalous mass transfer in metals and alloys. The increase in the diffusion coefficient under pulse actions can amount to several orders. Intense diffusion processes play the role of an analog of thermal exposure.

The structure formation in metals must be regarded as a result of the deformation effect on pulse loading and the relaxation effect under the action of the load and its removal. Under pulse actions, the deformation processes and stress relaxation repeat periodically [3]. The principal relaxation procedure implemented under pulse actions may be considered the diffusion–shear one. The basic relaxation process is fragmentation [3]; its key specific feature is formation of large-angle boundaries of the deformation type with high density of the grain-boundary dislocations.

Healing of surface defects is a direct manifestation of relaxation processes. The possibility of healing of defects in metals in pulse magnetic fields is mentioned in works [29–30]. By analogy with the mass transfer process in conditions of pulse mechanical loading, the authors of [29–30] assume that, in conditions of the pulse-magnetic field action, the dominating contribution to mass transfer is made by interstitial atoms, the motion of which determines the sharp increase in the diffusion of atoms in metals in a pulse magnetic field. However, the data on the influence of alternating and pulse magnetic fields on the diffusion and diffusion-controlled processes in solids are extremely scarce. Direct studies of the alternating magnetic field influence on heterodiffusion in metals and alloys are described in [31].

The classical procedure of defect healing is attributed to the formation and motion of large-angle boundaries in the process of recrystallization. This procedure was proposed in [32] for the description of a change in porosity in the sintering process. In the course of motion, the boundary approaches separate pores; as a consequence, they appear to be near the vacancy sink. The moving boundary "sweeps" pores before itself. Implementation of this procedure requires long-term annealing at high temperature.

The effect of pore healing under heat pulse treatment was explained on the basis of the diffusion–dislocation procedure characteristic of high values of stresses and temperatures in conditions of all-around compression [33]. An additional factor (along with the deformation factor due to continuous variation in temperature) favoring the appearance of the all-around compression component is the surface pressure at the matrix–pore interface that depends on the surface tension and interfacial curvature. The diffusion–dislocation procedure of pore healing takes into account the participation of dislocations in the mass transfer process. The main role is assigned to dislocation loops generated by pores at stresses close to the theoretical strength of the matrix. The estimate of the pressure that ensures the pore healing [33] gives a value on the order of 10 GPa. For the pulse action conditions, this pressure can decrease, since dislocation loops appear as a result

of a "collapse" of vacancy disks and prismatic dislocation loops [27]. The principal procedure of pore healing at thermal-cycle treatment, along with the diffusion–dislocation one, is the vacancy procedure. Its action is determined by a change in the dislocation density on the surface of a pore due to the development of the processes of work hardening and softening. Herein, the stresses around the pore partially relax.

CONCLUSIONS

As a result of the carried out research, it has been found that the structure effects of the applied WFMPT on СЧ-25 cast iron are healing of the surface defects, perlite dispersion, a decrease in the ferrite content in the structure due to the ferrite–graphite complex transformation into perlite, coarsening and modification of the internal structure of graphite inclusions, and a change in the cementite morphology.

The observed structural changes cause an increase in hardness of automobile parts made of СЧ-25 cast iron.

A detailed analysis of the procedures of the metal structure change under the action of a pulse-periodic magnetic field requires further experimental and theoretical research in physical metallurgy and related branches.

ACKNOWLEDGMENTS

This work was supported by the Foundation for Basic Research of the Republic of Belarus and by the Mogilev Executive Committee within the Program of Development for the Mogilev Region (project no. Mg-01).

REFERENCES

1. Marukovich, E.I., Bevza, V.F., and Grusha, V.P., Realization of the Concept of Wall Crystallization for Obtaining of High-Quality Hollow Cylindrical Works of Cast Iron, in *Materialy, tekhnologii i oborudovanie v proizvodstve, ekspluatatsii, remonte i modernizatsii mashin* (Materials, Technologies, and Equipment in Production, Operation, Maintenance, and Modernization of Machines), Novopolotsk, 2007, vol. 1, pp. 33–35.
2. Gorelik, S.S., Dobatkin, S.V., and Kaputkina, L.M., *Rekristallizatsiya metallov i splavov* (Recrystallization of Metals and Alloys), Moscow: MISIS, 2005.
3. Anisovich, A.G., Structure Formation Process Generalities and Thermodynamic Aspect in Organization of Metal Structure under Unsteady Energy Depositions, *Extended Abstract of Cand. Sci. (Phys.–Math.) Dissertation*, Minsk, 2005.
4. Martin, J.W. and Doherty, R.D., *Stability of Microstructure in Metallic Systems*, London: Cambridge Univ. Press, 1976; Moscow: Atomizdat, 1978, pp. 247–252.
5. Anisovich, A.G., Pulse Methods of Metal Treatment, *Tender*, 2006, no. 56, pp. 14–16.
6. Koksharov, S.A., Konstantinov, O.I., Mel'nikov, B.N., and Moryganov, A.P., Magnetic Field Influence on the State of Solutions of Reactive Dyes, *Zh. Prikl. Khim.*, 1990, vol. 63, no. 3, pp. 565–571.
7. Bingi, V.N. and Savin, A.V., Physical Problems of Weak Magnetic Field Influence on Biological Systems, *Usp. Fiz. Nauk*, 2003, vol. 173, no. 3, pp. 265–300.
8. Gorodetskaya, E.A., Spiridovich, E.V., Korevko, I.A., Azharonok, V.V., Filatova, I.I., and Nekrashevich, Ya.I., Influence of Plasma–Radio-Wave Treatment on the Sowing Properties of Seeds, *Dokl. Nats. Akad. Nauk Belarusi*, 2007, vol. 51, no. 6, pp. 256–262.
9. Azharonok, V.V., Filatova, I.I., Voshchula, I.V., Dlugunovich, V.A., Tsariuk, O.V., and Gorzhanova, T.N., Change of Optic Properties of Paper under the Influence of the Magnetic Component of a High-Frequency Electromagnetic Field, *Zh. Prikl. Spektrosk.*, 2007, vol. 74, no. 4, pp. 421–426.
10. Persidskaya, A.Yu., Kuzeev, I.P., and Antipin, V.A., On the Influence of Pulse Magnetic Field on the Mechanical Properties of Polymer Fibers, *Khim. Fiz.*, 2002, vol. 21, no. 2, pp. 90–98.
11. Gul', V.E., Khanchich, O.A., and Savchenko, N.A., The Homogeneous Magnetic Field Influence on Thermotropic Liquid-Crystal Copolymer of Hydroxybenzoic Acid and Ethylene Terephthalate, *Mekh. Kompoz. Mater. Konstruktsii*, 1995, vol. 1, no. 2, pp. 124–128.
12. Schastlivtsev, V.M., Romashev, L.N., Yakovleva, I.L., and Sadovskii, V.D., Electron Microscope Investigation of the Structure of Martensite Crystals Nucleated under the Action of Pulse Magnetic Field, *Fiz. Met. Metalloved.*, 1981, vol. 51, no. 4, pp. 773–782.
13. Zdor, G.N., Anisovich, A.G., and Yaskovich, A.G., Application of Pulse Magnetic Field for Improvement of the Mechanical Properties of Nonferrous Metal Alloys, *Probl. Mashinostr. Nadezhn. Mashin*, 2004 no. 5, pp. 65–70.
14. Malygin, B.V., *Magnitnoe uprochnenie instrumenta i detalei mashin* (Magnetic Hardening of Tools and Machine Parts), Moscow: Mashinostroenie, 1989.
15. Agapova, E.V., Gundyrev, V.M., and Sidorov, E.V., About Structural Changes in the YuNDK35T5AA Alloy upon Magnetic Annealing. *Fiz. Met. Metalloved.*, 2006, vol. 102, no. 2, pp. 178–183 [*Phys. Met. Metallogr.* (Engl. Transl.), vol. 102, no. 2, p. 163].
16. Kaletina, Yu.V., Fokina, E.A., and Schastlivtsev, V.M., Effect of Pulsed and DC Magnetic Fields on the Martensitic Transformation in Alloys with Isothermal Kinetics., *Fiz. Met. Metalloved.*, 2005, vol. 99, no. 1, pp. 31–37 [*Phys. Met. Metallogr.* (Engl. Transl.), vol. 99, no. 1, p. 26].
17. Montgomery, D.B., *Poluchenie sil'nykh magnitnykh polei s pomoshch'yu solenoidov* (Obtaining of Strong Magnetic Fields by Solenoids), Moscow: Mir, 1971 (Russian translation).
18. Gvozdev, A.G., Borodin, I.P., Gvozdeva, L.I., Sushkova, T.V., and Pakhomov, A.A, Study of the Influence of Treatment in a Pulse Magnetic Field on the Properties of 4Kh5MF1S Steel, *Materialy V Mezhdunarodnoi nauchnoi konferentsii "Prochnost' i razrushenie materialov i konstruktsii"* (Proc. V Int. Sci. Conf. on Strength and Damage of Materials and Structures), Orenburg, 2008, vol. 1, pp. 370–373.

19. Zdor, G.N., Anisovich, A.G., Shimanovich, V.D., Azharonok, V.V., and Dresvin, S.V., Transformation of Structure and Properties of Beryllium Bronze under the Influence of High-Frequency Magnetic Field, *Izv. Ross. Akad. Nauk, Ser.: Met.*, 2003, no. 4, pp. 100–105.
20. Maslovskii, V.M., On the Influence of Weak Magnetic Field on Structure of Condensed Media, *Materialy IV Mezhdunarodnogo nauchno–tekhnicheskogo seminara po netraditsionnym tekhnologiyam* (Proc. IV Int. Sci.–Tech. Seminar on Unconventional Technologies), Botevgrad, Sofiya–Gor'kii, 1989, pp. 5–14.
21. Gorelik, S.S., Rastorguev, L.N., and Skakov, Yu.A., *Rentgenograficheskii i elektronno–opticheskii analiz. Prilozhenie* (Roentgenographic and Electron–Optical Analysis. Supplement), Moscow: Metallurgiya, 1970.
22. Wasserman, G. and Grewen, J., *Tekstury metallicheskikh materialov* (Texture of Metal Materials), Moscow: Metallurgiya, 1969 (Translation from German).
23. Fokina, E.A., Kaletina, Yu.V., and Schastlivtsev, V.M., Specific Features of the Martensitic Transformation of Deformed Austenite in the 50N26 Alloy upon Cooling and Magnetic Treatment, *Fiz. Met. Metalloved.*, 2006, vol. 101, no. 4, pp. 381–391 [*Phys. Met. Metallogr.* (Engl. Transl.), vol. 101, no. 4, p. 355].
24. Pustovoit, V.N. and Sorochkina, O.Yu., The Influence of External Magnetic Field in the Temperature Range of Martensitic Transformation Superplasticity, *Bernchteinovskie chteniya "Termoelektricheskaya obrabotka metallicheskikh materialov"* (Bernstein Readings on Thermomechanical Treatment of Metal Materials), Moscow, 2004, p. 32.
25. Klevtsova, N.A., Klevtsov, G.V., and Fesenyuk, M.V., The Influence of Magnetic Field and Low Temperature on Martensitic Transformations in the Fe–Cr–Mn–V Alloy, *Materialy V Mezhdunarodnoi nauchnoi konferentsii "Prochnost' i razrushenie materialov i konstruktsii"* (Proc. V Int. Sci. Conf. on Strength and Damage of Materials and Structures), Orenburg, 2008, vol. 1, pp. 16–20.
26. Prokhorova, A.M., *Fizicheskii entsiklopedicheskii slovar'* (Physical Encyclopedic Dictionary), Sovetskaya entsiklopediya, Ed., Moscow, 1983, pp. 384–386.
27. Drapkin, B.M. and Kimstach, G.M., Magnetic Properties of Cementite in Iron–Carbon Steels, *Fiz. Met. Metalloved.*, 1995, vol. 80, no. 2, pp. 163–166.
28. Makarova, T.L., Magnetic Properties of Carbon Structures. Review), *Fiz. Tekh. Poluprovodn.*, 2004, vol. 38, no. 4, pp. 641–664.
29. Larikov, L.N., *Zalechivanie defektov v metallakh* (Healing of Defects in Metals), Kiev: Naukova Dumka, 1980.
30. Larikov, L.N., Fal'chenko, V.M., and Gertsriken, S.D., On the Influence of Pulse Magnetic Field on Atom Mobility in Iron and Aluminum, *Dokl. Akad. Nauk SSSR*, 1978, vol. 239, no. 2, pp. 312–314.
31. Verazhkovskaya, M.A., Petrov, S.S., and Pokoev, A.V., Heterodiffusion of Al in α–Fe in a Pulse Magnetic Field, *Pis'ma Zh. Tekh. Fiz.*, 2007, vol. 33, issue 22, pp. 43–47.
32. Geguzin, Ya.E., *Makroskopichekie defekty v kristallakh* (Macroscopic Defects in Crystals), Moscow: Gos. Nauchno–Tekh. Izd. Liter. Chern. Tsvetn. Metall., 1962.
33. Tofpenets, R.L., Sokolov, Yu.V., Zaluzhnyi, G.I., and Popok, D.A, Procedure and Kinetics of Pore Healing at TCT of Sprayed Coatings, *Vestsi Nats. Akad. Navuk Belarusi, Ser. Fiz.–Tekh. Navuk*, 1999, no. 2, pp. 10–13.

ISSN 1068-3755, Surface Engineering and Applied Electrochemistry, 2009, Vol. 45, No. 2, pp. 125–127. © Allerton Press, Inc., 2009.
Original Russian Text © M.K. Bologa, F.P. Grosu, A.A. Polikarpov, O.V. Motorin, 2009, published in Elektronnaya Obrabotka Materialov, 2009, No. 2, pp. 57–60.

ELECTRICAL PROCESSES IN ENGINEERING AND CHEMISTRY

Condensation of a Gas–Vapor Mixture in an Electric Field

M. K. Bologa[a], F. P. Grosu[b], A. A. Polikarpov[a], and O. V. Motorin[a]

[a]*Institute of Applied Physics, Academy of Sciences of Moldova, ul. Academiei 5, Chisinau, MD-2028 Republic of Moldova*
e-mail: mbologa@phys.asm.md
[b]*Moldova State Agrarian University, ul. Mircesti 44, Chisinau, MD-2049 Republic of Moldova*

Received December 18, 2008

Abstract—Condensation of a gas–vapor mixture in a direct electric field is discussed in this paper. At a noncondensable gas concentration of 5%, an approximately two-fold increase in the condensed liquid amount is obtained. The condensation process enhancement is explained by the cooperative effect of the condensate film turbulization and the decrease in the diffusion resistance of the noncondensable gas layer in an electric field. The obtained results can be used for the design of electrohydrodynamic generators and compact vapor condensers.

DOI: 10.3103/S1068375509020070

The processes of condensation in the presence of noncondensable gases are common in power engineering; in the chemical, oil-refining, and food industries; in refrigeration and cryogenic engineering; and in air conditioning systems. An increase in generating capacities is connected with an increase in the weight and dimensions of the heat interchangers, for the production of which a great amount of doped and nonferrous metals are utilized. Therefore, a decrease in the weight and dimensions of heat-exchanging units is still a problem of high priority. The most promising line of attack on the problem is the enhancement of heat-exchange processes. To date, various methods of condensation enhancement have been studied and proposed, in particular, the use of ribs as turbulizers of condensate films, nonwettable coatings, liquid stimulating agents for initiation of drop condensation, vortex generation, and rotation of the heat-exchange surface. A very promising method for condensation enhancement is the application of electric fields. The condensation in vertical tubes was studied theoretically and experimentally in works of Chato [1]. Chen et al. [2] analyzed film condensation in a vertical tube and obtained an analytical dependence for the mean Nusselt number. In works of Webb [3], Cavallini et al. [4], Muir [5], and Yang and Webb [6], the enhancement of condensation of R-134a and R-22 cooling agents by microribbing was considered (at a change in the rib height from 0.1 to 0.25 mm).

Gerstman and Choi [7] have shown the possibility to enhance condensation on a vertical plate by exposure of the film thickness to an electric field. Velkoff and Miller [8] studied condensation of R-113 vapors on a vertical copper plate at different field intensities and electrode geometries. The experimental studies carried out by Seth and Lee [9] showed the possibility to enhance the vapor condensation from a gas–vapor medium in an electric field. Later on, results of detailed studies on the condensation of vapors of dielectric liquids from a gas–vapor mixture were obtained by other authors as well [10–14]. However, data on the influence of an electric field on condensation of conducting liquids, including water, can hardly be found at all. The relevance of such research is imposed by the necessity to reveal the specific character of the interaction of two-phase conducting systems and electric fields and the possibility to use the condensed liquid in electrohydrodynamic generators [15].

In the first part of the research carried out [16], we showed the possibility of atmospheric moisture use in an electrohydrodynamic generator and studied the condensation of a gas–vapor mixture in the absence of an electric field. The aim of this work is the experimental study of the influence of an electric field on the condensation of water vapor from a gas–vapor mixture.

The study of the condensation process was carried out by means of an experimental installation; its diagram is shown in Fig. 1. The working liquid was heated to boiling in vessel *9*. The formed vapor proceeded into the lower part of a vertical tube with a length of 80 cm and a diameter of 28 mm, where it was mixed with air and condensed on the inner surface of the tube. The formed condensate dripped down and arrived into a measuring vessel. From the outside, the tube was blown with a flow of air with a controlled velocity. A copper wire electrode in varnish insulation with a diameter of 3 mm with scratches was placed in axial alignment inside the tube. Direct voltage from a high-voltage supply of the AII-70 type was applied to the inner electrode; the tube used for the second electrode was connected to the ground through a milliampere meter. The vapor consumption was measured according to the

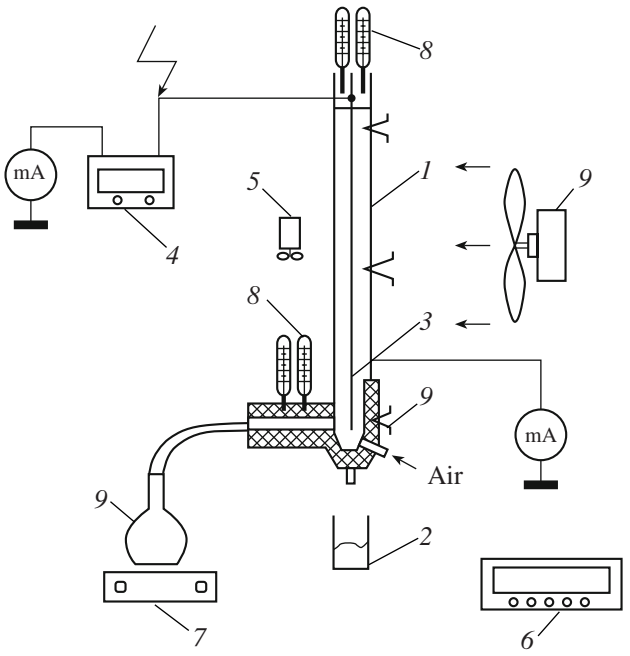

Fig. 1. Diagram of the sector of the condensation of a gas–vapor mixture: *1* is the tube–condenser of the vapor, *2* is the condensate receiver, *3* is the high-voltage electrode, *4* is the high-voltage supply, *5* is the anemometer, *6* is the temperature measurement unit, *7* is the vapor generator, *8* are thermometers, and *9* is the blower.

mass of the evaporated water and the duration of the experiment. The tube's surface temperature was measured by means of thermocouples installed in the beginning, in the center, and in the end of the tube. The humidity and the temperature of the vapor at the output of the tube were determined by virtue of a psychrometer; the consumption of air fed into the condenser was measured with a rotameter.

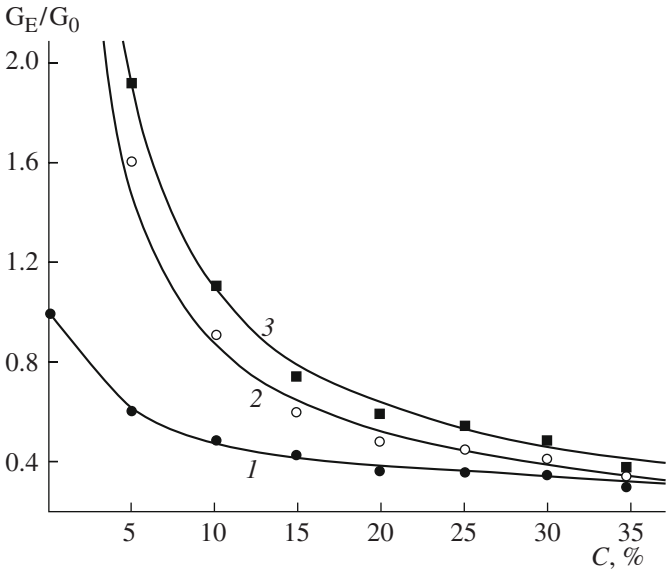

Fig. 2. Dependence of the condensate fraction on the air concentration at different current intensities, mA: (*1*) 0; (*2*) 1; (*3*) 2. V_{air} = 3.5 m/s.

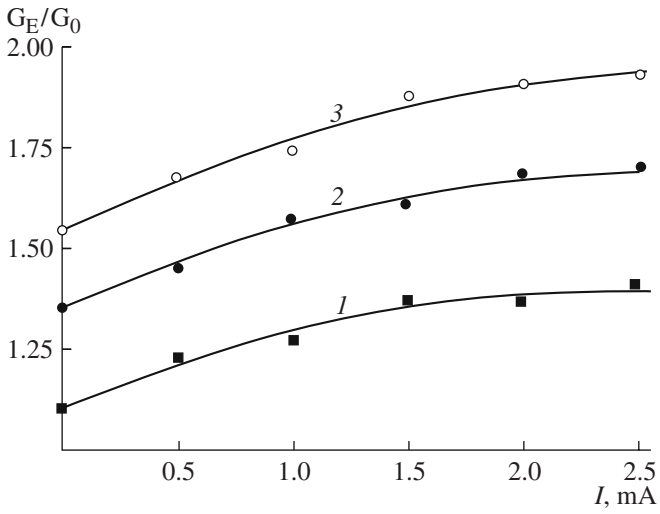

Fig. 3. Dependence of the condensate fraction on the current intensity at different velocities of blowing, c = 5%: (*1*) 1.3 m/s; (*2*) 2.0 m/s; (*3*) 3.5 m/s.

The velocity of the air blowing over the outer surface of the tube was measured by means of an anemometer. The experiments were carried out with the measurement of the process parameters in the following ranges: 0–35% for the noncondensable gas concentration, 0–3.5 m/s for the airflow velocity, and up to 15 kV for the voltage. The choice of the variation range for the velocity of the tube surface blowing over was determined by the characteristic range of the wind velocities in the conditions of Moldova. The maximum voltage value was limited by the breakdown of the interelectrode gap.

Figure 2 presents the dependences of the obtained condensate fraction on the air concentration at different current intensities of the corona discharge. The maximum degree of intensification is 1.9. The obtained results testify to a monotonous decrease in the degree of enhancement with increasing gas concentration both in the presence of the electric field and in its absence. The rate of the curves may be explained by the fact that the diffusion thermal resistance plays the key role even at very small concentrations of noncondensable gas.

Dependences of the condensate fraction on the current intensity at different velocities of the air blowing over the tube are given in Fig. 3. As the current intensity increased up to the breakdown of the interelectrode gap, an increase in the amount of the obtained condensate was observed. The corona discharge appearing at certain potential difference causes intense dispersion of the condensate film and its thinning. In addition,

intense agitation of the gas–vapor mixture occurs, which contributes to a decrease in the diffusion resistance. An increase in the velocity of the tube blowing over causes turbulization of the blowing airflow, which also favors the process enhancement.

Thus, the possibility of considerable enhancement of the condensation process in an electric field due to the condensate film turbulization and to the decrease in the diffusion resistance to the vapor transfer has been experimentally confirmed. At a noncondensable gas concentration of 5%, an approximately two-fold increase in the condensate amount has been obtained. The results can be used for the design of electrohydrodynamic generators and for the preparation of compact vapor condensers.

REFERENCES

1. Chato, J.C., Laminar Condensation inside Horizontal and Inclined Tubes, *Ph.D. Dissertation*, Cambridge, Department of Mechanical Engineering, MIT, MA, 1960.
2. Chen, S.L., Gerner, F.M., and Tien C.L., General Film Condensation Correlations, *Exp. Heat Transfer*, 1987, vol. 1, pp. 93–107.
3. Webb, R.L., *Principles of Enhanced Heat Transfer*, New York: Wiley–Interscience, 1994.
4. Cavallini, A., Censi, G., Del Co, D., Doretti, L., Longo, G.A., and Rossetto L., In-Tube Condensation of Halogenated Refrigerants, *ASHRAE Trans.*, 2002, vol. 108, no. 1, pp. 146–161.
5. Muir, E.B., Commercial Refrigerants and CFCs, in CFCs: Today's Options—Tomorrow's Solutions, *Proc. ASHRAE's 1989 CFC Technology Conf.*, 1989, pp. 81–86.
6. Yang, C.Y. and Webb, R.L., A Predictive Model for Condensation in Small Hydraulic Diameter Tubes Having Axial Microfins, *J. Heat Transfer ASME,* 1997, vol. 119, pp. 776–782.
7. Gerstman, J. and Choi, H.Y., Electrohydrodynamics Effects in Condensation, *Report 62–3*, Department of Mechanical Engineering, Tufts University, 1962.
8. Velkoff, H.R. and Miller, J.H., Condensation of Vapor on a Vertical Plate with a Transverse Electrostatic Field, *J. Heat Transfer ASME*, 1965, pp. 197–201.
9. Seth, A.K. and Lee, L., The Effect of an Electric Field in the Presence of Noncondensable Gas on Film Condensation Heat Transfer, *J. Heat Transfer ASME*, 1970, vol. 9, no. 1, pp. 616–620.
10. Savin, I.K., Bologa, M.K., and Didkovskii, A.B., The Electric Field Influence on Heat Transfer at Film Condensation of Vapor in the Presence of a Noncondensable Gas, *Elektron. Obrab. Mater.*, 1981, no. 2, pp. 41–44.
11. Savin, I.K., Didkovskii, A.B., and Bologa, M.K., Enhancement of Heat Exchange at Film Condensation of Vapor from a Gas–Vapor Mixture under the Electric Field Influence, *Elektron. Obrab. Mater.*, 1983, no. 2, pp. 59–63.
12. Savin, I.K., Didkovskii, A.B., and Bologa, M.K., Features of Heat Exchange at Vapor Condensation from a Gas–Vapor Mixture in the Range of Low Temperature Drops under the EHD Influence, *Elektron. Obrab. Mater.*, 1983, no, 5, pp. 52–56.
13. Wawzyniak, M., Motte, E., and Seyed–Yagoobi, J., Experimental Study of Electrohydrodynamically Augmented Condensation Heat Transfer, *Industry Applications Society Annual Meeting, 1994, Conference Record of the 1994 IEEE*, 1994, vol. 3, pp. 1653–1660.
14. Sadek, H., Robinson, A.J., Cotton, J.S., Ching, C.Y. and Shoukri, M., Electrohydrodynamic Enhancement of In-Tube Convective Condensation Heat Transfer, *Int. J. Heat Mass Transfer*, 2006, vol. 49, issues 9–10, pp. 1647–1657.
15. Cojuhari, I. and Bologa, M., Moldova Inventor's Certificate no. Md–2199, (13) B1, 2003.
16. Grosu, F.P., Bologa, M.K., Polikarpov, A.A. and Motorin, O.V., On Modeling of Processes of Moisture Circulation and Electric Charge Separation in the Atmosphere, *Elektron. Obrab. Mater.*, 2007, no. 3, pp. 29–35 [*Surf. Eng. Appl. Electrochem.* (Engl. Transl.), vol. 43, no. 3, p. 176].

ISSN 1068-3755, Surface Engineering and Applied Electrochemistry, 2009, Vol. 45, No. 2, pp. 128–132. © Allerton Press, Inc., 2009.

ELECTRICAL PROCESSES IN ENGINEERING AND CHEMISTRY

Kinetic Parameters-Analysis and Prognosis Items of the Nitriding Process

M. Cojocaru, I. Ciuca, L. Druga, G. Cosmeleata

"POLITEHNICA" University Bucharest, Splaiul Independentei, 313, 060042, Bucuresti, Romania

e-mail: office@uttis.ro

Received October 13, 2008

Abstract—The lack of practical information regarding the kinetics of a thermal process can be compensated by estimating the kinetic parameters of the process. Using the methodology imposed by Baram, as well as to one resulted form the use of the solution to the Fick's differential equation, through a minimum number of experiences, can be obtained sufficient information to estimate the process' average speed, its activation energy, the diffusion coefficient, etc., and forecast the saturation effects in conditions different from those used for experiments to obtain preliminary information. This paper presents the experimental results obtained during the nitriding of pure technical iron and respectively of a nitraloy type alloyed steel for improvement, regarding the kinetic of the nitrided layers' growth and starting from this results, the calculated values of the of the kinetic parameters, respectively the forecasted values of the kinetics in conditions different from those effectively used during experiments.

DOI: 10.3103/S1068375509020082

THE THEORETICAL BASE OF THE ISSUE

Baram [1] gives as main use for the extended equation of the heterogeneous reactions' kinetics, (Eq. (1)), to describe the phenomena that take place during the thermo-chemical processing of metals and alloys. The equation was obtained using the masses' action law and the phenomenological dependency of the time related variation of the inter phases separation areas' size (Eq. (2)) in solid bodies undergoing thermo-chemical processes.

$$K^* = \frac{(1-\alpha)V^n}{S_0 t^{1-\alpha}} \int_{m_0}^{m} \frac{dm}{[CV-(m-m_0)]^n} \quad (1)$$

$$S = K' S_0 \frac{1}{t^{\alpha}} \quad (2)$$

where S_0 represents the initial area of the solid phase; m_0 and m the mass of the solid phase at the beginning, respectively in the moment t of the process; V—the volume of the phase undergoing the processing; C—the limit concentration of the saturation element in the solid phase (the value will take into account the initial concentration of the element, respectively the chemistry of the process) n the grade of the inter phase reaction, depending on the type of the cementing element; α constant (kinetic parameter), depending on the individual property of the reacting phases; in case $\alpha \longrightarrow 0$, $(1-\alpha) \longrightarrow 1$, the process develops in the kinetic domain, the reactions on the interface reaction medium—metallic product are dominant and the inter phase reaction area is considered to remain unchanged; in case $\alpha \longrightarrow 1$, $(1-\alpha) \longrightarrow 0$, the speed of the layer forming process is limited by the speed at which develop the diffusion processes within the metallic matrix, the later ones representing the dominant processes, and the inter phase separation area changes; K^*—the constant of the process speed; its measuring units are the ones corresponding to the multiplication: $m^{1-n}V^n S^{-2} t^{\alpha-1}$, where m, V, S and t are the measuring units for mass, volume, area and time.

In case there is an exceeding of the cementing element in the medium, the variation in time of its concentration can be ignored (the most frequent case in the thermo-chemical treatment practice), the grade of the inter phase reaction becomes zero ($n = 0$), and through the integration of the Eq. (1) results the relation (Eq. (3))

$$K_0^* = \frac{(1-\alpha)\Delta m}{S_0 t^{1-\alpha}} \quad (3)$$

where $\Delta m = m - m_0$ represents the mass variation of the solid phase; If we consider the relation:

$$\delta = K' \Delta m \quad (4)$$

where δ represents the size of the cemented layer, results:

$$K_0 = \frac{(1-\alpha)\delta}{t^{1-\alpha}} \quad (5)$$

where

$$K_0 = K_0^* K' S_0. \quad (6)$$

The relations 3 and 5 are useful to ***calculate the constants of the speeds at which the thermo-chemical processing develop*** depending on the values of the mass

variations or of the cemented layer size variations in time for the products being processed, the same relations in logarithmic coordinates [$\log(\Delta m) - \log t$, respectively $\log\delta - \log t$] represent straight lines with tangents of the of the angles of inclination in relation with the $\log t$ abscissa, themselves equal with the $(1 - \alpha)$. This observation ensures the possibility to determine $(1 - \alpha)$ and K_0^* (or K_0) using very few experimental data related to the size variation of the cemented layer or the mass variation recorded during a certain technological process.

Relation 4 allows determining the ratio between the cemented layer size and its mass variation, $\delta/\Delta m$ a constant for a certain process being analyzed.

The process ***activation energy*** (Eq. (7)) can be calculated using the data related to the thermo-chemical process' ***average speeds***, determined at two temperatures, for the same amount of time.

$$E = \frac{\log W_2 - \log W_1}{\frac{1}{T_1} - \frac{1}{T_2}} \times 4.575 \qquad (7)$$

where E (Kcal/mol)—represents the thermo-chemical process' activation energy; W_1 (mg/cm^2/ora)—process' average speed, determined at temperature T_1, after the period of time t; W_2 (mg/cm^2/ora)—the process' average speed, determined at temperature T_2, after the period of time t;

$$W_t^T = \frac{K_0^*}{(1-\alpha)t^\alpha}; \text{ or } W_t^T = \frac{K_0}{(1-\alpha)t^\alpha} \qquad (8)$$

depending ob requirement the process' average speed can be expressed in mg/cm^2/ora, or in μm/ora.

Unfortunately, the data required for rigorous calculation in order to establish the thermo chemical treatment operations' parameters are almost nonexistent. The separate data from the specialty literature, related to values as ***D*** (***the diffusion coefficient value***), ***h*** (***mass transfer relative coefficient***) ***and K*** (***adsorption speed constant***) need to be verified for each situation taken aside. Knowing these values allows to understand the influence of various technological factors and to gain knowledge about ways to control thermo chemical processes. It is difficult and labor intensive to determine through experiments the values of interest D, h and K. A substantial help in resolving this issue comes from the graphic expressions of the criterial solutions of Fick's differential equations, $\Theta = f(Ti = h\sqrt{D.t};\ x/2\sqrt{D.t})$ and respectively $\Theta = f(h\sqrt{D.t};\ h, x)$ (where $\Theta = C_{x,t} - C_0/C_{\lim} - C_0$ [2, 3].

In order to determine the values of interest D, h and K, one can use the data related to the correlation between the size of the diffusion area and the isothermal maintaining time at the thermo chemical processing temperature, the same data that were used also to estimate the constants of the speeds at which the thermo chemical process develops, its activation energy and its average speeds of development.

In order to determine the values D, h and K related to a certain type of thermo chemical processes, undergoing in rigorously set conditions, it is necessary to go through the following phases; determine the relative concentration Θ; graphic estimation of the time after which the time variation curve of the size of layer enriched with the element transferred through diffusion from the medium (the cementing element), separates form the abscissa (in this application this is time t_1); from the graphic expression of Fick's differential equation solution, obtained by resolving it in grade II limit conditions, $\Theta = f(Ti = h\sqrt{D.t};\ x/2\sqrt{D.t})$ for $x/2\sqrt{D.t};\ = 0$ and the value of the relative concentration Θ previously determined, the value $h\sqrt{D.t} = Ti$ (Tihonov criterion) can be determined; for strictly set thermal processing conditions (temperature and medium conditions) the values D, h and K are constant, thus it can be approximated $Ti_1 = Ti_x\sqrt{\frac{t_1}{t_x}};$ the Tihonov criterion's values, determined after various periods of isothermal maintaining, t_x, along with the value corresponding to the relative concentration Θ, allow to determine the values corresponding to the Biot criterion ($Bi = h.x$) (the graphic expression $\Theta = f(h\sqrt{D.t};\ h.x)$ will be used); the values of the mass transfer relative coefficient, h, will be calculated starting from the graphic determined values for the Biot criterion and respectively the size of the diffusion layers, x, in relation with them; the value of the diffusion coefficient D, will be calculated, taking into account the estimated value of the Tihonov criterion (Ti_1) and the one referring to the mass transfer relative (average) coefficient:

$$D = \left(\frac{Ti_1}{h}\right)\frac{1}{3600.t_1}\ (\text{cm}^2/\text{s}) \qquad (9)$$

the value of the adsorption speed constant will be calculated, K (cm/s)

$$k = h.D \qquad (10)$$

THE CALCULATION OF THE KINETIC PARAMETERS AND THEIR SIGNIFICANCE

Materials and Equipment Used for Experiments

Experimental test intended to gather a minimum of information related to the kinetics of the gaseous nitriding process applied to the pure iron parts (Fe-ARMCO) and respectively to an alloyed steel for improvement intended for nitrding-nitralloy-39MoAlCr15 (0.38% C; 45% Mn; 0.25% Si; 1.4% Cr; 0.20% Mo; 1.1% Al). The nitralloy samples were used in an improved status (quenching 930°C/oil followed by tempering 630°C/oil). he test samples had the dimensions Ø 10 × 15 mm and were subsequently nitrided in ammonia, in a vertical

Table 1. Summary of the pure technical iron nitriding kinetic parameters (using Baram method)
(A) Nitriding conditions: 500°C; $\alpha_{NH_3} = 40\%$

t, ore	$[\Delta m/S_0]$	δ_{exp}	$[\Delta m/S_0]_{calc}$	δ_{calc}	$1 - \alpha$	K_0^*	K_0	W	$E_{500–580°C}$
4	0.89	133.5	–	–		0.235	35.23	33.4	17.0
8	1.46	222.8	–	–		0.245	37.51	27.9	12.0
12	***1.83***	***272.8***	–	–	0.65	***0.236***	***35.28***	***22.7***	***11.6***
20	–	–	*2.56*	*388.3*		$\overline{K_0^*} = 0.238$	$\overline{K_0} = 36.01$	*19.4*	$\overline{E_{\overline{W}}} = 14.1$
30	–	–	*3.34*	*505.4*				*16.8*	

Note: Measuring units: $\Delta m/S_0$ = mg/cm^2; δ-μm; K_0^* = mg/[cm^2 h$^{1-\alpha}$]; K_0 = μm/h$^{1-\alpha}$; $\delta/\Delta m$ = [μm cm^2]/mg; W = μm/h; E = Kcal /mol

(B) Nitriding conditions: 580°C; $\alpha_{NH_3} = 40\%$

t, ore	$[\Delta m/S_0]$	δ_{exp}	$[\Delta m/S_0]_{calc}$	δ_{calc}	$1 - \alpha$	K_0^*	K_0	W
4	2.52	374.5				0.535	79.6	93.7
8	3.06	463.8				0.512	77.7	57.9
12	3.68	553			0.34	0.536	80.6	45.9
20	–		*4.29*	*645.8*		$\overline{K_0^*} = 0.527$	$\overline{K_0} = 79.3$	*32.3*
30	–		*4.92*	*741.3*				*24.7*

muffle furnace, with an useful space of Ø 300 × 600 mm, electrically heated (P = 24 KW).

By choosing two materials, beside verifying the calculation methods for the kinetic parameters, it was intended to determine the effect of the ferrous matrixes alloying on the level of kinetic parameters.

Calculation of the Kinetic Parameters

The experimental data used for the calculation of the kinetic parameters, using the Baram method are stated in Table 1, for pure technical iron, for periods of isothermal maintaining of 4, 8 and 12 ore, at a nitriding temperature of 500°C, respectively 580°C. Using the calculated values of the reaction speeds, K_0^* and K_0 and of the kinetic parameter α, can be anticipated by calculation the size of the nitrided layers, respectively the mass variations of the samples undergoing thermal processing, for any other value of time for isothermal maintaining at the processing temperature.

Therefore:

$$\left(\frac{\Delta m}{S_0}\right)_{calc} = \frac{K_0^* t^{1-\alpha}}{1-\alpha}, \text{ from relation 3} \qquad (11)$$

respectively

$$\delta_{calc} = K_0 t^{1-\alpha}/1 - \alpha, \text{ from relation 5} \qquad (12)$$

where K_0^* and K_0 represent their average values (arithmetic average of the values obtained using experimental data).

The analysis of the data related to the kinetic parameters of the gaseous nitriding process applied to pure technical iron underlines the following aspects:

—at 500°C the nitrogen cementing process develops in the kinetic range, $(1 - \alpha) > 0.5$, therefore the phase of the process that slows its development speed is represented by the reactions on the inter phases separation level;

—at 580°C the development speed of the nitrogen cementing process is limited by the intensity of the diffusion within the metallic matrix, $(1 - \alpha) < 0.5$;

—the nitrided layer growth speeds increase with the increase in nitriding temperature, but they decrease noticeably in time;

—the nitriding process activation energy in the range of temperatures 500–580°C, determined using the average speed of the process, is close to the data existing within the specialty literature related to this value [4, 5].

Following the previously presented succession of calculations necessary to determine the diffusion coefficient, the mass transfer relative coefficient and respectively the adsorption speed constant's value, based on a minimal number of experimental data existing in Table 1, related to the nitriding of pure technical iron, the following values were obtained (Table 2).

The calculated values are in close accordance with the data from the specialty literature related to the nitrogen diffusion in non alloyed ferrite [6].

In case of alloyed matrixes, as for example improvement alloyed steel 39MoAlCr15, the nitrogen diffusion process kinetics in clearly modified, an aspect confirmed by both the experimental data and the corresponding values of the calculated kinetic parameters (Tables 3, 4).

Comparing the results obtained (Table 3) with the ones correspondent to the pure technical iron nitriding

Table 2. Summary of D, h, and K kinetic parameters calculation Nitriding temperature 520°C

t_x, h	$Ti_{\text{calc}} = Ti_1 : \sqrt{\frac{t_1}{tx}}$	X, cm	hx	h, cm^{-1}	$\bar{h}$, cm^{-1}
2	0.140	0.0148	0.10	6.75	
4	0.353	0.0193	0.20	10.36	
6	0.288	0.0238	0.25	10.50	9.60
8	0.250	0.0282	0.30	10.63	
10	0.230	0.0237	0.32	9.78	

$$D = \left(\frac{0.07}{9.60}\right)^2 \frac{1}{3600 \cdot 0.5} = 2.95 \times 10^{-8} \cong 3 \times 10^{-8} \text{ cm}^2/\text{s}$$

$$K = \bar{h} \times D = 9.60 \times 2.95 \times 10^{-8} = 28.3 \times 10^{-8} \text{ cm/s}$$

Table 3. Summary of the 39MoAlCr15 nitralloy nitriding kinetic parameters (using the Baram method)
(A) Nitriding conditions; 500°C; $\alpha_{NH_3} = 40\%$

t, h	$\delta_{\mu m}$, exp	$\delta_{\mu m}$, calc	$1 - \alpha$	K_0, μm/ora$^{\alpha - 1}$	W, μm/h	E, 500–600°C, Kcal/mol
10	200	–		29.98	19.99	9836.3
20	300	–		29.51	14.99	8214.8
30	390	–	0.608	29.98	12.99	8023.7
40	–	458.3		$\overline{K_0} = 29.59$	$\overline{W} = 15.99$	$\overline{E} = 8691.6$
50	–	525				

(B) Nitriding conditions; 600°C; $\alpha_{NH_3} = 40\%$

t, h	$\delta_{\mu m}$, exp	$\delta_{\mu m}$, calc	$1 - \alpha$	K_0, μm/ora$^{\alpha - 1}$	W, μm/h
10	410	–		65.06	41
20	599	–		61.82	27.3
30	700	–	0.487	65.05	23.33
40	–	792		$\overline{K_0} = 63.97$	$\overline{W} = 30.54$
50	–	883			

Table 4. Summary of D, h, and K kinetic parameters calculation $T = 520$°C; $\alpha_{NH_3} = 40\%$

t_x, h	$Ti_{\text{calc}} = Ti_1 : \sqrt{\frac{t_1}{tx}}$	X, cm	hx	h, cm^{-1}	$\bar{h}$, cm^{-1}
10	0.223	0.0251	0.30	11.95	
12	0.204	0.0273	0.40	14.65	14.8
20	0.158	0.0358	0.55	15.36	
30	0.129	0.0456	0.80	17.20	

$$D = \left(\frac{0.07}{14.8}\right)^2 \frac{1}{3600 \cdot 0.5} = 12.43 \times 10^{-9} \cong 1.2 \times 10^{-8} \text{ cm}^2/\text{s}$$

$$K = \bar{h} \times D = 14.8 \times 12.43 \times 10^{-9} = 18.4 \times 10^{-9} \text{ cm/s}$$

(Table 1) it can be noted that in both cases, at low temperatures, the saturation process phase that develops at the slowest speed is the one in the cementing media [$(1 - \alpha) > 0.5$], and that at high temperatures, ≥550°C, the layer forming speed will be hindered by the diffusion processes within the metallic matrix [$(1 - \alpha) < 0.5$]. It can also be observed the diffusion speeds and the reaction speeds' constants in the case of 39MoAlCr15 steel are substantially lower than the ones recorded in the case of pure technical iron nitriding. Implicitly, given the connection between the reaction speed's constant and the process activation energy, a decrease of the reaction speed's constant value will cause an increase of the activation energy.

The information gathered regarding the *D*, *h* and *K* kinetic parameters have a very distinct importance both in theory and in practice: in theory, they certify that by ferrite alloying, the diffusion coefficient decreases (2.5 times compared to the value recorded for pure technical iron nitriding) this in turn causing the increase in the mass transfer relative coefficient, h. The increase of the mass transfer relative coefficient at the same time with a decrease of the diffusion coefficient and a constant value of the adsorption constant leads to the conclusion that in case 39MoAlCr15 steel nitriding the probability of type ε nitrogen rich phases forming on the surface is much greater than in the case of pure technical iron nitriding; in practice, it is necessary to modify the activity of the atmosphere used for nitriding in such way that the process of nitrogen rich phases forming is strictly controlled, thus avoiding the appearance of the networks generated by these phases and therefore the inconveniences related to them. In this context, the specialty literature confirms by practical observations the theoretical reasoning previously presented: an increase in the degree of ammonia dissociation up to 60–65% (even 70% at a temperature towards 600°C) does not have a significant effect on the macro hardness and respectively on the size of the nitrided layer obtained in certain processing conditions (temperature-time) but greatly reduces the tendency of the type ε nitrogen rich phase to appear.

CONCLUSIONS

The kinetic parameters of any thermo chemical process can represent efficient analysis and prognosis instruments for the said processes. It is possible to determine them in an analytical manner using the heterogeneous reactions' kinetics extended equation and using minimum o information related to process kinetics, gathered through experiments. Thus it can be obtained data referring to the phase of the process that develops at the lowest speed (using the kinetic parameter α), the reaction speed constant, process activation energy, layer forming current speed.

The values of the diffusion coefficient, the mass transfer relative coefficient and of the adsorption speed constant can be estimated using the graphic expressions of the criterial solution to Fick's equation, again using minimum o information related to process kinetics, gathered through experiments.

The data referring to the two materials used for study, Fe-ARMCO and 39MOALCR15 are in accordance with the information from the specialty literature and confirm the validity of the analytical methods of calculation for the kinetic parameters, presented in this paper.

REFERENCES

1. Baram, I.I., *Appl. Chem. Mag.*, 1973, no. 4.
2. Popov, A.A., *The Theoretical Basis of Thermo-Chemical Treatment Applied to Steels*, Sverdlovsk, 1962.
3. Tait, N.U., *Steel Heating Technology*, Moscow: Metalurgia Publishing House, 1962.
4. Lahtin, Yu.M., *Physical Basis of Nitriding*, M.: Maşghiz, 1948.
5. Roberts, M.W. and McKee, C.S., *Chemistry of Metal-Gas Interface*, Oxford University Press, 1978.
6. Lahtin, Yu.M. and Kogan Ya.D., *Steel Nitriding*, Moscow: Machine Construction Publishing House, 1976.

ISSN 1068-3755, Surface Engineering and Applied Electrochemistry, 2009, Vol. 45, No. 2, pp. 133–135. © Allerton Press, Inc., 2009.
Original Russian Text © E.M. Makarova, A.V. Khlyustova, A.I. Maksimov, 2009, published in Elektronnaya Obrabotka Materialov, 2009, No. 2, pp. 67–69.

ELECTRICAL PROCESSES IN ENGINEERING AND CHEMISTRY

Diaphragm Discharge Influence on Physical and Chemical Properties of Electrolyte Solutions

E. M. Makarova[a], A. V. Khlyustova[b], and A. I. Maksimov[b]

[a]*Ivanovo State Chemical Technological University, pr. F. Engelsa 7, Ivanovo, 153000 Russia*
[b]*Institute of the Chemistry of Solutions, Russian Academy of Sciences, ul. Akademicheskaya 1, Ivanovo, 153045 Russia*
e-mail: kav@isc-ras.ru

Received October 10, 2008

Abstract—The results of the comparison of estimated (theoretical) and experimental values of electroconductivities in acid, alkali solutions, and tap water subsequent to the action of an underwater low voltage diaphragm discharge have been presented. The experiments showed disagreement between the experimental and estimated values, which suggests a change of the solutions structural characteristics.

DOI: 10.3103/S1068375509020094

INTRODUCTION

In papers devoted to the investigation of electric discharge action upon electrolyte water solutions [1, 2] changes in the acidity and electroconductivity in the solutions have been noted. The solutions' electroconductivity may vary by 1 or 2 orders of value. For the case of glow discharge, such a change can be explained by the nitric oxides' formation in the plasma region and their subsequent dilution in the work electrolyte, which causes acidity changes and, hence, the solutions electroconductivity modification. In the case of an underwater discharge (a diaphragm one in particular), NO_x formation in the plasma region is impossible, because the discharge glows within the electrolyte volume with nitrogen being absent. Previous experiments [3] showed that the diaphragm discharge action on water solutions of acids and alkalis leads to a considerable decrease of the electroconductivity. In [4], design and experimental data were compared concerning the electroconductivity changes under glow discharge conditions. The purpose of the present paper is to obtain similar results for glow discharge. The idea of the approach is the following: if the solution electroconductivity change is stipulated just by the concentration change of H_3O^+ and OH^- ions, i.e., the solution acidity changes at a constant ion mobility, the electroconductivity values being measured should coincide with the designed ones according to the experimental pH values. The observed divergence between them should be interpreted as a consequence of the H_3O^+ and OH^- ions' mobility being changed by the discharge's influence on the solution's structural characteristics.

METHODS OF THE EXPERIMENT

In the experiments, there was used a cell for the diaphragm discharge that is similar to the one described in [3]. Graphite rods of 5 mm diameter served as the electrodes. The operating voltage varied from 200 to 550 V, and the discharge current, from 30 to 250 mA. Tap water solutions were used: HCl (pH = 1.6), HNO_3 (pH = 1.88), H_2SO_4 (pH = 1.851), NaOH (pH = 10). The solution volume made up 400 ml. The diaphragm diameter was 1–1.5 mm.

The acidity was measured using a universal ion meter (*И*-160) every 5 minutes. The electroconductivity was measured simultaneously with the acidity using an ion meter (IonLab).

At the electroconductivity calculation, there was considered the contribution of the solutions' acidity change. The electroconductivity was defined by the formula

$$\chi = c(\mathrm{H})\lambda(\mathrm{H}) + c(\mathrm{OH})\lambda(\mathrm{OH}) + c(K^+)\lambda(K^+) + c(A^-)\lambda(A^-),$$

where c is the concentration, g-equiv/l; and λ is the utmost equivalent electroconductivity (mobility) of the corresponding ion, $\mathrm{Ohm}^{-1}\ \mathrm{cm}^2/(\text{g-equiv})$.

The table presents the reference values of λ of different ions at various temperatures.

Using the reference data on the temperature influence upon the utmost equivalent conductivity, there was made an allowance for the estimated temperature of the general electroconductivity of the solutions.

Table

T°C	Na^+	H^+	OH^-	Cl^-	NO_3^-	SO_4^{2-}
18	42.18	315	171	66.0	62.3	68.4
35	61.54	397	–	92.21	–	–
45	73.73	441.4	–	108.92	–	–
55	86.88	483.1	–	126.4	–	–
100	145	630	450	212	195	260

RESULTS AND DISCUSSION

Figure 1 depicts the estimated (index "a") and measured (index "b") values of the electroconductivity for the tap water (curve 1a and 1b) and the NaOH solution (curve 2a and 2b). In the tap water, the measured electroconductivity values are situated a bit lower versus the estimated ones. Whereas, for the NaOH solution, the data divergence is far beyond the error limits of the experiment.

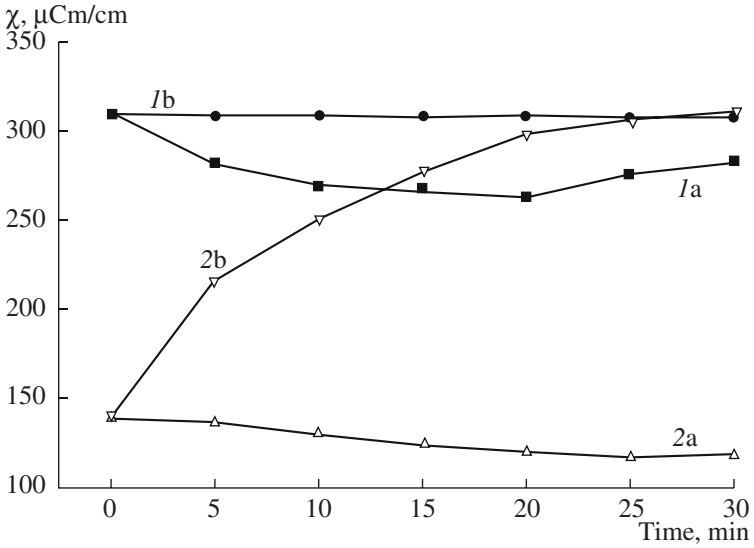

Fig. 1. Comparison of the estimated (index "a") and experimental (index "b") values of the specific electroconductivity change under the diaphragm discharge action. *1*—tap water; *2*—NaOH (pH=10).

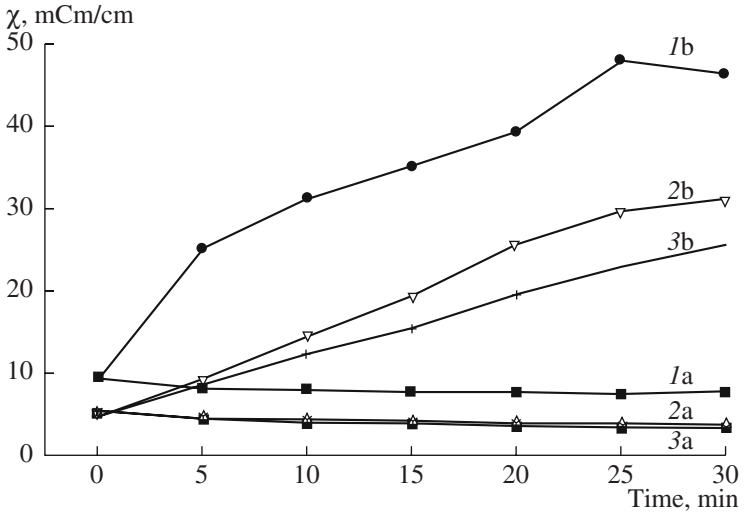

Fig. 2. Curves of the estimated (index "a") and experimental (index "b") values of the specific electroconductivity of acids: *1*—HCl; *2*—HNO_3; *3*—H_2SO_4 (pH 1).

The data obtained for the acid solutions (Fig. 2) are of a similar kind of character. Therefore, the largest distinctions in the estimated and measured values of the specific electroconductivities for the acids and alkali are assumed to be a regularity and are interrelated with the change of the solution structure resulting from the diaphragm discharge action, which mainly affects the hydroxonium ions mobility, the motion mechanism of which is of a relay character [6]. There has been supposed the disconnection of hydrogen bonds occurring due to the diaphragm discharge action, which primarily influences the H- and OH- ions mobility.

REFERENCES

1. Brisset, J.L., Lelive, J., Doubla, A., and Amouroux, J., Interactions with Aqueous Solutuions of the Air Corona Products, *Revue Phys. Appl.*, 1990, vol. 25, no. 6, pp. 535–543 .
2. Kutepov, A.M., Zakharov, A.G., and Maksimov, A.I., Problems and Perspectives of Investigations of Plasma Activated Technological Processes, *Dokl. Akad. Nauk,* 1997, vol. 357, no. 6, p. 782.
3. Maksimov, A.I. and Stroikova, I.K., Comparison of Glowing and Diaphragm Discharge Actions in Aqueous Solutions, *Elektron. Obrab. Mater.*, 2003, no. 1, p. 52.
4. Khlyustova, A.V., Zamaeva, T.V., and Maksimov, A.I., Peculiarities of Electroconductivity Change in Acid and Alkali Solutions under Glowing Discharge Action, *Surf. Eng. Appl. Electrochem.*, 2007, no. 6, p. 72.
5. *Spravochnik khimika. T. 3. Khimicheskoe ravnovesie i kinetika. Svoistva rastvorov. Elektrodnye protsessy* (A Handbook of a Chemist. Vol. 3. Chemical Equilibrium and Kinetics. Solutions Properties. Electrode Processes) Moscow; Leningrad: Khimiya, 1964.
6. Robinson, P. and Stoks, P., *Rastvory Elecktrolitov* (Electrolyte Solutions), Moscow: Izd. Inostr. Liter., 1963.

ISSN 1068-3755, Surface Engineering and Applied Electrochemistry, 2009, Vol. 45, No. 2, pp. 136–139. © Allerton Press, Inc., 2009.
Original Russian Text © M.A. Ramazanov, S.J. Kerimli, S.A. Abasov, R.Z. Sadykhov, 2009, published in Elektronnaya Obrabotka Materialov, 2009, No. 2, pp. 70–73.

ELECTRICAL PROCESSES IN ENGINEERING AND CHEMISTRY

The Crystallization Mode Influence and Magnetic Field Action upon the Mechanical and Thermal Properties of Composite Materials on the Basis of Polymers and Magnetic Additives

M. A. Ramazanov[a], S. J. Kerimli[b], S. A. Abasov[b], and R. Z. Sadykhov[b]

[a]*Baku State University, ul. Z. Khalilov 23, Baku, AZ-1148 Azerbaijan*

[b]*Institute of Physics, National Academy of Sciences of Azerbaijan, pr. G. Dzhavid 33, Baku, AZ-1143 Azerbaijan*

e-mail: mamed-r50@mail.ru

Received October 22, 2008

Abstract—The results of investigations of the temperature-time mode of the crystallization influence and magnetic field action upon the mechanic strength, magnetic permeability, and thermal properties of composites on the basis of polymers (PEHD, PVDF) and the magnetic additive $BaO(Fe_2O_3)_6$ have been presented. It has been shown that the changes of the mechanical strength, magnetic permeability, and the thermal properties of the magnetic composites being studied, with regard to the temperature-time mode of crystallization and processing in a strong constant magnetic field, can be interrelated with the change of the polymer matrix supermolecular structure, the degree of the phase interaction, and the interphase layer thickness.

DOI: 10.3103/S1068375509020100

INTRODUCTION

Recently, the compositions on the basis of polymers and ferromagnetics have been widely used in radio engineering, television, communication engineering, storage devices, and computer engineering due to their relatively high magnetic and exploitation properties. It is evident that, in the process of exploitation in the devices, the elements of polymer-ferromagnetic compositions are exposed to the long-term action of constant and alternating magnetic fields. The processing of magnetic polymer compositions under the influence of constant and alternating fields, as well as the change of the temperature-time regime of crystallization, may vary their magnetic, strength, and thermal properties. The processing of polymer magnetic compositions may improve the magnetic properties of ferromagnetics [1], and it can be used for the structure modification [2]. A constant magnetic field can induce the polymer chains approach and orientation and influence the per-molecular structures of polymers. In [3, 4], it is shown that the dielectric losses in the glass-transition temperature region become reduced under the magnetic field influence—the $\tan\delta$ maximum shifts into the high temperatures region. It has been determined that the orientational effects in polymers are mainly caused by the conformational transformations.

In unprocessed polymer composition materials, the particles of ferromagnetic stuff sustain isotropic distribution, and, after the direct magnetic field action, they are polarized. As a result, they change their space distribution within the polymer volume and shape like chains. The stability of the anisotropic distribution depends upon the residual magnetization of the compositions and the mobility of the polymer matrix.

EXPERIMENTAL METHODS

The influence of the crystallization regimes and the magnetic field action on the strength, magnetic, and thermal properties of compositions of the polymer (PEHD, PVDF) baric hexaferrit ($BaO(Fe_2O_3)_6$ has been examined. The thermal properties of the compositions have been studied by the differentially-thermal (DTA), differentially-thermogravimetric (DTG), and thermogravimetric (TG) methods with a Q-derivatograph of the MOM firm (Hungary) in the temperature region of 20–450°C. The channel sensitivity made up the following: DTA-1/5; DTG-1/15; TG- mg 200 [5].

The initial polymers PEHD and PVDF (without the additive) and the polymer–magnetic composite materials on the basis of PEHD, PVDF, and the magnetic additive $BaO(Fe_2O_3)_6$ were obtained by the method of hot pressing at a pressure of 15MPa at a temperature of the polymer matrix melting for 10 min with subsequent cooling in the following modes of crystallization: (1) The specimens were immersed into a vessel with liquid nitrogen. We call this kind of regime "nitrogen hardening" (NH). (2) The specimens were cooled in a mixture of ice with water at a rate of 2000 degrees/min. This type of regime is called a "melt-quench" regime (MQ). (3) Slow cooling (SC) of the melt up to room temperature at a rate of 2 degrees/min.

All the composition specimens were produced in the form of a film, and the compositions' magnetic proper-

ties were defined at a temperature of 293K. The strength characteristics of the compositions being studied were measured at a temperature of 293K according to [6].

The magnetization was measured by the Domenicalli method with a pendulum magnetometer at room temperature.

RESULTS AND DISCUSSION

Figure 1 displays the dependencies of the mechanical strength (σ) of the compositions PEHD + ($BaO(Fe_2O_3)_6$) and PVDF + ($BaO(Fe_2O_3)_6$), obtained in the MQ regime upon the volume content of the magnetic additive prior to and after the direct magnetic field processing at 2.4 kOe for 0.5 hours. As follows from Figure 1, the mechanical strength σ reduces with the magnetic stuff content increase (and, correspondingly, with the polymer matrix content decrease). Such kind of σ dependency upon the volume content of the magnetic additive is connected with the increase of the specific surface area of the magnetic stuff and the decrease of the share of the composition of the polymer matrix, since the polymer matrix serves a connecting link.

Figure 1 also shows that the constant magnetic field action causes the diminution of the mechanical strength of the composition. The degree of PVDF σ diminution is greater than that of the PEHD one.

The mechanical strength alteration after the compositions processing in the constant magnetic field is interrelated, in our opinion, with the magnetic particle polarization, which leads to the structural disorder (macromolecular excitation, local polarization) of the structure. The mechanical strength change with regard to the polymer matrix and with similar kinds of magnetic stuff is obviously connected with the decrease of the interaction between the neighboring molecules of the polymer matrix and the phase interaction. It is also possible that the constant magnetic field of the polymer molecule may partially orientate itself, which leads to a decrease of the potential barrier and to the decrease of the composition's mechanical strength.

Figure 2 shows the dependence of the magnetic permeability on the volume content of the magnetic stuff for the compositions of PVDF + ($BaO(Fe_2O_3)_6$ and PEHD + ($BaO(Fe_2O_3)_6$ obtained in the MQ regime.

It can be seen from the figure that, with the growth of the magnetic stuff volume content, an increase of μ is observed, with the μ value being dependent on the polymer matrix nature at the given volume content of the stuff.

Figure 3 depicts the MQ and SC mechanical strength dependences of the PVDF + ($BaO(Fe_2O_3)_6$) compositions upon the volume content of the ($BaO(Fe_2O_3)_6$) magnetic additive. It is clear that a σ decrease is observed with respect to the volume content. It is also evident that, with all the other factors being equal, the mechanical strength of the (MQ) com-

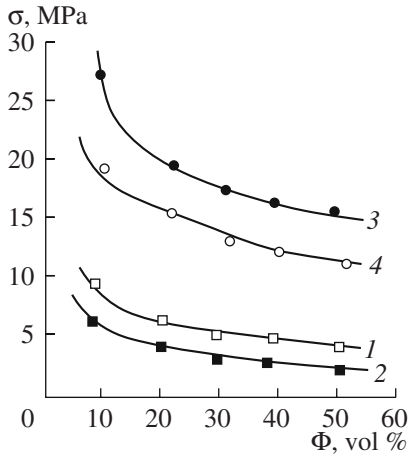

Fig. 1. Dependence of the magnetic strength upon the volume content of the magnetic stuff prior to and after processing in the direct magnetic field: (*1*) PEHD + ($BaO(Fe_2O_3)_6$ – prior to processing; (*2*) PEHD + ($BaO(Fe_2O_3)_6$) – after processing; (*3*) PVDF + ($BaO(Fe_2O_3)_6$) – prior to processing; 4. PVDF + ($BaO(Fe_2O_3)_6$) – after processing.

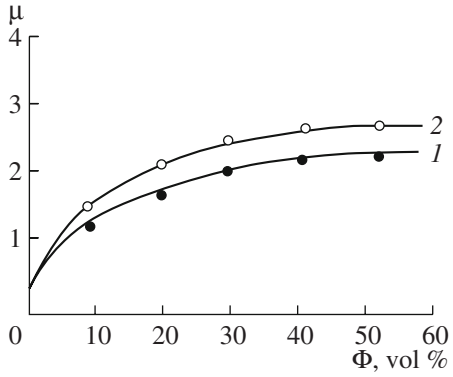

Fig. 2. Dependence of the magnetic permeability upon the volume content of magnetic stuff: (*1*) PEHD + $BaO(Fe_2O_3)_6$; (*2*) PVDF + $BaO(Fe_2O_3)_6$.

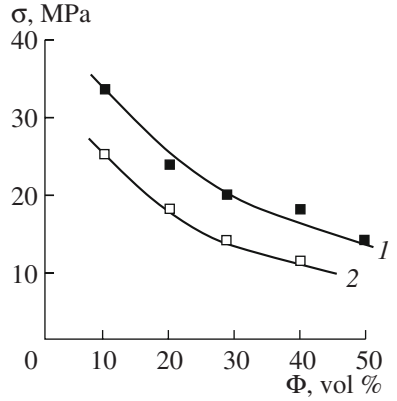

Fig. 3. Dependence of the mechanical strength of the MQ (*1*) and SC (*2*) compositions of PVDF+($BaO(Fe_2O_3)_6$) upon the volume content of the $BaO(Fe_2O_3)_6$.

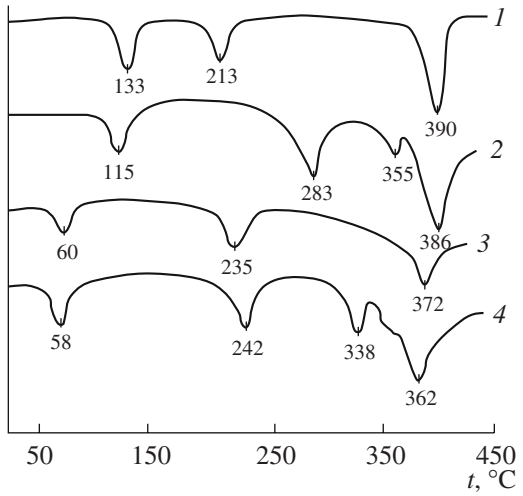

Fig. 4. DTA curves of mixtures of the specimens of the PEHD + $BaO(Fe_2O_3)_6$ system obtained in the NH regime: (*1*) PEHD (initial); (*2*) 90 vol % PEHD + 10 vol % $BaO(Fe_2O_3)_6$; (*3*) PEHD (after proc.); (*4*) 90 vol % PEHD + 10 vol % $BaO(Fe_2O_3)_6$ (after proc.).

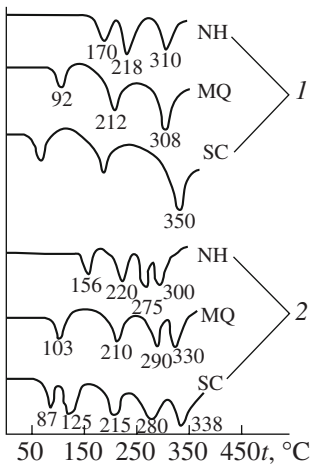

Fig. 5. DTA curves in accordance with the crystallization regime: (*1*) PVDF (initial); (*2*) 90 vol % PVDF + 10 vol % $BaO(Fe_2O_3)_6$.

positions is higher in comparison with the σ of the (SC) compositions.

From the above experimental data, it follows that the mechanical strength of the magnetic compositions is influenced by the polymer matrix polarity, the temperature regime of the crystallization, and the processing under the constant magnetic field.

Figure 4 displays the magnetic field influence on the thermostability of the PEHD and the PEHD–$BaO(Fe_2O_3)$ compositions obtained by NH prior to and after the magnetic field action. It is evident from the figure that, on the DTA PEHD curve, the endothermal effects are observed (Fig. 4, curve *1*) at 133, 213, and 390°C. The endoeffect at 133°C corresponds to melting of the polymer matrix crystalline part of the PEHD. The endoeffect at 213°C corresponds to opening of the weak bonds, and, at 390°C, to the PEHD depolymerization. The endoeffect temperature at 133°C with the additive PEHD + 10 vol % $BaO(Fe_2O_3)_6$ (Fig. 4, curve *2*) shifts towards the low temperatures and becomes 125°C, and this corresponds to melting of the composition with 90 vol % PEHD + 10 vol % $BaO(Fe_2O_3)_6$. The temperature of the weak bonds opening corresponds to 283°C.

From all that was mentioned above, it follows that the change in the temperatures of the thermal effects suggests the formation of a new interphase layer on the interface between the composites' components.

Under the magnetic field influence upon the PEHD and the composite 90 vol % PEHD + 10 vol % $BaO(Fe_2O_3)_6$, it was found that the temperatures of the weak bonds opening shifts towards high temperatures, and the temperature of depolymerization shifts towards low temperatures.

Similar investigations were carried out both for the initial PVDF polymer and the PVDF + $BaO(Fe_2O_3)_6$ composite.

At a rapid crystallization in the NH regime, in the PVDF films, there are observed (Fig. 5, curves *1*) a relatively high melting temperature of the PVDF crystalline part (170°C) and a high temperature of the weak bonds opening (218°C) as compared with the specimens obtained in the MQ and SC regimes. However, the specimens of the composition 90 vol % PVDF + 10 vol % $BaO(Fe_2O_3)_6$, obtained in the MQ (338°C) regime (Fig. 5, curves *2*) are more thermal stable in comparison with those produced by NH (300°C) and MQ (330°C); i.e., the temperature of depolymerization for the specimens obtained in the SC regimes is higher than for the samples obtained in the NH and MQ regimes.

CONCLUSIONS

The change of the mechanical strength, the magnetic permeability, and the thermal properties of the investigated magnetic compositions on the basis of PEHD + $BaO(Fe_2O_3)_6$ and PVDF + $BaO(Fe_2O_3)_6$ with regard to the temperature-time mode of crystallization can be stipulated by the alteration of the per-molecular structure of the polymer matrix and the degree of the phase interaction and the thickness of the boundary layer. The change of the mechanical strength, the magnetic permeability, and the thermal properties of the compositions after being processed in the constant magnetic field, in our opinion, is connected with the magnetic particle polarization, which causes structural disorder (macromolecular excitation, local polarization). It is also possible that the direct magnetic field of the polymer molecule may partially orientate itself,

which leads to a decrease of the potential barrier of the shift and to the decrease of the value of the composition's mechanical strength.

REFERENCES

1. Smirnov, B.I., *Dislokatsionnaya struktura i uprochnenie kristallov* (Dislocation Structure and Crystals Hardening), Leningrad: Nauka, 1981.
2. Polivanov, K.M., *Ferromagnetiki* (Ferromagnetics), Moscow-Leningrad:Gosenergoizdat, 1957.
3. Stankevitch, V.M., Smirnov, V.V., Pleskachevsky, Yu.M., and Yankova, G.E., Study of Interphase Phenomena in Filled High-Density Polyethylene by Electron Spin Resonance Method, *English Summaries*, 2000, vol. 5, no. 1, pp. 28–31.
4. Di W-h, Shang G., Jhao, J.D., and Reng, Y., Ethylene – (Vinyl Acetate) Copolymer Carbon Biber Conductive Interaction on its Electrical Properties, *Polymer International*, 2004, vol. 53, no. 4, pp. 449–454.
5. Gorshkov, V.S., Timashev, V.V., and Savel'ev, V.G., *Metody fiziko-khimicheskogo analiza vyazhushchikh veshchestv* (Methods of Physical and Chemical Analysis of Viscous Substances), Moscow: Vysshaya Shkola, 1981, pp. 37–42.
6. Abasov, S.A., Ramazanov, M.A., Ibragimova, H.S., and Mustafaev, Z.E., The influence of Preliminary Treatment under the Effect of Electric Field on the Strength Properties of the Composition on the Basis of Polyethylene and Piezoceramics, *Fiz. Khim. Obrab. Mater.*, 2003, no. 5, pp. 87–88.

ISSN 1068-3755, Surface Engineering and Applied Electrochemistry, 2009, Vol. 45, No. 2, pp. 140–144. © Allerton Press, Inc., 2009.

ELECTRICAL PROCESSES
IN ENGINEERING AND CHEMISTRY

Physico-Chemical characterization of Acid-Activated Clay: Its Industrial Application in the Clarification of Vegetable Oils

El Hechi[a,b], O. Ben Amor[b], E. Srasra[a], and F. Zargouni[c]

[a]*Unité matériaux, Technopole Borj Cedria, 95-2050, Hammam Lif, Tunis,*
[b]*Université de Sfax, Faculté des Sciences*
[c]*Université de Tunis, Faculté des Sciences*
e-mail: abderazak_elhechi@yahoo.fr

Received November 11, 2008

Abstract—The physico-chemical characterization of Tunisian bentonitic clays is based on the determination of the mineralogical composition (X-ray diffractions and infrared spectroscopy), chemical analysis, cation exchange capacities and the total surface area. The result given by these techniques show that these samples were smectic clay of beidellitic character. In the other hand, the activation of these clays by hydrochloric acid shows an increase of the specific surface area and favorite the clarification of vegetable oils.

DOI: 10.3103/S1068375509020112

INTRODUCTION

Clays are natural products which can be used in industry' crude or treated' by physical and chemical methods. The application domains of clay are derived from the nature and the structure of mineral' in addition to its physico-chemical properties. Acid treatments of clay consist to modify its structure by changing the properties of surface, porosity and acidity. The results obtained through acid activation vary according to the type of clay used' its nature' the acid concentration' the temperature and the time of treatment [1]. Acid activated clay is widely used in industry as a bleaching and decontaminating agent' adsorbent' catalyst and catalyst support [2, 3].

METHODS

The methods adopted in this study are the following: the chemical analysis of the major elements was carried out by EDTA Complexometric Method [4]; X-ray diffractograms were recorded by a Philips type PW 3710 apparatus; the infrared spectra were recorded by Perkin Elmer 783 Dispersive Spectrometer; the cation exchange capacities ($C.E.C._{Cu\text{-}EDA}$) were determined by the Copper Ethylene Diamine Method [5] and the total surface was determined by Methylene Blue Adsorption [6]. The acid treatment at reflux temperature is achieved with 3N hydrochloric acid [7].

RESULTS

X-Ray Diffraction

X-ray diffractograms (Fig. 1) show the different positions of 001 reflection of smectite, kaolinite and illite. The 001 reflection of smectite appeared at 14.7 Å of the crude samples. After an exchange with sodium, this reflection appeared at 12.24 Å characteristic of Na smectite. Heating the samples at 500°C for 2 hours reduced interlayer spacing to 10 Å. Treatment with ethylene glycol showed a change of a 001 reflection to 17.4 Å. The 001 and 002 reflections of kaolinite appeared respectively at 7.19 and 3.57 Å. These reflections disappeared after heating at 500°C for 2 hours. The reflection at 10 Å characterized a small amount of illite. The mineralogical composition estimated by X-ray diffraction is given in Table 1. After purification, the smectitic fraction was higher than 70% of the total clay fraction with small quantities of illite and kaolinite.

Table 1. Mineralogical composition (%) of clay deposit

Samples	Clay mineral, %			Impurities, %			
	Sm.	Ill.	Kao.	Q.	Ca.	D.	Gy.
Soht crude	45	3	10	17	23	2	–
Sof crude	42	5	13	16	17.5	3.5	3
Soht Na-purified	78	7	15	–	–	–	–
Sof Na-purified	71	11	18	–	–	–	–

Table 2. Chemical analysis of the crude and Na-purified samples (Dt): deficit tetrahedral, (Do): deficit octahedral

Samples	SiO_2	Al_2O_3	Fe_2O_3	MgO	Na_2O	K_2O	CaO	H_2O
Na-Soht	43.96	11.98	7.18	5.25	2.46	0.61	7.08	21
Soht crude	53.12	21.92	5.58	2.12	1.76	0.9	–	14
Soht	$Na_{0.48}K_{0.16}(Si_{7.46}Al_{0.54})(Al_{3.08}Fe_{0.59}Mg_{0.44})O_{22}$							
Na-Sof	46.32	14.57	7.58	5.26	2.73	0.83	5.42	17
Sof crude	55.19	22.02	5.42	2.36	1.59	0.95	–	12
Sof	$Na_{0.42}K_{0.17}(Si_{7.54}Al_{0.46})(Al_{3.08}Fe_{0.56}Mg_{0.48})O_{22}$							

Infrared Spectra

The infrared spectra (Fig. 2) show the absorbance of purified samples at a frequency range of 4000 to 400 cm^{-1} [8].

The vibrating bands at 3658 and 920 cm^{-1} (Al-Al-OH group) were observed on the infrared spectra of the different samples, confirming the presence of dioctahedral smectite [9]. The bands at 3435 and 1636 cm^{-1} indicated the adsorption of water molecule on the clay surface [10]. The (Si–O) structural bands of the clay were confirmed by strong absorption bands in the 1100–1000 cm^{-1} region. The bands at 877, 854 and 800 cm^{-1} corresponded respectively to (Fe,Al–OH), (Mg,Al–OH) and (Mg,Fe–OH) in smectitic clay [11]. The band at 3710 and 714 cm^{-1} indicated the presence of kaolinite.

Chemical Analysis

The chemical weight percent composition of the 2 um fraction (crude samples and purified clay fraction) are in Table 2. The chemical formula may be calculated for these fractions by using Mauguin Method. The number of cations in the octahedral sheet (Al, Fe and Mg) are closer to 4 than to 6. This result confirms that clays are essentially dioctahedral. The chemical composition data indicated the presence of small amounts of impurities in the solid; the majority of Mg and K must be in the composition of the mica, confirmed by the presence of illite and kaolinite in the XRD diffractograms.

Cation exchange capacities and the total surface

The cation exchange capacities ($C.E.C._{Cu\text{-}EDA}$) and total surface (Ts) were measured for the crude and purified samples (Soht and Sof). After purification, the cation exchange capacities and total surface increased distinctly. Results are given in Table 3.

Application in the Bleaching of Oils

Several methods were adopted for the clarification of vegetable oils, but the most used in industry is clay activated by hydrochloric acid. This method consists in the elimination of the pigments by adsorption from oil. For bleaching test 10 g of clay were added to 100 ml of 3 N HCl, heated under reflux conditions, for 20 min. Then, suspensions were centrifuged and solids washed with distilled water until no chloride anions were detected (Ag^+ test) and dried at 75°C. The oil clarification was followed by the measurement of absorbance by oil before and after treatment by clay. The bleaching capacity is given in table 4 and presented in Fig. 3. The formula used to calculate power decolorisation consists to:

$$\frac{A_{430}(C.O.) - A_{430}(T.O.)}{A_{430}(C.O.)}$$

A_{430}: absorbance at 430 nm of crude oil (C.O.) and after treatment with clay (T.O.)

The spectra of natural oil revealed the carotenoid pigment at 430, 455 and 483 nm. Bleaching decrease the intensities of carotenoid pigment until total disappear.

Oils treated with activated clays for 6 hours showed brown coloring of the pigments. In addition, the three maxima at 430, 455 and 483 nm were present in the absorption curves. These results showed that activated clays did not absorb large quantities of pigments. This behavior is explained by an intense destruction of the layers and interlayer space of activated clay. Under these

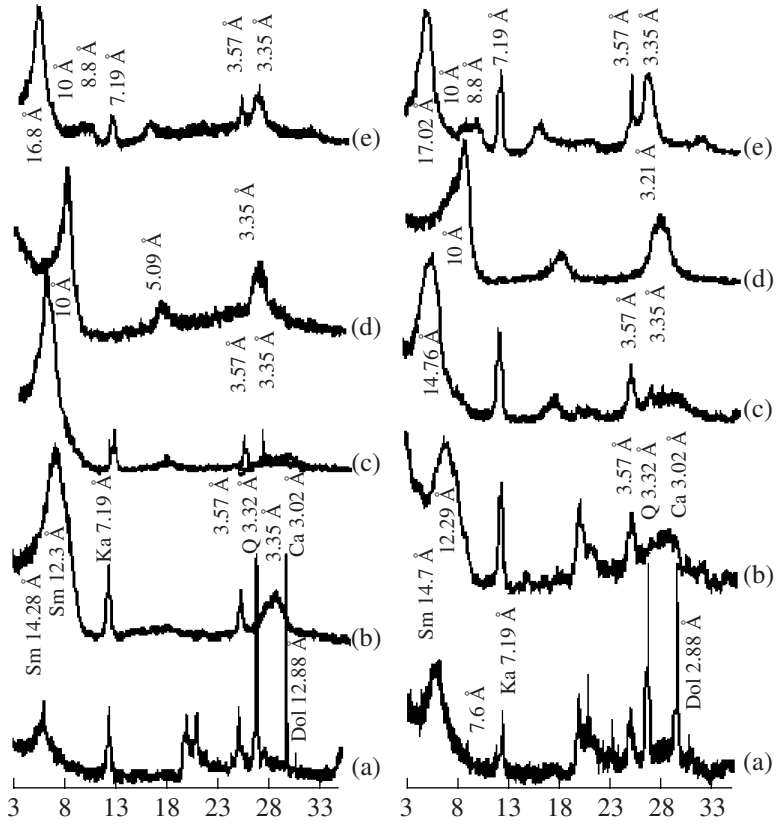

Fig. 1. XRD patterns of some acid activation clays. (a) crude powder; (b) Na exchanged powder; (c) oriented Na exchange film; (d) oriented Na exchange and heated at 500°C film; (e) oriented Na exchange and glycoleted film.

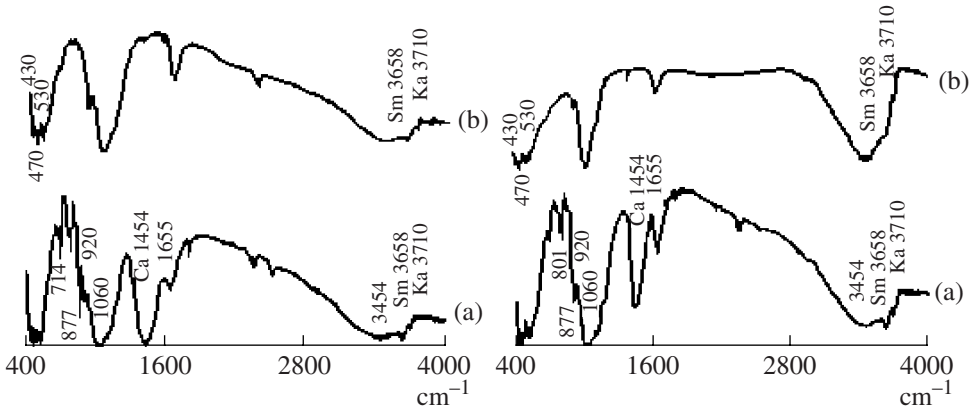

Fig. 2. IR- spectra of Soht and Sof, (a) crude sample and (b) purified sample.

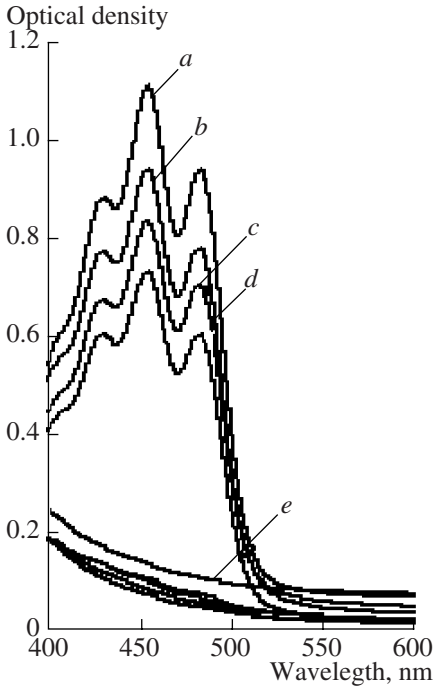

Fig. 3. The absorption spectra of vegetable oil: *a*—crude oil; *b*—treated oils by purified clay; *c*—treated oils by activated clays during 6 hours; *d*—treated oils by decarbonated clay; *e*—treated oils by activated clays during 1–5 hours.

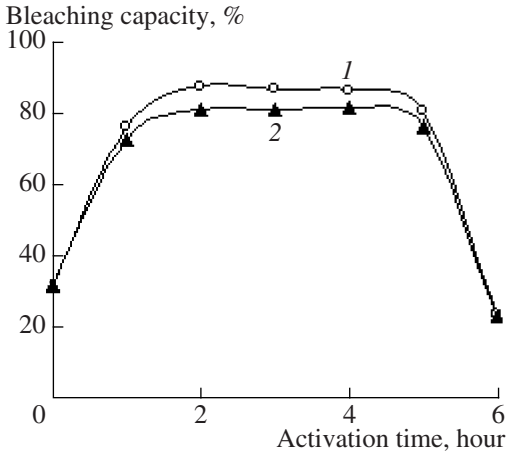

Fig. 4. Bleaching capacity of activated clays at 1–6 hours.

new conditions, clay lost absorption and adsorption characteristics. Consequently, clay lost its bleaching capacity. Oils treated with activated clay during 1–5 hours became clear, and clay eliminated the pigments. The fall of the bleaching capacity curves indicates that clay absorbed the pigments.

The bleaching capacity curves according to the activation time (Fig. 4) show that the weakest bleaching capacities are given by the crude clays, decarbonated and purified clays; on the other hand, the clays activated with hydrochloric acid present satisfactory values which exceed 85%. These curves make it possible to determine a clarification optimum after 2 hours of activation with 3 N hydrochloric acid, which shows the highest values.

CONCLUSIONS

The different analysis of these Tunisian samples shows that the clay fractions are essentially smectitic containing little amounts of illite and kaolinite. The associated minerals are essentially quartz and carbonate. After purification, the smectic fraction is always exceeding 70%.

Table 3. Cation Exchange Capacities (C.E.C. meq/100 g of calcined clay) and surface areas (S.A. m^2/g)

Samples	Crude		Na-Purified	
	C.E.C.	S.A.	C.E.C.	S.A.
Soht	43	408	80	650
Sof	44	464	75	606

Table 4. Bleaching capacity and Cation Exchange Capacities of Crude, Purified and Activated clays

		Bleaching capacity		C.E.C.	
Samples		Soht	Sof	Soht	Sof
Purified		12.45	15.24	80	75
Crude		31.29	31.97	43	44
Activated clays	1h	76.56	72.95	39.3	42.2
	2h	87.79	82.12	28.8	32.6
	3h	86.5	80.97	20.9	26.8
	4h	85.27	80.44	17.5	22.1
	5h	80.45	76.44	15.2	17.3
	6h	23.4	22.87	13	13.2

The treatment of bentonitic clays with 3 N hydrochloric acid shows that once activated, these clays have weak cation exchange capacities. The specific surface which seems the determining factor in the adsorption of the pigments increases and, consequently, the bleaching capacities of these clays become significant. This study makes it possible to determine a clarification optimum of vegetable oils by clay 2 hours after activation by 3 N hydrochloric acid.

REFERENCES

1. Srasra, E., Caractérisation minéralogique, propriété physico-chimique et application des argiles du gise-ment Haidoudi, Thèse de 3eme cycle, *Fac. Sc. Tunis*, 1987, p. 171.
2. Belver, C., Angel Bañnares Munoz, M., and Vicente, M., Chemical Activation of a Kaolinite under Acid and Alkaline Conditions, *Chem. Mater.*, 2002, vol. 14, pp. 2033–2043.
3. Teng, Min-Yu and Lin, Su-Hsia, Removal of Basic Dye from Water onto Pristine and HCl-Activated Montmorillonite in Fixed Beds, *Desalination*, 2006, vol. 194, pp. 156–165.
4. Soljic, Z. and Marjanovic-Krajovan, V., Méthode rapide d'analyse de SiO_2, Fe_2O_3, TiO_2, CaO et MgO dans une bauxite, analyse rapide de calcaire et de dolomite, *Chimie Analytique*, 1968, vol. 50, no. 3, pp. 122–127.
5. Bergaya, F. and Vayer, C.E.C. of Clays : Measurement by Adsorption of a Copper Ethylene Diamine Complex, *Appl. Clay Sci.*, 1997, vol. 12, pp. 275–280.
6. Pham Thi Hang and Brindley, G., Methyléne Blue Adsorption by Clay Minerals, Determination of Surface Areas and Cation Exchange Capacities, *Clays and Clay Minerals*, 1970, vol. 18, pp. 203–212.
7. Srasra, E., Surface Properties of an Activated Bentonite Decolorisation of Rapeseed Oils, *Appl. Clay Sci.*, 1989, vol. 4, pp. 411–421.
8. Beena Tyagi, Chudasama, Chintan D., and Jasra, Raksh V., Determination of Structural Modification in Acid Activated Montmorillonite Clay by FT-IR Spectroscopy, *Spectrochimica Acta, Part A*, 2006, vol. 64, pp. 273–278.
9. Caillere, H., Rautureau, *Minéralogie des argiles*, vol. 1: *tructures et propriétés phisico-chimiques*; vol. 2: *classification et nomenclatures* (2eme Ed.), Masson, p. 189.
10. Srasra, E. and Trabelsi-Ayedi, Physico-Chemical Properties of Tunisien Bentonitic Clays, *Asian J. Chem.,* 2001, vol. 13, no. 4, pp. 1287–1293.
11. Farmer, *The Infrared Spectra of Minerals*, London: Mineralogical Society, 1974.

ISSN 1068-3755, Surface Engineering and Applied Electrochemistry, 2009, Vol. 45, No. 2, pp. 145–152. © Allerton Press, Inc., 2009.
Original Russian Text © Yu.A. Boshnyaga, L.A. Bantysh, 2009, published in Elektronnaya Obrabotka Materialov, 2009, No. 2, pp. 79–88.

ELECTRICAL PROCESSING OF BIOLOGICAL OBJECTS AND FOOD PRODUCTS

Revisiting the Electric Field Sterilizing Action on Fruit Juice Microflora

Yu. A. Boshnyaga[a], L. A. Bantysh[b]

[a]*Institute of Applied Physics, Academy of Sciences of Moldova, ul. Academiei 5, Kishinev, MD-2028 Republic of Moldova*

e-mail: iubosneaga@gmail.com

[b]*Institute of Food Technologies, ul. M.Cogalnicheanu 63, Kishinev, MD-2009 Republic of Moldova*

Received August 11, 2008

Abstract—The practicability of usage of electric pulses to influence the microflora of liquid media is justified. The regime parameters at which it is possible to obtain the nonthermal effect of pasteurization (inactivation of the vegetative microorganism cells in the media) are presented. The minimization of the ohmic heating effect inevitably occurring at current passage through fruit juices is the essence of our propositions. The low-temperature pasteurization effect is verified experimentally.

DOI: 10.3103/S1068375509020124

High technologies of processing and conservation of foodstuffs presuppose the obligatory preservation of the most valuable thermolabile biologically active components including vitamins. Implementation of gentle methods of microbiological security support is of special interest for technologies of the vacuum and sublimation drying of foodstuffs, being intrinsically low-temperature ones.

Yet, for the stage of sterilization and pasteurization, there isn't a real alternative to thermal methods in spite of the apparent vast variety of "cold" sterilization methods: it is difficult to use fine-pored bacterium filters and the sphere of their application is rather limited; the methods of radial sterilization by ionizing radiation, ultrasound, chemical substances, and ultraviolet radiation don't possess selectivity of their influence on microorganisms and destroy in parallel useful substances.

As electric processes underlie living matter and are determinative for any microorganisms, researchers are paying special attention to electric methods of action on liquid media, which are the most promising from the point of view of "cold" pasteurization and sterilization.

It should be noted that the control problems of microorganism development in liquid media are of great interest not only for the food industry but also for pharmacology, the perfume and cosmetic industry, the wine industry, medicine and veterinary medicine, and communal services. For instance, in medicine there is the problem of an electric effect being used in order to destroy pathogenic (carcinogenic) cells in blood. In the wine industry, it is the pasteurization of dry wines that is topical, which allows excluding sulphur dioxide as a preservative. There is also interest in the improvement of water treatment, etc. In all the cases of electric processing, the emphasis is placed on the fact that living cells (unlike noncellular structures) have a defenseless vital area, namely, the cell membrane.

Generalization of the Experience of Electric Actions with Different Frequency on Liquid Media in Order to Achieve a Sterilizing Effect

Electric actions on cells have been a major focus of interest of investigators for many years [1–4].

Placing a product into an electrostatic field (e.g., of a parallel-plate capacitor) is the most simple method of the electric influence on fruit juice microorganisms. However, the electrostatic fields, including high voltage ones, rather weakly effect the liquid media. The presence of a large number of free charges (positive and negative ions) in fruit juices and the high polarization of water (the main component of juices) cause nearly complete neutralization of the external electrostatic field of any really attainable intensity in the product bulk. The displacement of charges in the electrostatic field (with an excess of the same sign charge in the surface layer) doesn't block the metabolic processes in microorganisms in the liquid bulk. Against the backgrounds of the intensive thermal motion of colloid size molecules and particles, the total displacement of the charges remains "unnoticeable." However, the absence of a noticeable response to electrostatic fields is well known for such sensitive and complex organisms as humans and animals (for instance, for birds sitting on high voltage wires). Consequently, noticeable effects shouldn't be expected in the case of application of electrostatic fields (even with maximum intensity) to microorganisms in liquid media.

Another situation occurs at the passage of an electric current of different frequencies through the product–electrolyte contacting with the electrodes.

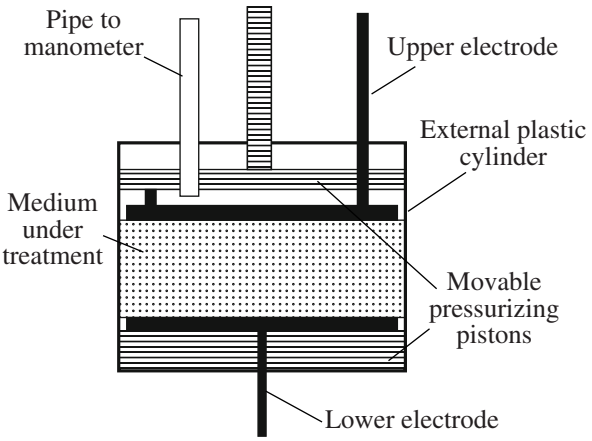

Fig. 1. Cell-applicator for electric processing of cylinder specimens.

Special literature contains references to the use of an alternating industrial-frequency current (ohmic heating) to sterilize liquid media [5].

A set of experiments on fruit juice processing by simple harmonic currents has been carried out to elucidate the specific "nonthermal" action of an industrial-frequency 50 Hz current. The cell–applicator used for electric processing of cylinder specimens is shown in Fig. 1. (A similar cell is hereafter employed to supply high-voltage pulses to the specimens).

The same product volume (1 ml) is subjected to processing in all the experiments. The layer thickness (the interelectrode spacing) is 1 cm, and the magnitudes of the voltage (V) impressed to the cell numerically coincide with the external (outer) electric field voltage impressed to the specimen (V/cm).

The direct electric current and industrial-frequency current passing through the fruit juices and their ohmic heating is observed from the electrolysis products released on the electrodes (the electrolysis is the most active at the direct current and decreases with the growth of the frequency).

The voltage amplitude variations are performed in the range from 50 to 500 volts. The period and on–off time of supplying the sine 50 Hz pulse runs (with the envelope line in the form of a meander wave) are controlled too (Fig. 2).

The switching duration of the sinusoidal vibrations and on–off time is respectively varied in synchronism with the voltage amplitude (by means of the pulse period change) in such a way as to maintain the total treatment process duration and to obtain the same final temperature of the product. The product specimens are quickly cooled to room temperature after the treatment.

No noticeable differences (variations) due to the change of the effective parameters were found after numerous tests: the antibacterial effect remained nearly the same for the given final temperature (independent of the conditions under which it is achieved).

Thus, there is observed a sufficiently strict dependence of the surviving population of microorganisms on the amount of heat liberated in the specimen owing to ohmic heating. This heat amount (under conditions of the negligible heat exchange with the environmental medium) is uniquely determined by the final specimen temperature. The higher the final temperature is, the smaller (up to the failure to detect) the population of yeasts or other microorganisms is. Implicitly, such a result speaks for the absence of any noticeable nonthermal (specific) action of the 50 Hz electric current.

To refine (to additionally correct) these conclusions (concerning the weakness or total absence of the nonthermal action of the industrial-frequency electric current within the examined range of the electric field intensities), there was carried out a set of tests on the heating of specimens up to the prescribed temperatures through conventional (conductive–convective) heating. The final temperature parameters, as well as the process duration, remain the same as in the case of the ohmic heating. No significant benefits (differences) in the final results are found, indicating the accuracy of the above mentioned conclusion.

It should be noted that, even in the absence of the expressed nonthermal effect at the sterilization of liquid media, the ohmic heating by an electric current has a number of important merits as compared with conventional conductive heating. The electrotechnology allows realizing the inertia-free treatment (uniform through the bulk and without the temperature falling) of a thick product, which is impossible with conventional heating. The near-electrode processes occurring at the ohmic heating can be minimized or made beneficial under certain conditions (thanks to the proper selection of the electrode materials and other measures). Besides, the mass-dimensional, sanitary, hygienic, and other

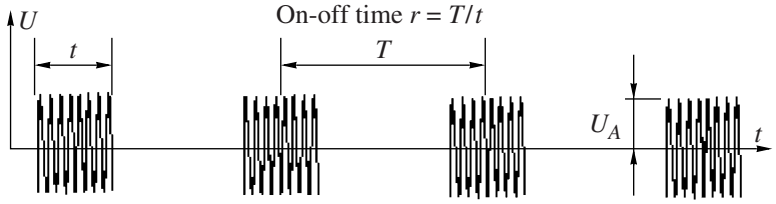

Fig. 2. Parameters controlled at the ohmic heating by industrial-frequency currents, the voltage amplitude (U_A), the pulse duration (t), the pulse period (T), and the total treatment time.

characteristics of the electrotechnology are preferable. It is true that the technology of "ohmic" sterilization by an electric current requires the consumption of high-potential (i.e., relatively expensive) electric power. However, this drawback can be to a great extent neutralized through the heat recuperation.

It is possible to avoid the influence of electrodes (and the electrolysis on them at the same time) by employing super-high frequency electromagnetic oscillations or microwaves to process liquid dielectrics. At a super-high frequency (about ~10^9 Hz = 1 GHz), the physical picture is similar to the above described one for the case of electrostatic fields but with some essential distinction: the polarity (the orientation of the dipoles and free charges) changes with the enormous frequency being the cause of the volume dielectric heating of the medium placed into the SHF field. Consequently, it is logical to use the SHF effect for sterilization. However, numerous experiments with SHF fields [1] (a long-term global experiment employing mobile telephone communication being one of them) showed that SHF band radiation (besides the effects connected with the dielectric heating by powerful radiation) can hardly influence organisms even on an informational level. (The earth's atmosphere is almost transparent for microwaves, and animals are "acquainted" with them since the moment of their birth. No wonder living organisms possess "immunities" to weak accidental SHF signals coming from space. Some other situation is observed for the millimeter and submillimeter bands strongly absorbed by the atmosphere: a certain self-descriptiveness in complex biological media is proved for them, mainly, as subject to the resonant action of weak electromagnetic radiation on water.) The experiments on the action of super-high frequencies on microflora (including that of liquid media) show that there isn't any expressed specific (nonthermal, resonant, or any other) effect of microwaves on microorganisms. The absence of noticeable specific (nonthermal) effects at SHF can also be explained by the smallness of the SHF-radiation quantum if the quantum approach is applied (for instance, at a frequency of $f = 3$ GHz, the microwave quantum energy is only $E \sim 10^{-5}$ eV). The "softness" and uniformity of the microwave thermal treatment favor the survivability of microorganisms [1]. (It should be noted that SHF gas plasma of a certain composition possesses a unique sterilizing ability but has nothing to do with the formulated problem).

The volume character is the advantage of the microwave heating noticeable in a sufficiently strong SHF field. It can be successively used for the common thermal sterilization of any dielectrics (solid and liquid ones). At the SHF heating, the electrodes have no influence on the product, as their contact with the medium under heating is not necessary.

Thus, the "conventional" methods of electric actions don't allow one to expect a sizeable nonthermal effect of sterilization.

Table 1. Specific resistances of model liquid media at room temperature (20°C)

Conducting medium	Specific resistance, $\Omega \times m$
Distilled water	10^3–10^4
River (town) water	10^1–10^2
Fruit juices	2–8
Sea water	0.3

Substantiation of the Advisability of the Application of High-Voltage Pulses for Pasteurization

The substantiation of the regimes under which it is possible to obtain the nonthermal effect at an electric action on liquid media with the aim of pasteurization (inactivation of the existing vegetative cells of microorganisms) is presented below. Minimization of the ohmic heating effect occurring inevitably at the current passage through the fruit juices is the focus of the proposition.

Fruit juices are in this work the subject of investigation of electric actions with the aim of pasteurization. They are aqueous electrolytes with various inclusions of usually colloidal size. In the framework of the problem under consideration, the most interesting among these inclusions is the behavior of yeast cells and molds, which damage fruit juices. The result of the electric action is determined by its parameters, as well as by the specific conductivity and other properties of the medium under treatment (including the microorganisms). The conductivity of the electrolyte medium depends mainly on the concentration of moving ions of opposite signs. It is possible to get an indication of the order of magnitude of the fruit juice's specific resistance on the basis of evaluation of reference data (Table 1). The specific resistance of fruit juices greatly depends on the concentration of ion-generating components and approaches that of sea water.

The temperature raising the resistivity of the fruit juices reduces in a linear fashion (caused mainly by the growth of the dissociation degree, as well as the damage of salvation shells). The damage of the microorganism vegetative cell structure (being the purpose of the action under examination) also promotes the decrease of the fruit juice's resistivity, but the separation (identification) of this component of the medium conductivity growth is an individual task.

It is reasonable to carry out the product processing using a parallel-plate capacitor whose conducting plates (metal or graphite ones) make contact with the fluid. The parallel-plate capacitor field uniformity allows expecting the corresponding uniformity (across the bulk) of the liquid product treatment.

The processes on the electrodes contacting with the liquid medium (the formation of a double electric layer and electrolysis) are decisive at low frequencies and direct current (unlike super-high frequencies).

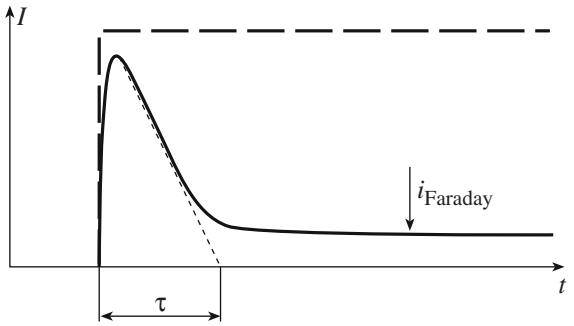

Fig. 3. The shape of the current through the cell with a staircase voltage being supplied to it.

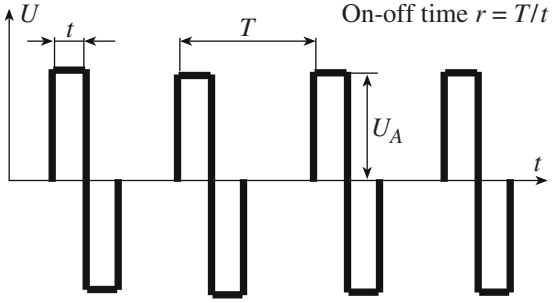

Fig. 4. High-voltage pulse controlled parameters (the pulse voltage amplitude, the pulse duration, the pulse period, and the total treatment time).

The total voltage on the cell (parallel-plate capacitor) may be presented in the following way:

$$U = \varphi_e^a + \varphi_e^c + \eta_a(i) + \eta_c(i) + I \times R, \quad (1)$$

where φ_e^a and φ_e^c are the equilibrium potentials of the anode and cathode, respectively (they are determined by the electrochemical properties of the electrode–solution pair and are settled at the presence of the electrode–solution contact); $\eta_a(i)$ and $\eta_c(i)$ are the overvoltage potentials on the anode and cathode, respectively; and $I \times R$ is the voltage drop in the volume of the medium under treatment.

The constituents of the right part of equation (1), excluding the equilibrium potentials, are interdependent. The voltage being supplied to the cell electrodes flows in the circuit (Fig. 3). The capacitive current, having the greatest magnitude at the moment of the voltage switching on, reduces as the double electric layer is charged (formed) with the time constant $\tau \sim RC$, where R is the specific electric resistance to the current of the double electric layer charging, and C is the DEL specific electric capacity. The value of the specific (for 1 cm^2 of the electrode area) electric capacity C of the double electric layer can be estimated with the known formula for the parallel-plate capacitor capacity:

$$C = \varepsilon_0 S/d = 0.885 \times 10^{-11}\text{F/m} \times 10^{-4}\text{m}^2/10^{-9}m = 10^{-6}F = \mu\text{F}. \quad (2)$$

Thus, the estimation gives a rather significant value of the DEL specific electric capacity of several microfarads: $C \sim n \times 1$ μF/cm^2 being realistic enough. (For example, it is possible to measure the double electric layer capacity by means of the alternating current bridge, but it is beyond the scope of the problems of this work). The double electric layer capacity may have a considerably greater value under the special conditions being widely used at present when designing modern high-capacity capacitors ("supercapacitors") [6].

Usually, the DEL formation time constant τ is equal to fractions of a millisecond [7]. This means that, with a unipolar pulse with a duration of less than 1 millisecond (or alternating polarity pulses with a frequency of more than 1 kHz) being supplied to the cell, the current of the double electric layer formation is prevailing at the minimum faraday current of the electrolysis.

The growth of the effective faraday electrolysis current, forming a close circuit, occurs with phase delay in relation to the reactive current of the double electric layer charging. In this case, on the cathode, there takes place the reduction of ions or molecules from the solution due to their absorption of the electrons from the cathode (for example, by cations: $2H^+ + 2e^- = H_2$), and, on the anode, there takes place the oxidation of ions or molecules due to the transfer of electrons to the anode (for example, by anions: $4OH^- = 4e^- + 2H_2O + O_2$). The mentioned electrolysis of water (the main component of fruit juices) is the most harmless process observed on the electrodes. Yet it is necessary to take into account the processes of reduction of ions (e.g., of iron as a result remaining in the solution ($Fe^{3+} + e^- = Fe^{2+}$) or of copper depositing on the cathode from the solution ($Cu^{2+} + 2e^- = Cu$) occurring on the cathode, as well as the processes of oxidation of ions and molecules in the electrolyte or making up the anode material (e.g., the copper anode dissolution: $Cu = Cu^{2+} + 2e^-$). If the above mentioned anode dissolution process is relatively easily blocked by application of inert materials to make the anode (graphite, oxides of some metals, platinum), the other processes effecting the treated medium composition and being peculiar for the electrolysis process are rather difficult to neutralize.

As follows from the previous presentation, it is possible to reduce the electrolysis effect due to the growth of the alternating voltage frequency (or the pulse duration shortening when a unipolar pulse is used). To sterilize the liquid medium (with the action on the microorganisms in the liquid bulk being the purpose and the near-electrode electrolysis processes being harmful secondary ones transforming a part of the electric energy into heat and changing the juice composition), it is reasonable to employ short enough pulses with changed polarity, steep leading edges, and maximum amplitude. There can be consciously given breaks between the packets of these pulses (see the example in Fig. 4, pairs of heteropolar pulses following each other

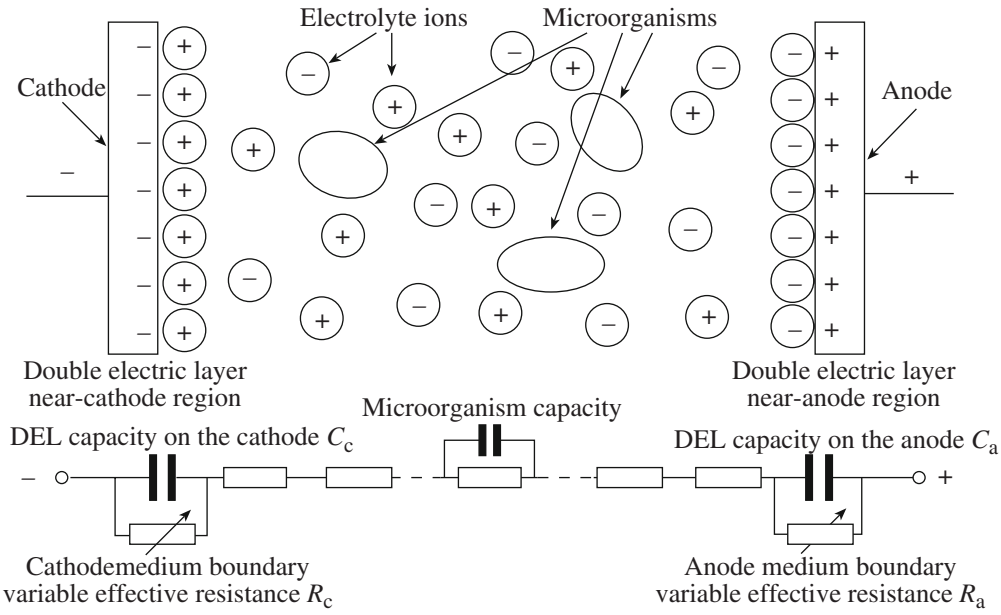

Fig. 5. Distribution of charges on the cell (corresponding to the formed DEL) and the cell equivalent electric circuit.

with a certain on–off time). The changed polarity pulses are preferable as they favor the electrolysis reverse flowing (meaning liquidation of the unwanted products generated during the electrolysis) with the change of the voltage $I \times R$ (and, respectively, the capacitive current passing through the liquid product bulk) growing simultaneously.

It should be noted that the above described method of electrolysis avoidance has been *de facto* approved for radiofrequency electrosurgery: diathermal installations (radiothoms) operate on a frequency of over 100 kHz (in actual practice, it is 300 kHz to 5 MHz), because a lower frequency causes noticeable electrolysis in the muscle and nerve-ending cells showing up as stimulation and jerks. Naturally, at the electrosurgical interface, suitable high frequencies are chosen to avoid these unwanted and extremely dangerous effects.

The pulse voltage amplitude U_A should be selected as the maximally achievable at the verge of avalanche-type breakdowns (in the external circuit or in the liquid) permitting one to hope for poration (breakdown, damage) of the microorganism cell membrane: a great value of the voltage drop $I \times R$ in general on the cell means, at the same time, a rise of the voltage drop on any microobject in the liquid bulk, including the vegetative cell membranes of microorganisms.

The above mentioned recommendations are illustrated by Fig. 5, where the processes in the cell and the equivalent cell electric circuit are jointly presented. Ohm's law validity in the examined circuit is beyond question in spite of the presence of discontinuities (bias currents) on the capacitors as the currents in the circuit continue to be quasi-steady because the bias currents group together only between the capacitor "plates." The product bulk effective resistance is shown as a distributive one with the resistance being shunted by the cell electric capacity at the locations of microorganisms. The yeast cells used in the experiments comprised oval (egg-shaped) structures 8–10 μm in length bounded by plasma membranes with selective permeability. When the electric pulse amplitude and steepness are sufficiently large, the unicell membrane breakdown (poration) is possible. The electrode-medium boundary effective resistance (R_c and R_a, respectively, on the cathode and the anode) grows from near zero at the moment of the pulse supply up to the relatively large constant steady value after the double layer capacitor charging is finished (in this case, almost the total voltage supplied to the cell drops near the electrodes). The maximal steepness of the pulse's leading and back edges is a mandatory requirement for the thermal effect (ohmic heating) minimization in the medium under treatment. It is reasonable to compare the potential effect of such steep pulses with the action of harmonic (sinusoidal) industrial-frequency currents: the "mild" regime of the gradual variation of 50 Hz oscillation frequency voltage is much more suitable for the survival of living cells than the supply of great amplitude "shock" pulses.

The optimum pulse duration t (see Fig. 4) can be found owing to the analysis of the shape of the current through the cell when a staircase voltage is supplied to it (Fig. 3). As was mentioned above, the double electric layer charging time constant is $\tau \sim 10^{-4}$ seconds or ~100 μs. It is during the capacitive current charging period that the "losses" due to the near-electrode electrolysis are minimal with the current and voltage drop being maximal in the specimen bulk. However, the

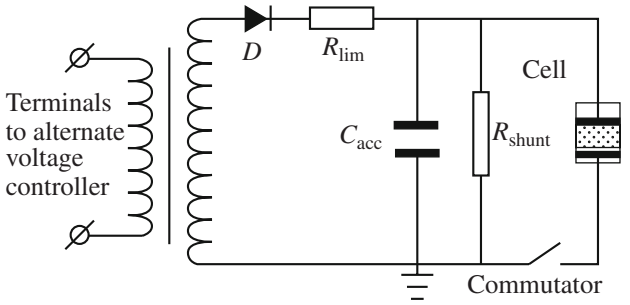

Fig. 6. Electric circuit of the cell applicator switching to the unipolar pulse generator.

value $t_{opt} \sim 100$ μs is an evaluated one, which should be adjusted (determined) experimentally.

It is evidently reasonable to determine the optimal pulse-repetition period T, as well as the total treatment time, experimentally, as they depend on the physiological features of specific microorganisms.

The Experimental Search for Regimes of Fruit Juice Pasteurization by High-Voltage Electric Pulses

It is worth noting the increased number of works concerning the implementation of high-voltage pulses to affect biological cells [8–16].

Due to the great variety of cell forms and the many controlled parameters, the influence mechanism isn't completely clear yet; that's why the results reported by different authors are so ambiguous and further investigations are necessary.

The electric circuit used in the experiments on the product (apple juice) processing by high-voltage unipolar pulses is presented in Fig. 6 (the design of the cell applicator for cylinder specimen electric treatment is shown in Fig. 1). It allows one to control the voltage supplied to the applicator in the range from 0 to 6500 volts. As was proved above, a pulse amplitude rise with steep leading and back edges increases the probability of vegetative microorganism cell damage. A larger voltage on the cell (and, respectively, the electric field intensity in the medium under treatment) could be achieved in practice, but the installation becomes somewhat more complicated (it is possible to increase the electric field intensity as well as to improve the pulse shape in future experiments). Yet, with the electric field intensity in the medium being even $E = 5$ kV/cm in the capacitive current regime, the voltage drop on the microorganisms (their average evaluated size is about 10 μm) comprises 5 volts, substantially exceeding the natural potential difference on the cell membrane (it is not more than 100 mV; the membrane internal side at rest is charged negatively and the external one, positively). Even such an excess can cause damage to the membrane.

There is no galvanic bond of the cell with the circuit thanks to the stepped-up high-voltage transformer. The limiting resistance R_{lim} is selected from the conditions of the permissible current through the high-voltage rectifying diode D and the suitable time constant τ of the accumulating capacitor charging C_{acc}; in this case, $\tau = R_{lim} \times C_{acc}$. The current amplitude value of the pulse passing through the cell (the average resistance for the selected object comprises about 200 Ω) could be assessed as 25 amperes. It is also easy to calculate the amount of energy released in the specimen under treatment during one pulse. At $C_{acc} = 1$ μF and $U = 6.5$ kV, we obtain

$$E = C_{acc} \times U^2/2 = 21 \text{ J}. \quad (3)$$

Such heat evolution (for $C_{acc} = 1$ μF) corresponds to a heating rate of about 3 degrees in a pulse, which is confirmed by experimental data. The discharge power in the pulse amounts to great values ($P_{max} = U_{max} \times I_{max} = 6.5$ kV × 25 A = 162.5 kW); correspondingly, the peak specific power in the experiments is $p_{max} = 162.5$ kW/cm^3 with this value not being the limiting one. Taking into account that $p_{max} \sim U^2$ and the voltage magnitude on the cell can be increased by at least 10 times (even without creation of a special atmosphere), the value $p_{max} \sim 10$ MW/cm^3 is quite attainable. Yet, at excessively large p_{max}, there is observed the phenomenon of the cell "explosion" (in the cases when local overheating and gas evolution occur because of the nonuniformity of the current distribution over the area of the electrodes) with the following development of avalanche-type breakdown. Such nonrecurrent adiabatic release of the total accumulated energy in a very small volume causes a sharp growth of the pressure in the cell.

(Fortunately, the double electric layer forming mechanism also includes the nonuniformity leveling mechanism, permitting one to generate large intensities—about 50 kV/cm—on the cell if there is met the condition that the electrodes are sufficiently parallel and gas evolution is suppressed).

At the moment of the switch closing, the voltage approximating the alternating voltage amplitude value on the step-up transformer secondary winding ($U_m \sim 6.5$ kV) is supplied to the cell. The analytic shape of the current pulse on the specimen is depicted in Fig. 7. It corresponds to the conventionally invariant (average) value $R_{cell} = 200$ Ω. It is easy to see that the current reduction curve

$$I = \frac{U}{R_{cell}} \exp[-t/(R_{cell} \times C_{acc})] \quad (4)$$

follows the exponential law. It is established in practice that the medium's specific resistance reduces as the current passes through the cell (simultaneously heating it). This effect is reflected on the real curve of the current through the cell (shown by a thin line in Fig. 7). The time constant of the capacitor discharge C_{acc} through the cell is calculated by the formula $\tau = R_{cell} \times C_{acc}$, and, at $R_{cell} = 200$ Ω and $C_{cell} = 1$ μF, we obtain $\tau = 200$ μs.

(The previous assay shows that the electrolysis faraday current is negligible at such τ). It is seen from the for-

mula that the accumulating capacitor increasing (C_{acc}) the pulse action time (duration) grows as well as the pulse energy. Thus, in practice, there are some limits of the accumulating capacitor value: at too great a capacity, there occurs the liquid medium avalanche-type breakdown because of the development of the current passage instabilities (nonuniformities) in the specimen bulk. (The greatest accumulating capacitor capacitance used in the experiments is $C_{acc} = 4$ μF).

Just before the tests, the sterile apple juice was infected with yeast cells (*Saccharomyces vini*) to a certain contamination level. After the treatment at different cultivation degrees, the number of germinated colonies was calculated by the standard microbiological research procedure.

The results of the conducted experiments on the action of high-voltage electric pulses with great leading edge steepness are the following (see the typical treatment example, Table 2).

Certain microflora suppression is noticeable even at temperatures lower than 40°C. The number of supplied pulses decreasing the microorganism population reduces until the complete absence of growth.

Note that, at the conventional heating over a water bath at the same temperatures, there is, on the contrary, observed stimulation of the yeast growth. At the produced final temperature lower than 50°C, it is possible to obtain a sterile product thanks to the action of the electric pulses. (At conventional heating, such an effect for yeasts (*Saccharomyces vini*) is observed near a temperature of 60°C after much longer holding.)

Experiments with variable accumulating capacitor values C_{acc} (variable values of the pulse energy and duration) were carried out to improve the processing regimes and refine the influence mechanism. As follows from the previous presentation, the increase of C_{acc} allows one to enhance the pulse power and the total energy and, at the same time, it reduces the possible number of supplied pulses (correspondingly, decreasing the treatment time). Contrary to our expectation, the pulse power enhancement turned out to be unproductive: according to our data, the microorganisms proved to be more sensitive to the repeated though shorter pulses (at the same total supplied energy). Thus, the pulse energy decrease with the appropriate growth of the treatment duration positively effects the outcome.

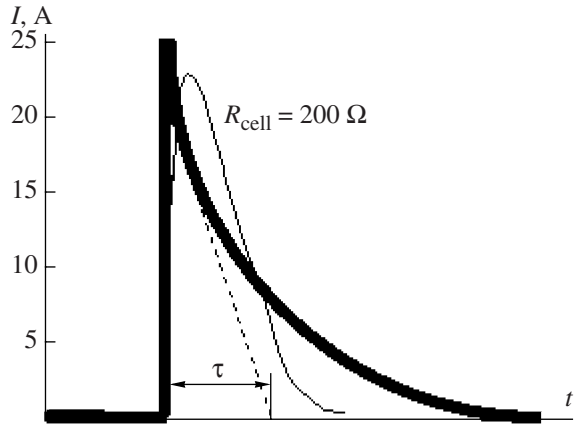

Fig. 7. Ideal (analytical) curve of the current variation through the cell at $R_{cell} = 200$ Ω (the exponent is depicted by a solid line) and the current curve shape obtained from the experiment.

It can be suggested on the basis of the presented results that the pulse edge steepness is very important along with the temperature and the treatment time factors (as is seen from Fig. 7, the steepness of only the leading edge is provided in the above described experiments, so it is possible to improve future results by making the back edge steeper too). First and foremost, this pulse processing differs from the previous treatment with currents of industrial frequency at which the voltage changes smoothly by a sinusoidal law.

There can be established a certain advantage of liquid medium electric treatment with the aim of inactivation of microorganisms by high-voltage pulses as compared with industrial frequency currents and conventional heating. It is necessary to ascertain the precise mechanism of the actions and optimize their regimes.

Table 2. The results of electric pulse treatment of clarified apple juice (pulse period $T = 5$ s)

Voltage amplitude, kV	Number of pulses	Accumulating capacitor capacity C_{acc}, μF	Experiment duration, s	Initial temperature, °C	Final temperature, °C	Contamination, KoE/sm^3	
						Yeasts	Molds
Infected juice titer						3×10^5	1×10^3
6.5	10	0.125	50	21.1	26.3	3×10^4	1.5×10^2
6.5	20	0.125	100	23.3	31.7	6×10^3	1.0×10^2
6.5	32	0.125	160	20.5	29.7	2.5×10^3	4×10^1
6.5	40	0.125	200	19.0	31.0	2.3×10^3	3×10^1
6.5	50	0.125	250	20.5	33.1	3.2×10^2	No growth
6.5	50	0.125	250	20.6	33.8	2.2×10^2	No growth

CONCLUSIONS

Liquid medium treatment by high-voltage electric pulses allows one to attain microorganism inactivation at lower temperatures and in a shorter holding time as compared with conventional thermal pasteurization methods, favoring the better preservation of a product's thermolabile components. The high-voltage electric pulse effect on liquid media is a promising method of microflora inactivation with minimum thermal damage of products. Yet the optimization of the actions (concerning the electric field intensity amplitude, the pulse shape and duration, the pulse period, and the total treatment time) is necessary for every separate product because of the enormous variety and different sensitivity of cell structures to electric influences. The sensitivity of the product's enzymes and its other components to different conditions deserves special study. There aren't enough evidential data to ensure the safety (certification) of products treated by high-voltage pulses. Further investigations are needed to promote this method.

REFERENCES

1. Kostak, B., Bacterial Considerations in Microwave Foods., *Food Eng.*, 1990
2. Sastry, S.K., Moderate Electric Field Treatments for Enhancement of Bioprocesses, *Proc. Int.Conf. "Energy-Saving Technologies for Drying and Hygrothermal Processing"*, Moscow, 2002, vol. 3, pp. 40–47.
3. Lazarenko, B.R., Roshchin, V.P., Abramova, R.V. and Yavorskaya, R.I., Electric Influence on Microrganisms, *Electr. Obrab. Mater.*, 1968, no. 5, pp. 79-84.
4. Gulyi, I.S., Ukrainets, A.I., Debelinskii, S.N., Botoshan, N.I., Chebanu, V.G., Kovbasa, V.N. and Berzoi, S.E., High Voltage electrostatic Field Effect on Beer Physical and Chemical Properties, *Electr. Obrab. Mater.*, 1991, no. 4, pp. 50–55.
5. Yarovoi, P.I., Chebanu, V.G., Stanku, M.L., Shcheglov, Yu.A., Yagina, V.S., Grigorashchenko, T.V. and Markitan, L.I., Drainage Water Decontamination by Alternating Electric current, *Electr. Obrab. Mater.*, 1985, no. 6, pp. 76–78.
6. Schindal, J., The Charge of the Ultra-Capacitors, *IEEE Spectrum*, 2007.
7. Gamburg, Yu.D., *Elektrokhimicheskaya kristallizatsiya metallov i splavov*, (Electrochemical Crystallization of Metals and Alloys), Moscow: Yanus-K, 1997.
8. Barbosa-Canovas, G.V., Qin, B.L., Swanson, B.G. (Eds) Biological Effects Induced by Pulsed Electric Fields of High Intensity, Rodrigo, M., Martinez, A., Fiszman, S.M. and Mateu, A. (Eds) Technologias avanzadas en estirilizacion y seguridad de alimentos y otros productos, Spain: Grafo ipresores, 1996, pp. 151–165.
9. Wouters, P.C. and Smelt, J.P., Inactivation of Microorganisms with Pulsed Electric Fields: Potential for Food Preservation, *Food Biotechnol.*, 1997, vol. 11, pp. 193–239.
10. Andersbach, A., Heinz, V. and Knorr, D., Effects of Pulsed Electric Fields on Cell Membranes in Real Food Systems, *Innov. Food.Sci. Emerg. Technol,* 2000, no. 1, pp. 135–149.
11. Barbosa-Canovas, G.V., Pierson, M.D., Zhang, Q.H. and Schafner, D.W., Pulsed Electric Fields, *J. Food. Sci.*, 2000, vol. 65 (supplement), pp. 65–79.
12. Ade-Omowaye, B.I.O., Andersbach, A., Taiwo, K.A. and Knorr, D., Use of Pulsed Electric Field Pretreatment tp Improve Dehydration Characteristics of Plant Based Foods, *Trends Food Sci. Technol.*, 2001, vol. 12, pp. 285–295.
13. Vasil'ev, G.M., Vasetskii, V.A., Vasil'eva, E.M. and Ganzha, V.L., Electric Pulse Technology of Milk Pasteurization, *Energoeffectivnoct'*, 2001, no. 9, pp. 12–13.
14. Hasegawa Hideo, Takeda Koji, Matsuzoe Soichi, Ueki Yutaka and Tamura Toshiuki, Sterilization using Pulsed High Voltage, *San'yo denki giho*, (*Sanyo Technical Rev.*), 2001, vol. 32, no. 2, pp. 92–100.
15. Bendicho, S., Barbosa-Canovas, G.V. and Martin, O., Milk Processing by High Intensity Pulsed Electric Fields, *Trends Food Sci. Technol.*, 2002, vol. 13, pp. 195–204.
16. Bazhal, M.I., Ngadi, M.O. and Ragavan, Zh.S.V., Synergic Effect of Pressure and Pulsed Electric Field on Food Tissue Pressing, *Electr. Obrab. Mater.*, 2003, no. 3, pp. 59–66.

ISSN 1068-3755, Surface Engineering and Applied Electrochemistry, 2009, Vol. 45, No. 2, pp. 153–156. © Allerton Press, Inc., 2009.
Original Russian Text © P.K. Khizhenkov, M.V. Netsvetov, 2009, published in Elektronnaya Obrabotka Materialov, 2009, No. 2, pp. 89–92.

ELECTRICAL PROCESSING OF BIOLOGICAL OBJECTS AND FOOD PRODUCTS

Influence of Low-Intensity Physical Factors on Plant Growth Indices: 1. Alternating Magnetic Fields and Salt Solutions

P. K. Khizhenkov, M. V. Netsvetov

Donetsk Institute for Physics and Engineering, National Academy of Sciences of Ukraine, ul. R. Luxemburg 72, Donetsk, 83114 Ukraine

e-mail: disfleur76@live.fr

Received November 21, 2008

Abstract—This paper is devoted to barley seeds processed by their soaking in sodium, potassium, calcium, and magnesium solutions with the action of simultaneous alternating electromagnetic fields (EMF), which considerably influence their growth under regular conditions. The efficiency of the combined salts and EMF action is maximum for potassium and minimal for magnesium. The EMF biological effect under the conditions of the substrate salinization depends on the field frequency—the metal ions' accumulation may increase, decrease, or remain unchanged. Each ion is characterized by its own frequency spectrum of efficiency.

DOI: 10.3103/S1068375509020136

The recent decades are characterized by the increase of anthropogenic pressure upon living beings and their habitat. Man-caused pollution comprises physical and chemical factors. The physical factors include, first of all, the electromagnetic background in a wide range of frequencies. Chemical factors are represented mainly by domestic waste (~1000 kg of garbage a year per one town dweller) and industrial contamination, including the wastes from the use of radioactive elements.

As a rule, from the viewpoint of ecological safety, the influence of each factor or group of factors on a living being should be estimated separately. At the same time, in a number of papers, it has been shown that the effect of chemical contaminants (of heavy metals) can be considerably modified at their simultaneous action with electromagnetic fields (EMF) [1–4]. It is known that ions, which are indispensable for vital functions, when in large excess in an organism, also produce a serious negative effect similar to the effect of toxins. Saline lands where the biological variety is represented by a limited number of species may serve as an example. The examination of the effects of physiological ions together with EMF is the object of the present paper.

METHODS OF INVESTIGATION

The barley seeds *Hordeum vulgare* L. (100 barley grains in a batch) were soaked in 10% solutions of sodium, potassium and calcium chloride, and magnesium sulfate for 4 hours. In each solution, one of the batches was exposed to EMF with H = 30 Oe at frequencies of f = 1.5, 8, 16, 24, 32, 40, and 50 Hz. The second batch—the control—was soaked in the solutions devoid of the field action. In addition, 14 batches were used to determine the influence of a 4-hour EMF exposure on the seeds at the swelling stage in pure water, and 8 batches were used to determine the influence of a saline solution as compared to water at $H = 0$.

On the soaking completion, the seeds of the control and the test batches were rinsed with running water and placed into a germination dish. After seven days of germinating, the quantity of the acrospires was determined in the test (n_0) and the control (n_c) and the average length of the sprouts l_0 and l_c. For the graphical plotting, the relative values of the germination $N = n_0/n_c$ and the acrospires' lengths $L = l_0/l_c$ were used.

RESULTS AND DISCUSSION

As the experimental test showed, a 4-hour EMF exposure of the seeds hydrated in pure water gives zero effect on the further germination. The acrospires of the seeds soaked in the saline solutions devoid of the field action are identical to the control ones in the way of germination, and they are behind concerning the average lengths for the salts of potassium, calcium, sodium, and magnesium as compared to the control group (relatively by 17, 19, 29 and 14%).

The obtained results demonstrate that the single short-term action of the chemical limiting factors is not life threatening for the plants, but it impedes their growth.

At EMF action in the period of soaking with the saline solutions, the picture of the plants' reaction sharply changes. The frequency dependencies of the EMF influence on the growth indices of the barley

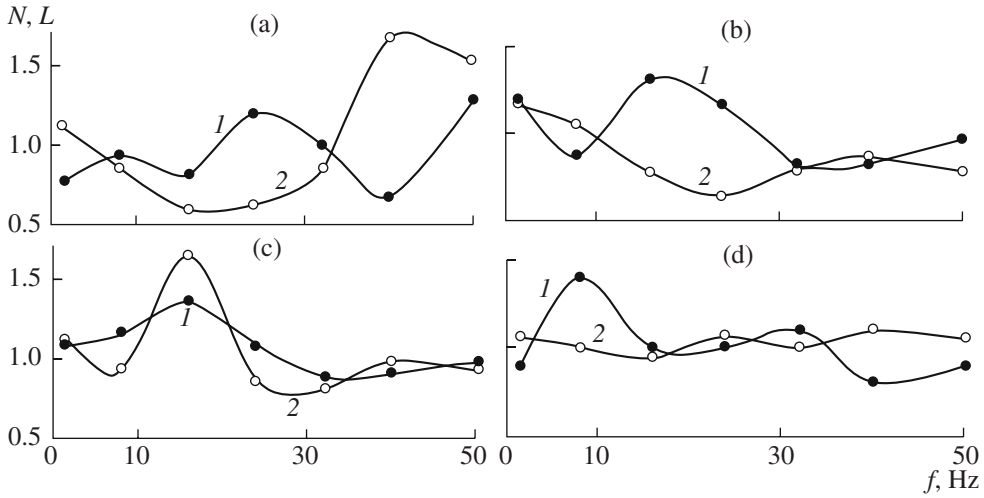

Fig. 1. The dependency of the relative germination *N (1)* and average lengths *L (2)* of acrospires after the seeds soaking in solutions of KCl (a), NaCl (b), $CaCl_2$ (c), and $MgSO_4$ (d).

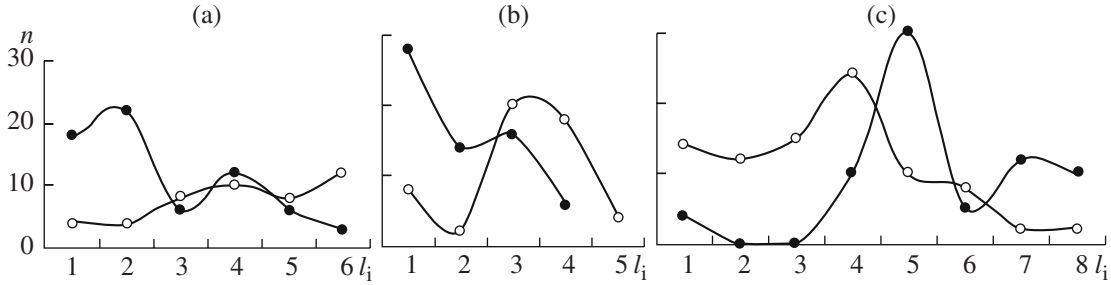

Fig. 2. The distribution of acrospires by length intervals l_i with soaking in a KCl solution and in fields of = 40 (a), 50 (b), and 24 (c) Hz. Here and further in Figs. 3, 4, 5, and 6, the acrospires lengths are given in the following intervals, mm: 1–10 (1), 11–20 (2), 21–30 (3), etc. Full circle—control; open circle—test.

couched from the seeds swelling in water solutions of potassium, sodium, and calcium chloride and magnesium sulfate are presented in Fig. 1. In all the cases, there were obtained complex nonmonotone dependencies of $L(f)$ and $N(f)$. The growth characteristics fluctuate and may exceed the control values and be less or equal to them with respect to the frequency.

For KCl, the germination at $f = 1.5$, 16, and 40 Hz is 20–30% lower versus the control; i.e., the acting factor from virtually neutral turns into limitative. Obviously, EMF at these frequencies enhance the cell membranes' permeability and influence the orientation of the biochemical reactions and, perhaps, their rate. At $f = 24$ and 50 Hz, the germination increases, but it fails to prevail authentically over the level obtained with the seeds swelling in pure water. The frequencies of 8 and 32 are neutral (Fig. 1, a) in the present experiment. The longitudinal growth of the stems in this experiment at $f = 16$ and 24 Hz was inhibited, and, at 40 and 50 Hz, it was stimulated. It should be noted here that the increase of l_{av} by 65% entailed the acrospires quantity decrease by more than 30% ($f = 40$ Hz), and the growth of l_{av} by 54% occurred at a simultaneous increase of the acrospires quantity by 27% ($f = 50$ Hz). In the present case, at the given frequencies, l_{av} considerably exceeds not only the control values but also the ones obtained at pure water soaking (by 48 and 37%). However, the growth indices' maxima in the test batches are similar to the control ones but at the same time are considerably lower than those obtained with the seeds being soaked in pure water.

In a less pronounced form, the antiphase character of the N and L indices is observed at $f = 1.5$ and 24 Hz. The $f = 40$ Hz experimental results may be interpreted from the position of the intrapopulation distinctions. At the excess concentrations of K^+ ions inside the seeds of the rapidly growing specimens, there also occurs a swift decrease of the concentration per unit of volume (or mass) of the whole organism. With slowly growing specimens, the excess concentration lasts for a longer period of time, which ruins most of them. This conclusion is partially confirmed by the comparative distribution of the acrospires according to the length ranges presented in Fig. 2.

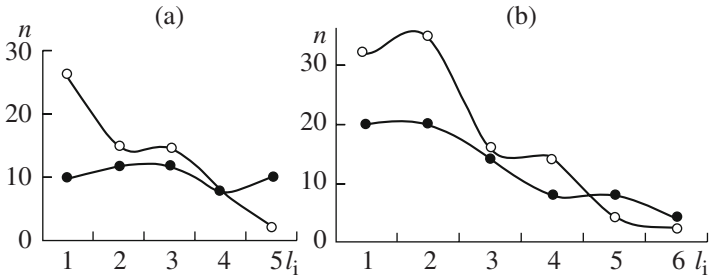

Fig. 3. The distribution of n according to l_i with the seeds soaking in an NaCl solution and fields of $f = 24$ (a) and 16 (b) Hz.

As one can see, in the intervals of 1–10 and 11–20 mm, the share of acrospires of the test batch is several times less than that of the control one. As to the 50 Hz frequency action, where both of the growth indices exceed the control ones, it may be supposed that here the main part belongs to the blocking effect of the membrane permeability for K^+ ions and, as a result, to the considerable reduction of their penetration inside the cells in comparison with the case when $H = 0$. One should note a distinction in the distribution control curves in Fig. 2. They are in antiphase. However, taking into account that here, at $f = 50$ Hz, the acrospires corresponding to $l_i = 5$ and 6 are missing, it would be more correct to think that the curves of the distribution are just shifted to the left in relation to the distribution at $f = 40$ Hz. It is these kinds of distinctions of the control indices (the experiments were carried out at each frequency on different days) that stipulate the necessity of using relative units. The changes of the control values from test to test are caused by some tertiary reasons: temperature and light fluctuations, magnetic storms, atmospheric electricity, etc. No matter how the maximum length of the sprouts changed, all the intervals always remain occupied in the test and control. The third of the observed effects referring to $f = 24$ Hz has an opposite character with respect to the first one ($f = 40$ Hz). The reason for the inversion may be both the relative increase of the potassium ion concentration inside the cells and the change of the biochemical processes' flow induced by the field. This question still remains open and is also valid for the two previous events ($f = 40$ and 50 Hz). The control indices in the test with $f = 24$ Hz differ from the previous ones too, but, taking into account the increase of the growth intervals' number, one may assume a shift of the distribution curve to the right by 3 intervals versus the test at $f = 4$ Hz. The control acrospires' length distributions in the intervals of 2–5 for $f = 40$ Hz, 1–4 for 50 Hz, and 5–8 for 24 Hz do not differ qualitatively between each other (Fig. 2).

On comparison of the test acrospires distribution within the same intervals, a like similarity is not detected. At soaking the seeds in the NaCl solution with the simultaneous EMF action, the dependencies $N(f)$ and $L(f)$ have a qualitative identity with the ones for the KCl solution (compare Fig. 1, a and b), but differ they by the intensity, especially at the 40 and 50 Hz frequencies. Here, the antiphase relations of $N(f)$ and $L(f)$ are as hard to explained as in the case of the seeds soaking in the KCl solution. The distributions of the acrospires lengths by the intervals l_i at $f = 16$ and 24 Hz have a definite qualitative similarity: in the short and average intervals, the test sprouts prevail numerically, and, vice versa, in the interval of maximum length, the control ones prevail (Fig. 3). However, the distinctions between the data on the acrospires l_i distributions in the experiments with sodium and potassium chlorides under H_A action at $f = 24$ Hz eliminate the possibility of a common response mechanism to the simultaneous action of the magnetic field and K^+ ions in one case and the field and Na^+ ions in the other.

The most simple and synphased dependencies of the growth indices on the frequency of the magnetic field (acting over the seeds soaking period) were obtained with the $CaCl_2$ solution application (Fig. 1, c). Here, the most effective frequency is 16 Hz, at which the EMF action definitely prevents the excessive penetration of Ca^{++} ions into the organism. This conclusion is also confirmed by the quantitative distribution of the acrospires with respect to the lengths (Fig. 4). In the control batch, the short acrospires numerically prevail, and, in the test one, the long acrospires numerically prevail.

The use of the $MgSO_4$ solution for soaking at $f = 8$ Hz causes the acrospires quantity to increase by 40%. At 40 Hz, a decrease by 20% is noted. At the rest of the frequencies, the effect is either zero (16 and 24 Hz) or statistically inauthentic (32 and 50 Hz). The changes of L

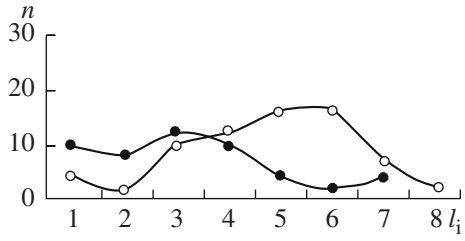

Fig. 4. The distribution of n according to l_i with the seeds soaking in a $CaCl_2$ solution and fields of $f = 16$ Hz.

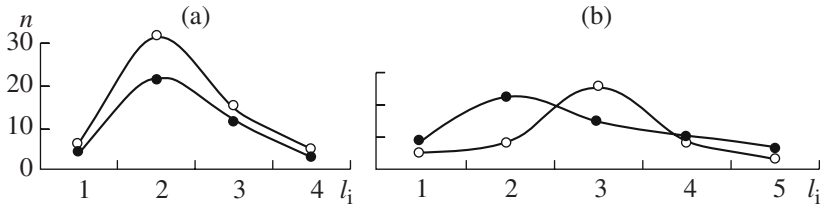

Fig. 5. The distribution of n according to l_i with the seeds soaking in an $MgSO_4$ solution and fields of $f = 8$ (a) and 40 (b) Hz.

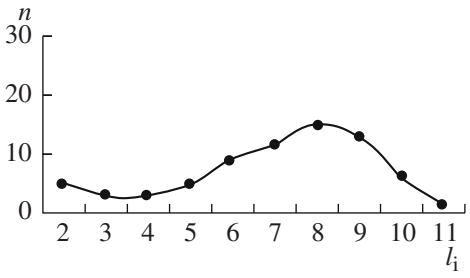

Fig. 6. The distribution of n according to l_i with the seeds soaking in pure water.

over the whole range of the investigated frequencies (Fig. 1, d) are also doubtful. Evidently, the field with the $f = 8$ Hz frequency inhibits the Mg^{++} ions penetration into the seeds. In the control and test batches, the acrospires' maximum quantity is registered in interval 2 (Fig. 5). It is impossible to explain the N decrease at $f = 40$ Hz from the viewpoint of the intensification of the magnesium penetration inside the seeds, since, in this case, in the test, the n maximum, while remaining sufficiently high, shifts to the left by one interval in the direction of the acrospires' smaller lengths.

Figure 6 displays the acrospires' numerical distribution over the length intervals obtained at the seeds germination in pure water. As was mentioned above, a single 4-hour EMF exposure under the present conditions provides no effect. The absence of salts inhibiting the growth leads to a general increase of the average lengths of the acrospires, the maximum sizes of which exceed 120 mm, and the greatest number of acrospires is observed in intervals 7–9 ($\Sigma = 45$ units). From the comparison of Figs. 2, 3, 4, 5, and 6, it is clear that the EMF frequencies stimulating the growth fail to compensate for the negative influence of the salt excess in the initial period of the seeds swelling.

CONCLUSIONS

The instability of the electromagnetic conditions change the metal (K, Na, Ca, Mg) absorption by the seeds during the soaking process.

The efficiency of the combined chemical substances and the EMF action is maximum for potassium and minimal for magnesium.

The result of the EMF biological effect depends on the field frequency: the chemical substances' accumulation may increase, decrease, or remain unchanged.

REFERENCES

1. Khizhenkov, P.K., Dobritsa, N.V., and Netsvetov, M.V., Combined Action of Alternating Magnetic Fields and Certain Chemical Substances on Barley Germination, *Electron. Obrab. Mater.*, 2004, no. 4, pp. 83–86.

2. Khizhenkov, P.K., Aleksandrova, N.V., and Netsvetov, M.V., Permeability of Cell Membranes of Plants Seed Heavy Metals Ions under Alternating Magnetic Fields Action, *Dokl. Nats. Akad. Nauk Ukrainy*, 1999, no. 8, pp. 166–169.

3. Khizhenkov, P.K., Dobritsa, N.V., Netsvetov, M.V., and Driban, V.M., The Influence of Low- and Ultra- Lowfrequency Alternating Magnetic Fields on Cell Membranes Ion Permeability, *Dokl. Nats. Akad. Nauk Ukrainy*, 2001, no. 4, pp. 161–164.

4. Khizhenkov, P.K., Netsvetov, M.V., Kislyak, T.P., and Dobritsa, N.V., The Change of Barley Seeds Cell Permeability for Negative Organic Ions Relatively to Acting Alternating Magnetic Field Frequency, *Dokl. Nats. Akad. Nauk Ukrainy*, 2001, no. 3, pp. 179–180.

ISSN 1068-3755, Surface Engineering and Applied Electrochemistry, 2009, Vol. 45, No. 2, pp. 157–160. © Allerton Press, Inc., 2009.
Original Russian Text © O.M. Postolakyi, S.A. Boortseva, 2009, published in Elektronnaya Obrabotka Materialov, 2009, No. 2, pp. 93–97.

ELECTRICAL PROCESSING OF BIOLOGICAL OBJECTS AND FOOD PRODUCTS

MM Radiation Influence Upon the Growth and Lipid Formation of *Streptomycetes Canosus CNMN-Ac-02* and Its Variants

O. M. Postolakyi and S. A. Boortseva

Institute of Microbiology and Biotechnology, Academy of Sciences of Moldova, 1, Akademiei str., Chisinauoo, MD-2028 Moldova

e-mail: oleseap@yahoo.com

Received December 18, 2008

Abstract—The collection strain *Streptomycetes canosus CNMN-Ac-02* and its two variants *Streptomycetes canosus CNMN-Ac-03* and *Streptomycetes canosus CNMN-Ac-04* obtained as a result of γ and combined γ and UV radiation have been studied from the viewpoint of their biomass and lipids composition modifications under the influence of millimeter waves. An increase of the biomass productivity in the initial strain (by 38.8%) and its variants (by 16.7 and 25.8%), as well as a decrease of the quantity of lipids in it, has been defined. The content of phospholipids, sterols, and triglycerides varies with respect to the mm radiation exposure time. The exposures that cause an increase of phospholipids and sterols in the initial culture and its variants have been determined.

DOI: 10.3103/S1068375509020148

The problem of biosystem and environment correlation has always been urgent in biology. At present, when man-made pollution of the environment has become a determining factor of destabilization of biological systems of different levels of organization, the problem of the stability of all living things under the conditions of the deteriorating environmental quality is one of the major issues in modern ecology. One of the new and so far insufficiently studied environmental biosphere factors is the electromagnetic field (EMF) of artificial origin, which considerably changes the ecological situation on our planet and intensively influences the living objects and their habitat [1 and 2].

Within the scale of the evolutionary process, the growth of the electromagnetic field intensity should be considered as a single-stage leap with hardly predictable consequences. The experimental data, both of home and foreign researchers, display high biological activity in all the EMF frequency ranges [3–5].

The biological response of living organisms is influenced by the following EMF parameters: its intensity, the radiation frequency, the radiation duration, the signal modulation, the frequency combinations, the action repetition. The combination of the above parameters may produce various kinds of consequences for the object being irradiated [4].

In the process of examination and application of the data on EMF action upon various biological systems, it is necessary to take into account the conformity of the selected test objects with the preset problems and experimental technique possibilities. The most convenient and useful models are considered to be the cells of microorganisms due to the relative simplicity of their cultivation and maintaining under laboratory conditions, as well as their short period of life [2].

Recently, the influence of mm radiation (MMR) on biological objects has been a major focus of interest. It has been noted that there is the possibility of MMR waves application as a means for obtaining information on the vital function processes of various organisms. In microbiology, the positive effect of MMR action results in growth stimulation and metabolism acceleration and changes in the cells' biochemical composition [6].

Data on the MMR influence upon the formation of lipids have not yet been met in printed materials; therefore, the purpose of this research is to study the MMR action on streptomycetes' biomass and lipids productivity.

METHODS OF THE EXPERIMENT

As the object of the investigations, 3 streptomycetes strains were selected: *Streptomycetes canosus CNMN-Ac-02* and its two variants *Streptomycetes canosus CNMN-Ac-03* (obtained as a result of γ-radiation) and *Streptomycetes canosus CNMN-Ac-04* (obtained as a result of combined γ + UV radiation) [7].

The strains maintenance was performed by the recurrent reseeding on a splay of Czapek's agar media with glucose. The cultures were stored in a refrigerator at a temperature of +4°C. Prior to the beginning of the experiment, the culture was reseeded from a test tube to Petri dishes with agar media of the above composition. The streptomycetes growth in the dishes took place in a thermostat at +27°C over seven days.

The irradiated strains were then reseeded in M-1 liquid media (the main source of carbon was 20.0 g/l of corn flour). Further cultivation was performed on a agitator for

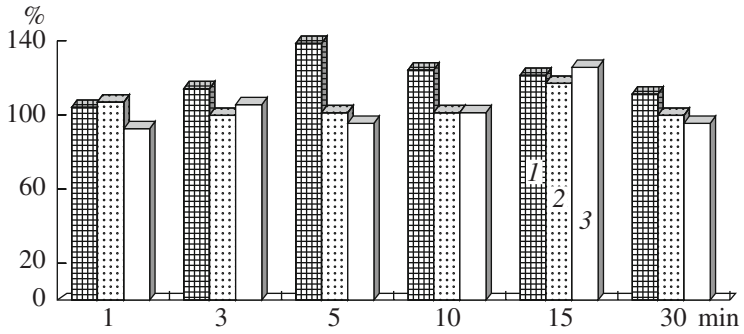

Fig. 1. Streptomycetes biomass productivity depending on the exposure time to mm waves. *1—S. canosus CNMN-Ac-02*; *2—S. canosus CNMN-Ac-03*; *3—S. canosus CNMN-Ac-04*.

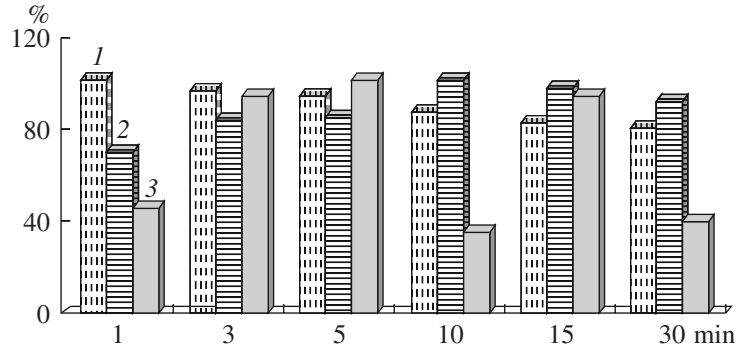

Fig. 2. Lipid formation in Streptomycetes depending on the exposure time to mm waves. *1—S. canosus CNMN-Ac-02*; *2—S. canosus CNMN-Ac-03*; *3—S. canosus CNMN-Ac-04*.

five days at 27°C. The biomass was separated from the strain broth by a centrifuge (5000 r/min, for 20 min). The biomass quantity was determined by weighing. The intracellular lipids were extracted from the biomass by the Folch method [8] modified in the laboratory [9]. The qualitative and quantitative lipid compositions were determined by the method of thin-layer chromatography on "Sorbfil" plates and densimetrically [8].

RESULTS AND DISCUSSION

Among the biologically active substances of microbial origin, lipid shave a special place. They participate in complex metabolic processes, constitute part of the cell structural elements, and are an energetically profitable substrate for oxidation as well [10–12].

Actinomyces synthesize and accumulate in their cells a considerable quantity of fats. The lipid content in mycelium of actinomyces ranges from 5 to 40% and even more with respect to the nutrient medium composition and the individual peculiarities of the organism [12, 13].

It is well known that the physical and chemical factors influence the qualitative and quantitative composition of the lipid components of the membranes, and, by means of alteration of the lipid composition of the membranes, one can reduce their negative action [7, 13, 14].

It was established earlier that the *S. canosus CNMN-Ac-03* strain differs from the initial strain of *S. canosus CNMN-Ac-02* by the higher productivity of the biomass, and the *S. canosus CNMN-Ac-04* strain differs by its higher lipid synthesis and antimicrobial activity [7].

The analysis of the streptomycetes biomass productivity change with respect to the exposure time showed that the initial strain increased its biomass productivity almost during all the exposures, reaching the maximum (138.8%) at 5-minutes irradiation (Fig. 1). The variants *S. canosus CNMN-Ac-03* and *S. canosus CNMN-Ac-04* displayed a significant biomass increase only at a 15-minute exposure, which gives, correspondingly, 116.7% and 125.8% in comparison with the test specimen. During the rest of the exposures, the biomass quantity of the variants exhibited no increase or remained at the control level.

The determination of the lipid quantity in the biomass of the three studied streptomycetes strains demonstrated that, under MMR action, there occurs their synthesis inhibition (Fig. 2). Thus, the strain of *S. canosus CNMN-Ac-02* displays an authentic decrease of the biomass lipid sum quantity beginning with 3-minutes exposure. At 30-minutes irradiation, the lipid quantity equals 80.8% in comparison with the control value. A similar process is observed with *S. canosus CNMN-Ac-03*: the lipids minimum was noted for MMR for 1 min (70.34%

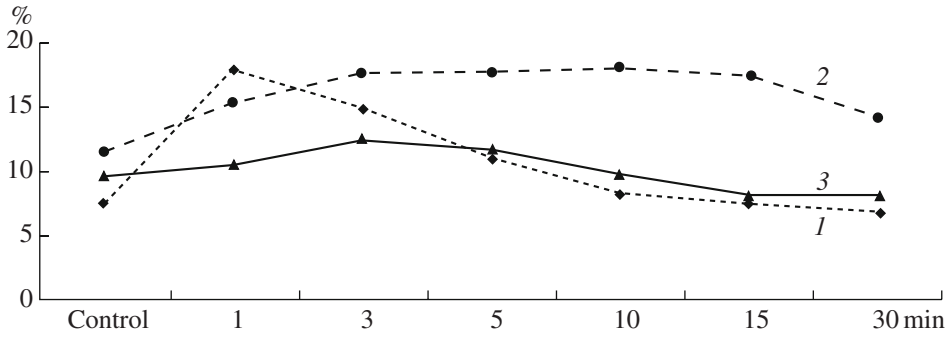

Fig. 3. The quantity of phospholipids in the Streptomycetes' biomass after being irradiated with mm waves (% of the lipid sum). *1—S. canosus CNMN-Ac-02*; *2—S. canosus CNMN-Ac-03*; *3—S. canosus CNMN-Ac-04*.

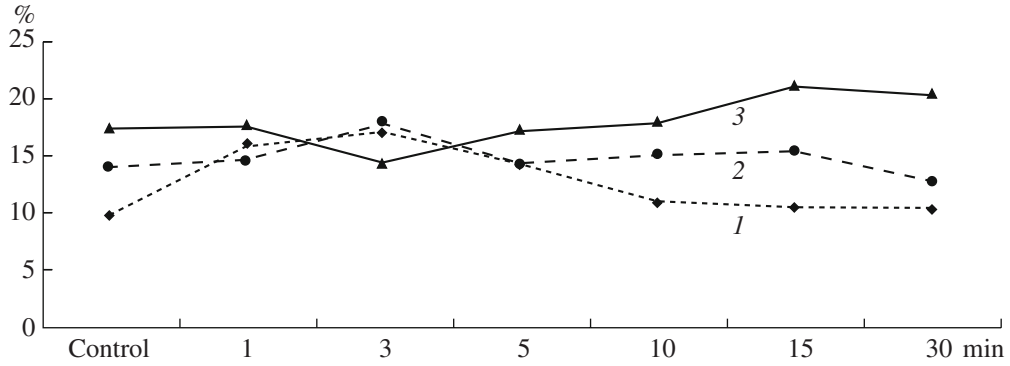

Fig. 4. The sterol quantity in the Streptomycetes' biomass after being irradiated with mm waves (% of the lipid sum). *1—S. canosus CNMN-Ac-02*; *2—S. canosus CNMN-Ac-03*; *3—S. canosus CNMN-Ac-04*.

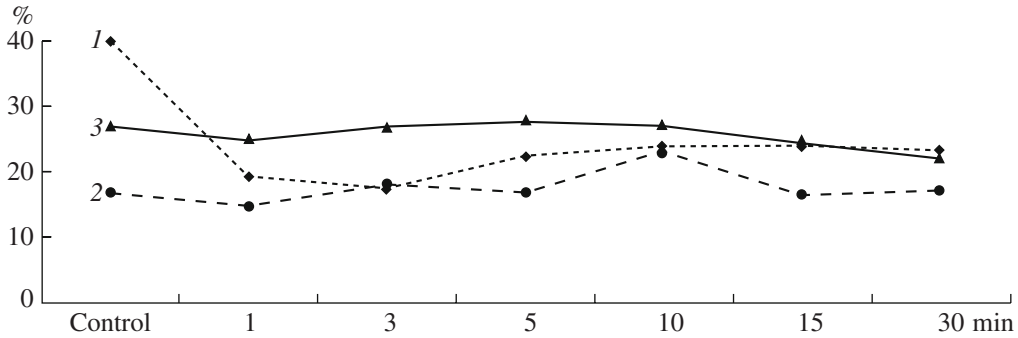

Fig. 5. The triglyceride quantity in the Streptomycetes' biomass after being irradiated with mm waves (% of the lipid sum). *1—S. canosus CNMN-Ac-02*; *2—S. canosus CNMN-Ac-03*; *3—S. canosus CNMN-Ac-04*.

versus the test specimen). *S. canosus CNMN-Ac-04* shows under mm waves a nonlinear character of the change of the lipid quantity in the biomass, which varies within the range of 35.6–102.0% in comparison with the test specimen.

The study of the lipid fractional composition and, namely, such bioactive fractions as the phospholipids, sterols, and triglycerides shows that their content in the lipids changes with regard to the MMR processing duration. Thus, a considerable increase of phospholipids by 134.0% versus the control was observed with the initial strain at a 1-minute exposure (Fig. 3). With the increase of the MMR action time, this index decreases, and, at a 30-minute exposition, it is 89.6% versus the control. The phospholipids quantity in the *S. canosus CNMN-Ac-03* strain exceeds the control value in all the experimental variants, attaining the maximum at 10 minutes irradiation (57.8% greater than the control figure). With *S. canosus CNMN-Ac-04*, at minor exposures, the phos-

pholipids quantity in the biomass exceeds the control. As the MMR action time increases upon this strain, the quantity of the phospholipid fraction in the lipids decreases. Thus, their quantity reaches the maximum at a 3-minute exposure and exceeds the control value by 28.8%; at a 30-minute exposure, the quantity is less than in the test specimen (by 16.4%).

The experiments showed that the MMR action in the time range of 1–10 min involves the sterol synthesis stimulation by the *S. canosus CNMN-Ac-02* strain. The sterols quantity in the lipids attains the maximum at 3-min irradiation. The most active sterols synthesis was also observed at a 3-min exposure in the *S. canosus CNMN-Ac-03* strain. The inverse effect was displayed by the *S. canosus CNMN-Ac-04* strain at 3-min MMR action: in this case, the sterols quantity in the lipids decreases and becomes 82.7% versus the control. The maximum sterols quantity was observed at the *S. canosus CNMN-Ac-04* 15-minute irradiation (by 19.5%).

The change of the triglycerides quantity in the lipids of the three studied streptomycetes strains under MMR action occurred in the following way: it considerably decreased in *S. canosus CNMN-Ac-02* (by 40.0–80.0% versus the control), and, in *S. canosus CNMN-Ac-03* and *S. canosus CNMN-Ac-04*, there was observed minor triglycerides synthesis stimulation at the 5- and 10-minute exposures.

In conclusion, it can be said that, under MMR action, there occur considerable changes of the growth and lipid formation in streptomycetes. The reaction of each strain is individual in accordance with the exposure. A general regularity has been defined: the biomass productivity stimulation involves a lipids synthesis decrease. In our opinion, the quantitative increase of the bioactive phospholipids fraction indicates the activation of the microorganism's protective reaction against a physical factor action.

REFERENCES

1. Betskii, O.V. and Deveatkov, N.D., *Biologicheskie aspekty mm voln nizkoi intensivnosti* (Biological Aspects of Low Intensity mm Waves), Moscow: Seven Plus, 1994.
2. Gapochka, L.D., Gapochka, M.D., and Korolev, A.F., Population Aspects of Unicellular Organisms Tolerance to Low Intensity Electromagnetic Radiation Influence, *Mm Waves Biol. Med.*, 2002, no. 2(26), pp. 3–9.
3. Tambiev, A.X., Kirikova, N.A., and Luk'yanov, A.A., Application of Active Frequencies of mm and sm Electromagnetic Radiation in Microbiology, *Naukoemkie Tekhnol.*, 2002, no. 1, pp. 34-–53.
4. Egorova, E.I., Microwave Radiation Influence on the Quantitative and Biomass Change of Planktonic Algae, *Biomed. Tekhnol. Radioelektron.*, 2006, no. 1–2, pp. 54–58.
5. Ghitu, D.I., Betchii, O.V., Parhomenko, V.F., Rotaru, A.N., and Rusu, D.T., Unele probleme fundamentale si applicative ale rediatiilor altatromagnetice de frecventa extreme de inalta (milimetric) atermice, *Materialy I Mezhdunarodnoi Nauchno-Practicheskoi Konferentsii "Netraditsionnye metody v meditsine, biologii i rastenievodstve. Eniologiya. Ekologiya i zdorov'e"* (Proc. Int. Conf. " Non-Traditional Methods in Medicine, Biology and Plant Cultivation. Eniology. Ecology and Health") Chisinau, 2005, pp. 41–47.
6. Gamayurova, V.S., Krynitskaya, A.Yu., and Astrakhantseva, M.N., Influence of SWF EMR of Nonthermal Intensity on *Saccharomices Cerevisiae* Yeast Growth, *Zh. Radioelektron.*, 2003, no. 3., pp.
7. Rastimeshina, I.O., Study of Conditions of Bioactive Substances Directed Synthesis by *Streptomycetes canosus* CNM-71 Culture, *Abstract of. Doctoral (Biol.) Dissertation*, Chisinau, 2001.
8. Keits, E.M., *Tekhnika lipidologii* (Lipidology Techneque), Moscow: Mir, 1985.
9. Burţeva, S., Usatîi, A., and Toderaş, A., Variabilitatea formelor spontane a tulpinii *Streptomycetes sp.36* – producatoare de substante bioactive, *Buletinul AŞ RM, Ştiinţe biol. Si chim.*, 1996, no. 1, pp. 27–32.
10. Dyatlovitskaya, E.V., and Bezuglov, V.V., Lipids as Bioeffectors. Introduction, *Biokhimiya*, 1998, no. 62, issue 1, pp. 3–5.
11. El-Naggar, M.Y., El-Kersh, M.A., and El-Sharaky, A.S., Correlation of Actinomycin X_2 to the Lipid Profile in Static and Shaken Cultures of Streptomycetes Nastri Strain YG 62, *Microbios*, 1999, vol. 100, no. 396, pp. 117–127.
12. Lomtatidze, L., Shiukashvili, T., Aneli, G., and Mamulashvili, K., Fatty Acids of Cell Wall Lipids of Some Actinomyces, *Bull. Georg. Acad. Sci.*, 2001, vol. 163, no. 1, p. 164.
13. Boortseva, S.A., Biologically Active Substances of Streptomycetes (biosynthesis, properties, application prospects), *Abstract of Doctoral (Biol.) Dissertation*, Chisinau, 2002.
14. Zalashko, M.V., Solokhina, T.A., and Koroleva, I.F., Influence of Stress Actions on Yeast Lipids Composition, *Prikl. Biokhim. Mikrobiol.*, 2000, vol. 36, no. 1, pp. 37–40.

ISSN 1068-3755, Surface Engineering and Applied Electrochemistry, 2009, Vol. 45, No. 2, pp. 161–166. © Allerton Press, Inc., 2009.
Original Russian Text © Sh.M. Abbasov, G.T. Agaverdiieva, A.S. Baitsar, U.F. Faradzhova, G.M. Mekhdevi, 2009, published in Elektronnaya Obrabotka Materialov, 2009, No. 2, pp. 98–104.

OPERATING EXPERIENCE

Structure and Principal Electrophysical Properties of Ge_{1-x}–Si_x Thin Films

Sh. M. Abbasov[a], G. T. Agaverdiieva[a], A. S. Baitsar[b], U. F. Faradzhova[c], and G. M. Mekhdevi[a]

[a]*Institute of Radiation Problems, National Academy of Sciences of Azerbaijan, ul. F. Agaeva 9, Baku, AZ-1143 Republic of Azerbaijan*
e-mail: shabbasov@rambler.ru
[b]*I. Franko L'vov State University, Ukraine*
[c]*National Aviation Academy of Azerbaijan, Baku, Azerbaijan*

Received November 20, 2008

Abstract—In the process of thermal treatment of deposited $Ge_{0.85}Si_{0.15}$ films, a number of peculiarities were found related to the character of their conductivity. The films of $Ge_{0.85}Si_{0.15}$ solid solutions are rather resistant to thermal quenching. It was shown experimentally that irradiation with electrons under an accelerating voltage enhances the crystallization in the films and lowers their electric conductivity.

DOI: 10.3103/S106837550902015X

INTRODUCTION

Ge and Si exhibit an unlimited mutual solubility both in the solid and the liquid state, and this agrees well with the nature of these elements. They possess analogous chemical properties and similar atomic radii and occupy adjacent places in the electrochemical series. Ge and Si possess a diamond-like crystal lattice. The ratio $a_{Ge}/a_{Si} = 1.042$; that is, the lattice parameters differ by less than 4.3% [1].

The authors of the phase diagram [2] noted that the alloy crystallization in the usual conditions is inhomogeneous. With a decrease in temperature, the solid phase that eliminates under cooling retains a higher concentration with respect to the equilibrium one.

The phase diagram was studied theoretically. It was found that, to provide the correlation between the theoretical and experimentally observed solidus and liquidus curves, it is necessary to accept that the interaction between the like atoms Ge–Ge and Si–Si should be weaker than between the Ge–Si atoms; therefore, there is a tendency to ordering in the solid solution.

The results of work [3] have shown that the number of interstitial atoms in the Ge–Si solid solution is so small that it is beyond the sensitivity threshold of X-ray analysis.

According to the X-ray data, the lattice constant of Ge–Si alloys changes linearly with the change in the composition. The Si atoms deform the Ge lattice decreasing its parameter.

EXPERIMENTAL

In Ge_{1-x}–Si_x alloy ($x = 0$–0.15), the atoms of silicon and germanium are randomly located in the sites of the diamond-like lattice. Since the alloy is not an ideal crystal, but a crystal with imperfections in the periodicity of the lattice structure, it does not possess an energy band structure in the strict sense of this term. However, it is possible to examine some features of the energy band structure of the alloy.

The electron energy spectrum consists of a large number of energy intervals with a high density of destroyed states in them. The energy spectrum of the alloy also consists of a large number of intervals where a low density of destroyed states is present; those are mainly forbidden gaps. The electron energy spectrum of the alloy can be represented as consisting of a large number of destroyed bands with a high density of states possessing small "tails" (regions with a low density of states), which penetrate the forbidden bands (regions with a negligibly low density of states). Since the lattice constants for ideal crystals of silicon and germanium only differ by several percent and germanium and silicon atoms possess the same valence, it is probable that the "tails" in the energy spectrum of the germanium–silicon alloy are rather of secondary (not of primary) importance in the energy spectrum.

Much attention is paid to the study of the electric properties of strongly doped and compensated solid solutions [4].

It was stated that the mobility decreased in the temperature range of $T = 300$–700 K as $T^{-1.1}$ and $T^{-0.9}$ in uncompensated and compensated samples, respectively [4]. Using these data, the ionic component of the mobility was determined (Fig. 1) [5]. In this calculation, the dependence $\mu \sim T^{-0.8}$ was taken for the dispersion on inhomogeneities of the solid solution and $\mu_T \sim T^{-3.5}$ for the dispersion on lattice vibrations. In the range of 50–100 K, the dependence

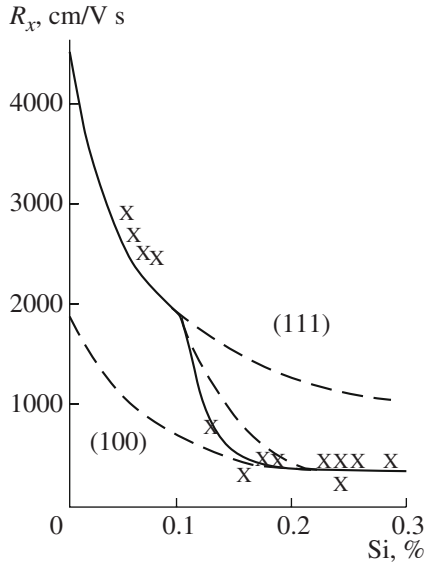

Fig. 1. Dependence of the Hall mobility versus the percentage composition of $Ge_{1-x}Si_x$ solid solutions. The dashed line corresponds to the (111) and (100) areas without the interstitial dispersion. The thick line shows the arbitrary form of the interstitial dispersion.

$\mu_T \sim T^{-2}$ was taken [6], and it was assumed that $\frac{1}{\mu_{i.i.}} = \frac{1}{\mu_{exp}} - \frac{1}{\mu_i} - \frac{1}{\mu_t}$ taking into account the corrections according to the results obtained in [6]. In the crystals of Ge–Si solid solutions with the silicon content up to 15%, the hole mobility for the dispersion on lattice vibrations changes for $\mu_p \sim T^{-2.33}$ in the range of 100–280 K in the same fashion as in pure germanium [7].

To perform the process of vacuum evaporation of the substance, an evaporation source is needed that can contain the evaporated substance and maintain its temperature at a level high enough to provide the necessary vapor pressure. The deposition rate of the films can be varied from values of less than 1 Å/s to values exceeding 1000 Å/s.

To approximately evaluate the operation temperature of the source, one should possess a steady vapor pressure of the evaporated material (germanium–silicon solid solution) on the order of 10^{-2} Torr to provide a rate of the film deposition on the order of 4.5–5 nm/s. Tungsten was used as the source material; the source temperature was maintained at a level of 2100 K. The source was made in the laboratory in the form of a boat 4 cm long and 1 cm wide. Tungsten is a brittle material, and this created the only problem that we experienced while making the source. The ends of the electric contacts were connected to the copper contact terminals.

The condensation of a molecular beam with some density (the number of atoms that reach the substrate in a unit of time) occurs only at a temperature that does not exceed some critical temperature T_{cr}. The critical flux density is always present, and, at the specific temperature T_{cr}, the condensation begins (on the given substrate) [8].

As is known, the migration of the adsorbed particles on the substrate surface exhibits isotropy. This idea is true for amorphous substrates, but it should be revised for the case when the condensation on a crystalline substrate is examined.

Nucleation of vacuum condensates on a neutral (in particular, amorphous) substrate can occur according to two main mechanisms: vapor–crystal [V $\longrightarrow$ C]; that is, direct condensation from the vapor state into the crystalline state occurs; and vapor– liquid [V $\longrightarrow$ (L $\longrightarrow$ C)]; that is, the vapor transforms into the liquid. Further, the liquid can remain in the overcooled amorphous state or crystallize [L $\longrightarrow$ C].

The critical temperature was found experimentally to be $T_{cr1} \approx 2/3T_m$. Below this temperature, the mechanism V $\longrightarrow$ C takes place, and, over this temperature, the mechanism V $\longrightarrow$ L occurs (T_m is the melting temperature of the condensed material in its bulk form). The T_{cr1} values can vary in definite limits in dependence on the properties of the condensate and the substrate material, the binding energy between them, the condensation rate, and other conditions of the condensation process. Some authors [9] suggested that a second critical temperature exists: $T_m = T_{cr2} \approx 1/3T_m$. Over this temperature, the V $\longrightarrow$ C mechanism takes place, and, below it, the mechanism V $\longrightarrow$ L occurs. This assumption is based on various experimental data related to research on the condensation of a large number of metals as well as some alloys. The data of microscopic and X-ray methods and microhardness measurements give evidence that an interval ΔT_{cr} exists, where heterogeneous condensation according to both mechanisms occurs (V $\longrightarrow$ C and V $\longrightarrow$ L). The T_{cr} and ΔT_{cr} values can vary in some limits dependent on the condensation conditions. In the low temperature range of condensation ($T_m < T_{cr}$), the condensation according to the V $\longrightarrow$ L mechanism sometimes leads to the formation of metastable crystalline and amorphous (vitreous) phases (V $\longrightarrow$ L $\longrightarrow$ C or V $\longrightarrow$ L $\longrightarrow$ A, where A is an amorphous phase) that completely or partly transform into more stable phases at long storage or heating [10].

In the case, when an "active" (single-crystalline) substrate is used and the epitaxial or autoepitaxial growth of single-crystalline layers takes place characterized by strong bonds with the substrate, the condensation mechanism V $\longrightarrow$ L is suppressed and the temperature range ($T_{cr1} - T_{cr2}$) widens where the mechanism V $\longrightarrow$ C occurs.

The examined condensation mechanisms refer to the initial stage only. At the following stages, the nuclei of the liquid phase are not stable, and the transition into the crystalline phase (L $\longrightarrow$ C) occurs. However, the preceding mechanism V $\longrightarrow$ L leaves its imprint in the form of defects of the crystalline structure in the condensate, which in turn influence the structure-sensitive properties. This was used for the indirect detection of

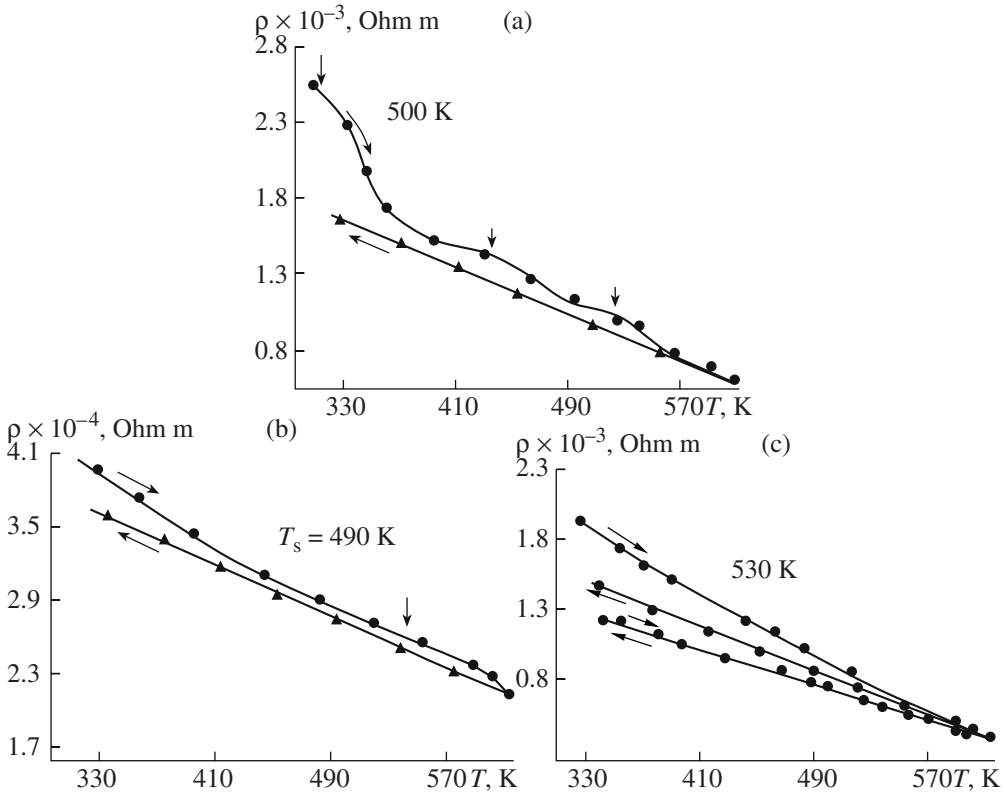

Fig. 2. Temperature dependence of the resistance of $Ge_{1-x}Si_x$ ($x = 0.15$) films; $n = 100$ nm.

the V ⟶ L mechanism at $T_m < T_{cr2} \sim 1/3T_m$ in bulk condensates.

It is assumed that, in the case of flash evaporation, a pure V ⟶ C condensation mechanism takes place (without the film submelting). In practice, a satisfactory film structure can be obtained only after additional recrystallization of the deposited film.

To obtain a perfect structure using the method of flash evaporation, a staggered condensation V ⟶ C and V ⟶ L ⟶ C is performed via the condensate heating to $T > T_m$ (melting) using the heat radiated by the source.

Nowadays, the problem of the thermal stability of the electrophysical properties of semiconductor materials is of great importance in solid-state technology. However, each field of technical application of semiconductors advances its specific demands concerning their principal characteristics.

At the present time, the influence of the temperature on the electrophysical properties of germanium and silicon has been studied rather well, and it was established that these two elements, while containing oxygen, exhibit thermal instability. The point is that oxygen reveals both the neutral and the electrically active character in germanium and silicon and substantially changes their electrophysical properties with the temperature changing [11]. Film condensates of germanium–silicon solid alloys are especially sensitive to oxidation both during the evaporation and during the quenching processes.

A number of peculiarities associated with the character of the conductivity were found during the thermal treatment of the deposited $Ge_{0.85}Si_{0.15}$ films. The films of $Ge_{0.85}Si_{0.15}$ solid solutions are rather resistant to thermal treatment. The condensates prepared at $T_s = 490$ K (Fig. 2a) were of a quasi-amorphous type. In the temperature range of 350–450 K, they exhibit a semiconductor behavior of conductivity with a thermal activation energy of 0.052 eV. This value was determined from the slope of the plot $\log\sigma = f(1/T)$ drawn according to the experimental values (Fig. 2). In the temperature ranges of 450–550 K and 550–680 K, the semiconductor type of conductivity is retained and the activation energy somewhat increases and amounts to 0.096 eV. In these temperature ranges, the three intervals (350–420, 510–540, and 590–620 K) are observed with more sharp changes in the electric conductivity; they can be associated with crystallization processes in the condensates (Fig. 4).

It can be seen in the dependence $\log\sigma = f(1/T)$ (Fig. 3) that the conductivity sharply increases with the temperature increase beginning from 600 K. This is associated with the intrinsic conductivity. Curves 1 and 2 show different temperatures of transition to the intrinsic conductivity. The activation energy at these temperatures is 0.22 and 0.26 eV. The interval from 360 to 600 K for curves *1*

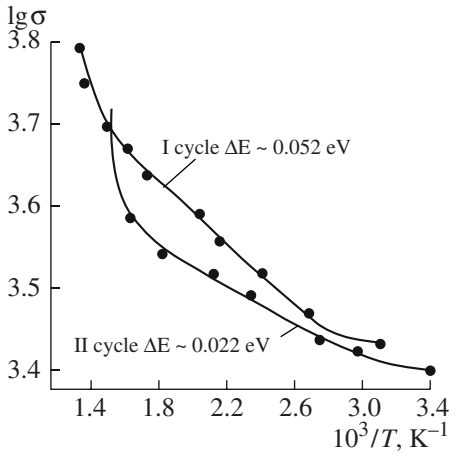

Fig. 3. Dependence of the conductance versus the temperature of $Ge_{1-x}Si_x$ ($x = 0.15$) films at thermocycling.

and *2* corresponds to the values of the activation energy of 0.054 and 0.022 eV.

The kinetics of the crystallization and the thermal stability were studied via heating the amorphous film directly in the column of a UEMV-100K electron microscope using a PRON-2 attachment (Fig. 5). The thermal stability of the amorphous state was determined via the appearance of the most intensive diffraction reflections of the crystalline phase against the background of the diffuse maxima of the amorphous phase. The thermal stability of the amorphous state was studied in the films deposited on the substrates at room temperature and at 490 K.

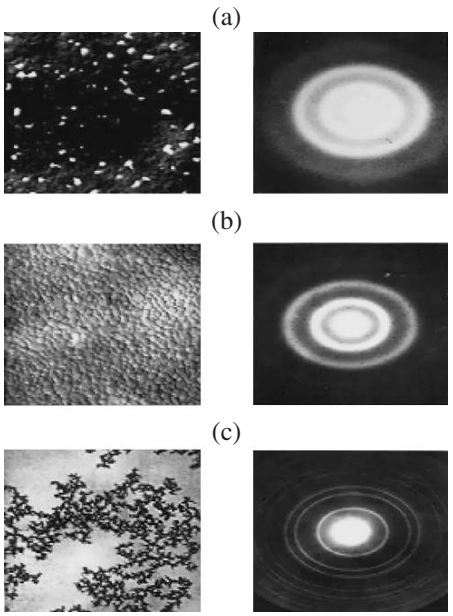

Fig. 4. Micrographs and electron-diffraction patterns of $Ge_{1-x}Si_x$ ($x = 0.15$) films: $n = 100$ nm, T_s, K: (a) 490, (b) 500, (c) 530 K × 3500.

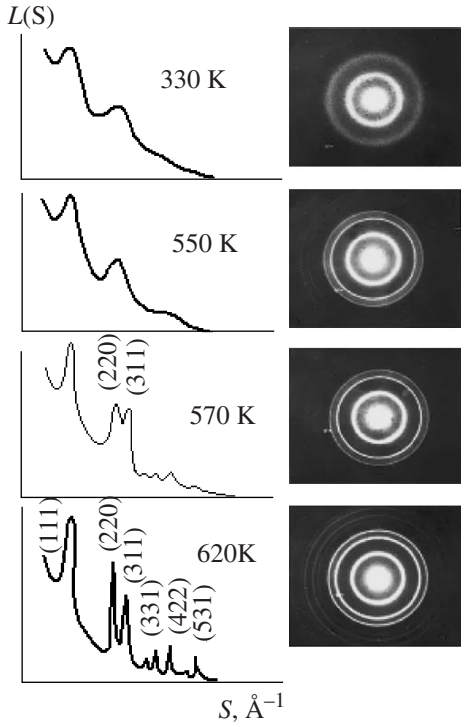

Fig. 5. Crystallization kinetics of $Ge_{1-x}Si_x$ ($x = 0.15$) solid solution.

Figure 5 shows the successive stages of the structure transformations in the amorphous films. The amorphous $Ge_{0.85}Si_{0.15}$ films in their initial state are not in a state of thermal equilibrium but relax to a metastable state. With the temperature increase, the quenching of defects and changes in the free volume and topological short range ordering occur. The composition order does not change in this process.

The amorphous films possess some quantity of stored heat, which liberates during the crystallization of the amorphous phase; in this process, the properties of the film change irreversibly. It is important to know the crystallization mechanism on the microscopic level for the practical application of $Ge_{1-x}Si_x$ ($x = 0.15$) amorphous films. These studies would allow one to draw conclusions concerning the possible widening of the temperature range where the amorphous films can be effectively used. The controlled crystallization can be used for making superdispersed structures.

The amorphous $Ge_{0.85}Si_{0.15}$ films crystallize at a temperature of 565 K. The rate of the continuous heating directly in the column of the electron microscope amounts to 10 K/min. The initiation of the crystallization process is registered by the appearance of the most intensive diffraction lines [(111), (220), and (311)] of the crystalline phase of the solid solution in the elec-

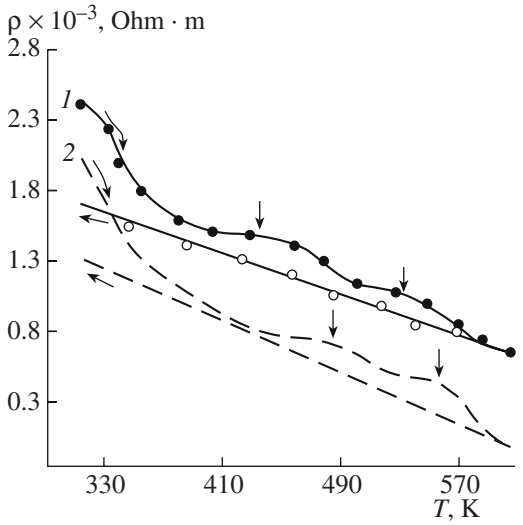

Fig. 6. Dependence of the resistivity of $Ge_{1-x}Si_x$ ($x = 0.15$) solid solution versus the temperature: (*1*) before irradiation, (*2*) after irradiation.

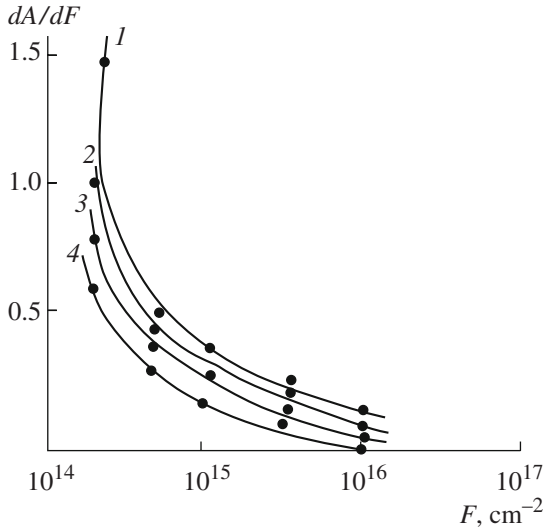

Fig. 7. Dependence of the rate of generation of defects versus the irradiation dose for various Si contents in *n*-$Ge_{1-x}Si_x$ solid solution: (*1*) $x = 0$, (*2*) $x = 0.05$, (*3*) $x = 0.10$, (*4*) $x = 0.15$.

tron-diffraction patterns against the background of the diffuse haloes.

The growth of the crystalline phase occurs in a dendrite fashion with formation of multiple bifurcations in the amorphous phase. When the temperature increases by 15–20 K, the crystallizations terminates with the formation of a continuous polycrystalline film of the solid solution.

The crystallization temperature of $Ge_{0.85}Si_{0.15}$ amorphous films is only 15 K greater than that of the films of amorphous germanium. This fact gives evidence that the same nondiffusional crystallization mechanism occurs in both cases. That is, the silicon addition to germanium does not lead to a substantial increase in the thermal stability of the amorphous state. It is known that the thermal stability of the amorphous state can be considerably increased by doping with an impurity that does not form solid solutions with the host material or possesses significantly different atomic dimensions. Taking this into account, one should expect increasing of the thermal stability of the amorphous films in the system Ge–$Si_{0.15}$ in such an interval of compositions where the destruction of the solid solution occurs. In this case, the mechanism of the diffuse stratification of the amorphous material with the temperature increasing will be the defining crystallization process; this will substantially retard the crystallization processes and lead to the increasing of the thermal stability of the amorphous state.

An additional crystallization at continuous heating at the rate of 25 K/min was performed to clarify the crystallization mechanism. The temperature of the initiation of the crystallization process is virtually the same in the case of the continuous heating with rates of 10 and 25 K/min; this proves the nondiffusional character of the interatomic reconstructions in $Ge_{0.85}Si_{0.15}$ amorphous films, as well as gives evidence of the highly homogeneous interatomic distribution in the amorphous films.

INFLUENCE OF IRRADIATION ON THE ELECTRIC CONDUCTIVITY AND CRYSTALLISATION OF $GE_{1-X}SI_X$ FILMS

The method of irradiation with electrons involves two basic elements:

(a) a source of electrons (an EM-9 electron microscope and a linear accelerator of electrons of the ELU-6 type);

b) a special attachment located instead of the microscope observation window (or luminescent screen).

The irradiation of the samples by an electron beam can be performed using a defocused or focused spot (projective or objective mode of operation) at an accelerating voltage of 35 kV. The attachment allows using replaceable cutting diaphragms to vary the dimensions of the irradiated area, to measure the resistivity of the samples in the process of irradiation, and to control the temperature of the samples.

The $Ge_{1-x}Si_x$ (x = 0.15) samples were irradiated by an electron beam with a surface area of 5 × 2 mm for 1.5 hours.

The temperature dependence of the electric conductivity of the Ge–Si samples show that the electric conductivity decreases and the slope of the line $R = f(T)$ increases as a result of the irradiation (Fig. 6); this suggests that the thermal activation energy increases. This phenomenon is most pronounced in the high temperature range. This behavior of the electric conductivity of the $Ge_{1-x}Si_x$ amorphous films gives evidence that the

conductivity gap broadens. Evidently, the action of the electron flux accelerates the partial crystallization and leads to the capture of oxygen atoms.

It was established that, when the silicon content in the *n*-type $Ge_{1-x}Si_x$ thin films increases, the rate of formation of radiation defects also increases (Fig. 7), and the dose necessary to produce the *n* to *p* conversion decreases. The higher the silicon content in the $Ge_{1-x}Si_x$ samples irradiated with the same relative doses of electrons, the higher the concentration of holes after the conversion of the conductivity type.

The data collected during the experiments concerning the action of fluxes of accelerated electrons on the mechanical properties of the crystals on the basis of $Ge_{1-x}Si_x$ can be explained if we suppose that the simplest defects in the crystal structure induced by the irradiation are vacancy-type lattice defects [12].

One can suppose that empty sites (vacancies) and displaced atoms introduce a set of energy levels into the forbidden gap. Complexes are formed in the presence of uncontrolled impurities in the crystal. Unlike the pure components, the Ge–Si solid solution is an inhomogeneous material, and it can be represented as a two-phase system. The interface between the phases is a source of strong elastic strains and is characterized by the maximal density of dislocations.

Taking into account these considerations, we proposed a model to explain the radiation effects in $Ge_{1-x}Si_x$ involving the concept of the structural inhomogeneity of the solid solutions, which consist of the regions enriched with silicon or with germanium.

The interface between these regions acts as an effective drain for interstitial atoms formed owing to the radiation. The intensive adsorption and accumulation of free vacancies in the bulk of the material define the peculiarities of the radiation processes in $Ge_{1-x}Si_x$ solid solutions and devices on their basis [13].

According to the proposed model, the point defects formed in $Ge_{1-x}Si_x$ interact with structural defects and form complexes that act as recombination centers and decrease the concentration of charge carriers. This results in changes in the mechanical and electrical characteristics of the irradiated samples.

REFERENCES

1. Kikorkin, N.N., *Rost kristallov* (Crystal Growth), Izd. AN SSSR, 1959, pp. 132–134.
2. Elliott, R.P., *Constitution of Binary Alloys, First Supplement*, McGraw-Hill, 1965.
3. Smith, R.A., *Semiconductors*, Cambridge, UK: Cambridge Univeristy Press, 1961.
4. Adzharov, G.Kh., Ganiev, A.S., and Shakhtakhtinskii, M.G., Energy Spectrum of Ground States of Shallow Acceptor Centers and Effective Masses of Holes in the Crystals of Germanium–Silicon Solid Solutions, *Dokl. Akad. Nauk Azerb. SSR*, 1981, vol. 37, no. 8, pp. 36–40.
5. Abbasov, Sh.M., Mamedov, V.S., Shakhovtsov V.I., Gasumov, G.M., and Zagainova, L.I., Intrinsic and Lattice Absorption in Ge–Si Solid Solutions at 4.2 K, *Dokl. AN Azerb. SSR*, 1980, vol. 36, no. 6, pp. 33–36.
6. Golikova, O.A., Iordanashvili, E.K., and Petrov, A.V., Electrical Properties of Solid Solutions in the System Si–Ge, *Fiz. Tverd. Tela (Leningrad)*, 1966, vol. 8, no. 2, pp. 500–507.
7. Agaev, N.A., and Adzharov, G.Kh. Mobility of Holes in the Crystals of Germanium—Silicon Solid Solutions, *Mater. dokl. po issledovaniyu i primeneniyu tverdykh rastvorov germanii–kremnii* (Report on the Study and Application of Germanium—Silicon Solid Solutions), Baku, 1990, pp. 56–62.
8. Palatnik, L.S., and Papirov, I.I., *Orientirovannaya kristallizatsiya* (Oriented Crystallization), M: Metallurgiya, 1967.
9. Metsik, M.S., Golub', L.M., and Shermanov, L.A., Modification of the Electrical Relief of Solid State Surfaces in the Process of Neutralization of Active Centers by Thermal Treatment and Deformation, in *Aktivnaya poverkhnost' tverdykh tel* (Active Surface of Solids), M.: Izd. VINITI, 1976, p. 170.
10. Palatnik, L.S., Fuks, M.Ya., and Kosevich, V.M., *Mekhanizm obrazovaniya i substruktura kondensirovannykh plenok* (Mechanism of Formation and Substructure of Condensed Films), M.:, Nauka, 1972.
11. Tkachev, V.D., Makarenko, L.F., Markevich, L.F., and Murin, L.I., Rearranging Thermodonors in Silicon, *Fiz. Tekh. Poluprovodn*., 1984, vol. 18, no. 3, pp. 526–531.
12. Abbasov, Sh.M., *Vliyanie oblucheniya na elektrofizicheskie, opticheskie i fotoelektricheskie svoistva tverdykh rastvorov germanii–kremnii* (Influence of Irradiaiton on the Electrophysical, Optical and Photoelectrical Properties of Germanium—Silicon Solid Solutions), Baku: Elm, 2003.
13. Abbasov, Sh.M., Agaverdiyeva G.T., Ibrahimov Z.A., and Farajova U.F. Investigation of Electrophysical and Photoelectrical Properties of $Ge_{1-x}Si_x$/Ge Heterostructures Obtained by Molecular-beam Epitaxy Method, *The Fifth Eurasian Conference on Nuclear Science and Its Application*, October 2008, Ankara, Turkey, pp. 241–242.

ISSN 1068-3755, Surface Engineering and Applied Electrochemistry, 2009, Vol. 45, No. 2, pp. 167–170. © Allerton Press, Inc., 2009.
Original Russian Text © M.B. Muradov, A.Sh. Abdinov, R.H. Hajimamedov, G.M. Eyivazova 2009, published in Elektronnaya Obrabotka Materialov, 2009, No. 2, pp. 105–108.

OPERATING EXPERIENCE

Dielectric Properties of Nanocomposites on the Basis of Copper Sulfide Nanoparticles and a Polymer Matrix

M. B. Muradov, A. Sh. Abdinov, R. H. Hajimamedov, and G. M. Eyivazova

Baku State University, Z. Khalilov str. 23, AZ1073 Baku, Republic of Azerbaijan

e-mail: mbmuradov@gmail.com

Received November 24, 2008

Abstract—The temperature dependences of the dielectric permittivity and conductivity of nanocomposites on the basis of nanoparticles of copper sulfide and a polymer matrix (polyvinyl alcohol) were investigated in the frequency range of 265 Hz–1 MHz. The activation energies of the charge carriers were determined using the temperature dependence of the conductivity. It was found that this energy depends on the size of the formed particles. The alteration of the conductivity values dependent on the number of cycles is associated with the redistribution of nanoparticles over the cross section of the polymer matrix.

DOI: 10.3103/S1068375509020161

Nanoparticles on the basis of chalcogenide semiconductors are promising materials for application in optoelectronics, medicine, high-speed computing systems [1–3], gas sensors [4–7], and other branches of industry. In recent years, nanocomposites prepared of polymers and semiconductor particles have been an object of extensive research. This is linked with the possibility to change the physicochemical properties of the materials by employing the variation of the polymer-to-semiconductor ratio. The study of the electrical properties of the aforementioned materials [9–11] enables one to assess the physicochemical processes that occur in these systems and to outline the prospects for their application. Various factors can influence the physicochemical properties of nanocomposites: the particle separation, the interphase interactions, the character of the polymer molecular structure, the method of the nanocomposite preparation, and so on.

The given paper relates to the study of the electrical properties of nanocomposites on the basis of copper sulfide (CuS) nanoparticles and polyvinyl alcohol (PVA).

METHOD OF PREPARATION OF CUS/PVA NANOCOMPOSITES

The CuS/PVA nanocomposites were prepared using the method of successive ionic layer chemosorption in the volume of a polymer matrix described in [12–16]. Thin films of polyvinyl alcohol were used as a polymer matrix. Solutions of $CuSO_4 \cdot 5H_2O$ and $Na_2S \cdot 9H_2O$ in ethylene glycol were used as a source of cations and anions, respectively. The concentration of all the solutions was of 0.2 M. The sorption duration for each ion type was 30 minutes. After the sorption of each ion type, the samples were twice washed in ethylene glycol to eliminate the electrolyte residue. This allowed preventing the possibility of spontaneous nucleation in the volume of the polymer matrix. The process of formation of nanoparticles was started with the sorption of copper ions. It is known that copper ions form weak bonds with polymers in the process of sorption in the volume of polyvinyl alcohol [17] and can migrate under the action of a double electric layer, which forms at the electrolyte–PVA film interface.

The investigation of the morphology of the samples using an NTEGRA (NT MDT) atomic force microscope (AFM) showed that the average dimensions of the particles were 5.3 nm for five growth cycles and 20 nm for fifteen cycles.

SAMPLE PREPARATION AND METHOD OF MEASUREMENTS

The electrical properties of the prepared samples were determined using an E7-20 immittance meter in the frequency range of 265 Hz–1 MHz. The CuS/PVA samples were placed between the metal electrodes in a sandwich configuration. The thickness of the films was 150, 508, and 280 μm for the samples prepared using five, ten, and fifteen formation cycles, respectively. A voltage of 1 V was applied to the samples.

RESULTS AND DISCUSSION

Figure 1 shows the dependence of the variation of the film mass versus the number of cycles performed during the formation of copper sulfide nanoparticles. As can be seen in the figure, the mass portion of copper sulfide amounts to 85% when the number of cycles is two. The further increase in the number of cycles does not substantially change the mass portion of copper sulfide. This is associated with the fact that the polymer

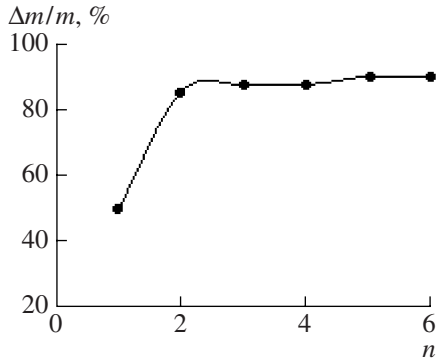

Fig. 1. Dependence of the film mass versus the number of cycles of formation.

pores become filled during the first two formation cycles. With the further increase in the cycle number, the formation of CuS nanoparticles occurs preferably due to the increase in the surface layer thickness.

The dependences of the dielectric permittivities of the CuS/PVA samples versus the frequency for various formation cycles were measured at temperatures of 348–378 K. The results of the measurements of ε at various temperatures for five formation cycles are shown in Fig. 2a. As can be seen in the figure, the dielectric permittivity of the samples increases when the temperature increases. The mobility of the dipoles increases with the temperature increasing; this facilitates the process of orientation of the dipoles. For low frequencies (ν = 265 Hz), the dielectric permittivity changes as a function of the temperature in the range from 9.8 to 22.36. The value of the dielectric permittivity decreases when the frequency increases. For higher frequencies, the ε value changes insignificantly in the range from 7.7 to 9.2.

The dependence of the dielectric permittivity versus the frequency at various temperatures for the samples with ten cycles of formation is shown in Fig. 2b. As can be seen in the figure, the value of the dielectric permittivity in the frequency range of ν = 265 Hz–1MHz increases and changes in the range of 35–151.8 with the increase in the concentration of nanoparticles. In contrast to the samples with five cycles of growth, the value of the dielectric permittivity does not depend on the temperature beginning from the frequency of 10 kHz and decreases monotonously to the value of 35 for higher frequencies.

Figure 2c shows the dependence of the dielectric permittivity of CuS/PVA samples with fifteen cycles of formation versus the frequency at various temperatures. As can be seen in the figure, the values of the dielectric permittivity of the samples vary in the range of 80–118 for the frequency value of 256 Hz.

The variation of the dielectric permittivity ε of the samples versus the frequency for low frequencies is associated with the fact that there is enough time at low

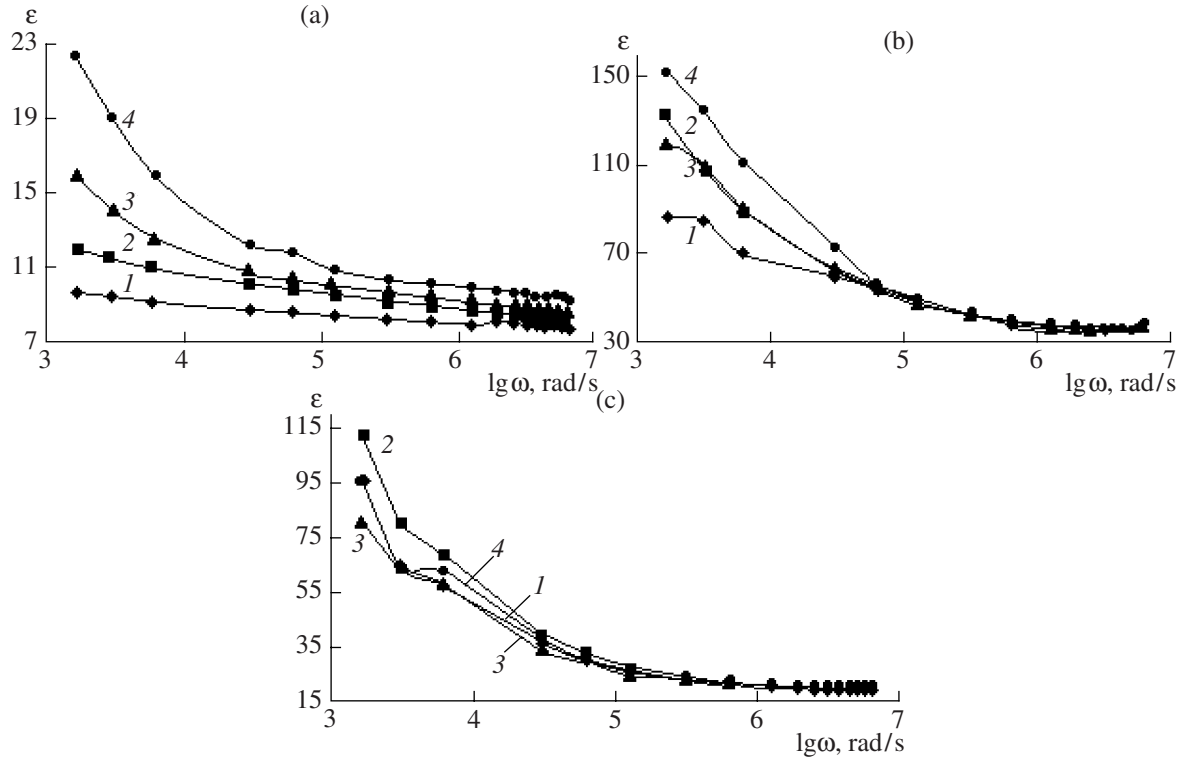

Fig. 2. Dependence of the dielectric permittivity of the CuS/PVA samples versus the frequency at various temperatures and for various number of cycles of formation: (a) 5 cycles, (b) 10 cycles, and (c) 15 cycles.

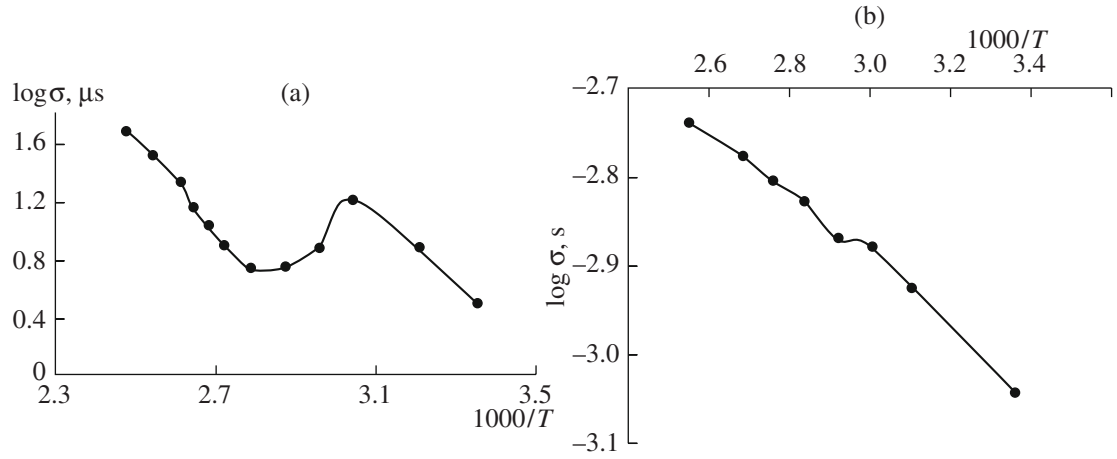

Fig. 3. Dependence of the conductivity versus the temperature for CuS/PVA samples with (a) five cycles of formation and (b) ten cycles of formation.

frequencies for the polarization to change its direction; this does not occur at higher frequencies. Therefore, at higher frequencies, the dielectric permittivity reaches a definite frequency and then remains unchanged.

As can be seen in Fig. 2, the dielectric permittivity of the samples with fifteen cycles of formation is higher than for the samples with five cycles of formation, but it is lower than for the samples with ten cycles of formation. This increase in the dielectric permittivity with increasing the number of cycles is associated with the filling of the polymer with copper sulfide nanoparticles. At the subsequent increase in the number of cycles (15 cycles), the nanoparticles, owing to their electrostatic interaction with the ions of the electrolyte solution, migrate out of the polymer bulk onto the near-surface region [17]. This results in the decreasing of the dielectric permittivity.

Using the results of the studied temperature dependences of the conductivity (Fig. 3), we calculated the activation energies of the samples according to the formula [18]

$$\Delta E = 0.2(\log\sigma_2 - \log\sigma_1)/(10^3/T_1 - 10^3/T_2). \quad (1)$$

The calculated values of the activation energy (Fig. 3) and the electrical conductivity showed that they depend on the number of cycles. The values of the activation energy decrease and that of the conductivity increase when the number of cycles increases. The values of the activation energy amount to $E_a = 0.47$ eV for the samples with five cycles of formation and $E_a = 0.07$ eV for the samples with ten cycles of formation. The lowering of the activation energy with the increase in the number of cycles (that is, with the increase in the dimensions of the nanoparticles) can be explained by the quantum-dimensional effects in the nanoparticles [19]. The increase in the dimensions of the nanoparticles decreases the forbidden gap:

$$\Delta Eg = \hbar^2\pi^2/2m_r a^2, \quad (2)$$

where ΔE_g is the variation of the forbidden gap in the nanoparticles, m_r is the reduced effective mass of the charge carriers, $\hbar$ is the Planck constant, and a is the radius of the nanoparticle.

According to Eq. (2), the energy separation between the donor level and the conduction band decreases owing to the increase in the dimensions of the nanoparticles. The formation of defect levels can be determined by various factors. In our opinion, the interaction of the nanoparticles with the polymer matrix plays a dominant role in this process.

The dependences of the conductivity of the composites with five and ten cycles of formation measured for $\nu = 1$ KHz are presented in Fig. 3. As can be seen in the figure, the conductivity for the samples with five cycles of formation is higher than that for the samples with ten cycles. For the samples with five cycles of formation, the conductivity increases with the temperature increasing. Having reached a temperature of 55°C, the conductivity decreases, and it again increases beginning from a temperature of 85°C. The lowering of the conductivity with an increase in the number of cycles is associated with the redistribution of the nanoparticles over the thickness of the polymer film [17]. Owing to this redistribution, the concentration of semiconductor nanoparticles increases in the near-surface region; this leads to the decreasing of the transverse resistance of the sample.

CONCLUSION

The dielectric permittivity and conductivity of nanocomposites on the basis of copper sulfide and PVA were investigated at various frequencies and temperatures. The values of the dielectric permittivity and conductivity of the samples were calculated in the frequency range of 265 Hz–1 MHz. It was determined from the temperature dependence that the activation energy of the charge carriers depends on the size of the

particles. This was explained by the quantum-dimensional effects in the nanoparticles.

ACKNOWLEDGMENTS

The authors would like to acknowledge the helpful assistance of G.Yu. Mamedova and L.A. Binnatova in fulfilling this research. This research was supported by STCU (grant no. 3486).

REFERENCES

1. Han, J., Zhang, W., Chen, W., Thamizhmani, L., Azad, A.K., and Zhu, Z. Far-infrared Characteristics of ZnS Nanoparticles Measured by Terahertz Time-domain Spectroscopy, *J. Phys. Chem. B*, 2006, vol. 110, no. 5, pp. 1989–1993.
2. Zhang, T.Y., and Cao, J.C., Optical Absorption in Semiconductor Nanorings under a Lateral Terahertz Electric Field, *J. Appl. Phys.*, 2005, vol. 97, no. 2, pp. 024307-1–5.
3. Sigmund, J., Sydlo, C., Hartnagel, H.L., Benker, N., Fuess, H., Rtz, F., Kleine-Ostmann, T., and Koch M. Structure Investigation of Low-Temperature-Grown GaAsSb, a Material for Photoconductive Terahertz Antennas, *Appl. Phys. Lett.*, 2005, vol. 87, no. 25, pp. 252103-1–3.
4. Burda, C. and El-Sayed M. A. High-density Femtosecond Transient Absorption Spectroscopy of Semiconductor Nanoparticles. a Tool to Investigate Surface Quality, *Pure Appl. Chem.*, 2000, vol. 72, nos. 1–2, pp. 165–177.
5. Salomonsson, S. Roy, Aulin, Ch., Cerdà, J., Käll, P.O., Ojamäe, L., Strand, M., and Lloyd Spetz A. Nanoparticles for Long Term Stable, More Selective MISiCFET Gas Sensors, *Sensors Actuators B*, 2005, vol. 107, pp. 831–838.
6. Baraton, M.I., and Merhari L., Nanoparticles-based Chemical Gas Sensors for Outdoor Air Quality Monotoring Microstations, *Mat. Sci. Eng. B*, 2004, vol. 112, pp. 206–213.
7. Hülser, T.P., Wiggers, H., Kruis, F.E., and Lorke A., Nanostructured Gas Sensors and Electrical Characterization of Deposited SnO_2 Nanoparticles in Ambient Gas Atmosphere, *Sensors Actuators B*, 2005, vol. 109, pp. 13–18.
8. Xu, H., Liu, X., Cui, D., Li, M., and Jiang, M., A Novel Method for Improving the Performance of ZnO Gas Sensors, *Sensors and Actuators B, Chem.*, 2006, vol. 114, pp. 301–307.
9. Meirav, U., Kastne, M.A., and Wind, S.J., Single-electron Charging and Periodic Conductance Resonances in GaAs Nanostructures, *Phys. Rev. Lett.*, 1990, vol. 65, pp. 771–774.
10. Seto, J.Y.W., The Electrical Properties of Polycrystalline Silicon Films, *J. Appl. Phys.*, 1975, vol. 46, pp. 5247–5254.
11. Conte, G., Feliciangeli, M.C., and Rossi, M.C., Impedance of Nanometer Sized Silicon Structures, *Appl. Phys. Lett.*, 2006, vol. 89, no. 2, pp. 022118-1–3.
12. Nicolau, F., and Menard, J.C., Solution Growth of ZnS, CdS and $Zn_{1-x}Cd_xS$ Thin Films by the Successive Ionic-layer Adsorption and Reaction Process; Growth Mechanism, *J. Cryst. Growth*, 1988, vol. 92, pp. 128–142.
13. Klechkovskaya, V.V., Maslov, V.N., Muradov, M.B., and Semiletov, S.A., Investigation of the Growth Process and Structure of Semiconductor Films of CdS, ZnS and Solid Solutions on Their Basis Prepared Using the Mechanism of Successive Layer Chemosorption from Electrolyte Solutions, *Soviet Physics Crystallographica*, 1989, vol. 34, no. 1, pp. 182–186.
14. Lindroos, S., Kanniainen, T., and Leskela, M., *Thin Solid Films*, 1995, no. 263, pp. 79.
15. Agasiev, A.A., and Muradov, M.B., Formation of Cadmium Sulfide Particles in the Bulk of a Polymer Matrix, *Pis'ma v Zhurnal Tekhnicheskoi Fiziki*, 1997, no. 17, pp. 54–57.
16. Tolstoy, V.P., Successive Ionic Layer Deposition. The Use in Nanotechnology, *Russian Chemical Reviews*, 2006, vol. 75, no. 2, pp. 183–199.
17. Volkov, A.V., Moskvina, M.A., Karachevtsev, I.V., Lebedeva, O.V., Volynskii, A.L., and Bakeev, N.F., The Structure and Electric Conductivity of Highly Disperse in situ Polymer–CuS Compositions, *Polymer Sci. A*, 1998, vol. 40, no. 6. pp. 970–976.
18. Mott, N.F., and Davis, E.A., Electronic Processes in Non-crystalline Materials, Oxford: Oxford Univ. Press, 1979.
19. Mao, S.S., Nanolasers: Lasing from Nanoscale Quantum Wires, *Int. J. Nanotech.*, 2004, vol. 1, no. 1/2, pp. 42–85.